MASTER'S THESIS

Validation and Verification of Thermo-Hydro-Mechanical (THM) Coupling in Plaxis.

Lucas Abraham Willemsen

Master of Science
Civil Engineering

Luleå University of Technology
Department of Civil, Environmental and Natural Resources Engineering

LULEÅ UNIVERSITY OF TECHNOLOGY

Validation and verification of Thermo-Hydro-Mechanical (THM) coupling in Plaxis

Lucas Abraham Willemsen

25th May 2011

Supervisors Plaxis:
R. Brinkgreve
A. Haxaire
V. Galavi

Supervisor LTU:
H. Mattsson

Abstract

In this thesis the first steps in the verification process of the new Thermo-Hydro-Mechanical (THM) kernel of PLAXIS are made. The proper implementation of the governing equations is verified by comparing model output with analytical solutions. Good agreement is obtained for thermo-mechanical problems. The governing equations for a full THM study are coupled and non-linear. Because of this analytical solutions are only available when approximations are made. An exact solution is presented for the advection-diffusion equation of temperature. The implementation of the vapor diffusion is investigated. The model CODE_BRIGHT developed at the University of Catalonia (UPC) has been matched with experimental results. By matching the model output of PLAXIS with CODE_BRIGHT it will be possible to obtain similar agreement with experimental results. Good agreement between PLAXIS and CODE_BRIGHT is demonstrated by doing a numerical comparison.

Contents

Chapter 1

Introduction

A good understanding of Thermo-Hydro-Mechanical (THM) coupling is essential for the storage of nuclear waste. The radioactive isotopes pose a long-lasting threat to the environment. It is therefore essential that a repository retains its structural integrity for these time scales. One way of storing nuclear waste would be to excavate tunnels in material with a very low permeability. Examples of these materials would be clay or salt rock formations [56]. The void space around the metal canisters is then backfilled with expansive bentonite [43]. Together with the host rock this forms a barrier, shielding the environment form the harmful impact of the radioactive isotopes. The flow of water through the barrier is expected to be very low. Vapor diffusion may become a dominant transport mechanism due to the thermal gradient induced by the decay of radioactive isotopes inside the canisters [47] [56]. Another possible escape route for the contaminants is the formation of shear bands, since they can form a preferential escape route for the contaminants through advection [47].

Temperature has an effect on the surface tension of water, which in turn influences the retention curve of a material [54]. Additionally, the permeability, stiffness and mechanical behavior of rock and soil also shows a strong temperature dependence, as demonstrated by [57]. In order to model the long term behavior of a barrier it is important to model all these effects that couple temperature, water pressure and strain. Other geotechnical applications in which temperature plays an important role are the construction of geothermal power plants and subsurface freezing. The former is a key challenge in sustainable energy. The latter provides temporary stability and is most common in soil tunneling, but is also applied in mining and rock engineering.

This document is structured as follows. First a literature review is done in which topics relevant to thermo-hydro-mechanical coupling are discussed. The set of governing equations implemented in the new THM module of PLAXIS is given in Chapter 3.1. In order to demonstrate the proper computer implementation of these equations the numerical results are compared with analytical solutions. No analytical results are known for the full set of governing equations since they are coupled and nonlinear. So special cases are modeled in which only a subset of the governing equations are required. When the numerical implementation has been verified to a satisfactory level the numerical results of PLAXIS will be compared with those from CODE_BRIGHT. CODE_BRIGHT has been extensively validated with experimental results [45] [19] [41].

Chapter 2

Geotechnical principles and the theoretical aspects of THM-coupling

2.1 General THM balance equations

In this section the balance equations for mass, energy density and momentum are derived. The procedure described by Rutqvist et.al [42] is followed in these derivations. The starting point is the general thermodynamic balance equation given by:

$$\frac{\partial}{\partial t} M_\psi^\kappa + \nabla \cdot \mathbf{q}_\psi^\kappa - Q_\psi^\kappa = 0 \tag{2.1}$$

In which M_ψ^κ represents the mass or energy per unit volume. In this context κ represents the mass component (solid, water or dry air) or the 'heat component' and ψ represents a phase. In the following derivations three different phases will be distinguished: solid, liquid and gas. Additional phases such as the contractile skin [12] have negligible volumetric contributions and are therefore neglected. Furthermore, contaminant phases are not considered either. Q_ψ^κ in equation (2.1) represents a production rate of component κ in phase ψ. Take for example Q_l^a which represents a production of the 'dry air' mass component per unit volume in the liquid phase. This term could represent a physical process like the dissolution of air into water. The term $\mathbf{q}_\psi^\kappa$ in equation (2.1) represents a flux density with respect to a fixed coordinate system.

2.1.1 Fluid mass conservation equations

When deriving fluid mass conservation equations, M_ψ^κ can be expressed as:

$$M_\psi^\kappa = \phi S_\psi \rho_\psi^\kappa \tag{2.2}$$

In which ϕ represents porosity. Also, the flux vector $\mathbf{q}_\psi^\kappa$ can be expressed as:

$$\mathbf{q}_\psi^\kappa = \mathbf{i}_\psi^\kappa + \phi S_\psi \rho_\psi^\kappa \mathbf{v}_\psi \tag{2.3}$$

In which $\mathbf{i}_\psi^\kappa$ represents a diffusive/dispersive mass flux of component κ in phase ψ. The velocity vector $\mathbf{v}_\psi$ in the advective term represents the physical velocity of the fluid phase and is not a bulk volume average. This velocity can be decomposed in two vectors: one representing the solid $\mathbf{v}_s$ and one relative to the solid $\mathbf{v}_{r\psi}$.

$$\mathbf{v}_\psi = \mathbf{v}_{r\psi} + \mathbf{v}_s \tag{2.4}$$

Inserting equation (2.2) and (2.3) into (2.1) gives for the fluid mass balance:

$$\frac{\partial}{\partial t}\left(\phi S_\psi \rho_\psi^\kappa\right) + \nabla \cdot \left(\mathbf{i}_\psi^\kappa + \phi S_\psi \rho_\psi^\kappa \mathbf{v}_\psi\right) - Q_\psi^\kappa = 0 \tag{2.5}$$

As mentioned before, the term Q_ψ^κ can represent the movement of a component between phases due to dissolution or evaporation/condensation. An equation similar to (2.5) can be derived for the solid. There is no source term for the solid mass per unit volume (i.e. it is assumed that the solid will not dissolve in the fluid).

$$\frac{\partial}{\partial t}\left(\left(1-\phi\right)\rho_s\right) + \nabla \cdot \left(\left(1-\phi\right)\rho_s \mathbf{v}_s\right) = 0 \tag{2.6}$$

Inserting equation (2.4) into equation (2.5) and applying the product rule gives:

$$\frac{\partial}{\partial t}\left(\phi S_\psi \rho_\psi^\kappa\right) + \phi S_\psi \rho_\phi^\kappa \left(\nabla \cdot \mathbf{v}_s\right) + \mathbf{v}_s \cdot \nabla\left(\phi S_\psi \rho_\psi^\kappa\right) + \nabla \cdot \left(\mathbf{i}_\phi^\kappa + \phi S_\psi \rho_\psi^\kappa \mathbf{v}_{r\psi}\right) - Q_\psi^\kappa = 0 \tag{2.7}$$

The material derivative following the solid can be written as:

$$\frac{D}{D^s t} = \frac{\partial}{\partial t} + \mathbf{v}_s \cdot \nabla \tag{2.8}$$

With this definition equation (2.7) can be written in a more convenient form:

$$\phi \frac{D\left(S_\psi \rho_\psi^\kappa\right)}{D^s t} + S_\psi \rho_\psi^\kappa \frac{D\phi}{D^s t} + \phi S_\psi \rho_\psi^\kappa \left(\nabla \cdot \mathbf{v}_s\right) + \nabla \cdot \left(\mathbf{i}_\psi^\kappa + \mathbf{q}_{r\psi}^\kappa\right) - Q_\psi^\kappa = 0 \tag{2.9}$$

In which:

$$\mathbf{q}_{r\psi}^\kappa = \phi S_\psi \rho_\psi^\kappa \mathbf{v}_{r\psi} \tag{2.10}$$

A similar procedure can be applied to the solid mass balance equation in equation (2.6). Applying the product rule yields:

$$\frac{\partial\left(\left(1-\phi\right)\rho_s\right)}{\partial t} + \mathbf{v}_s \cdot \nabla\left(\left(1-\phi\right)\rho_s\right) + \left(1-\phi\right)\rho_s\left(\nabla \cdot \mathbf{v}_s\right) = 0 \tag{2.11}$$

This equation can again be transformed from its Eulerian form (i.e. observed from a fixed coordinate system) into its Lagrangian form (i.e. co-moving coordinate system) by using the material derivative given in equation (2.8).

$$\frac{D\left(\left(1-\phi\right)\rho_s\right)}{D^s t} + \left(1-\phi\right)\rho_s\left(\nabla \cdot \mathbf{v}_s\right) = 0 \tag{2.12}$$

This equation can be used to get an expression for the term $\frac{D\phi}{D^s t}$ that appears in equation (2.9). Applying the product rule gives.

$$\frac{D\phi}{D^s t} = \frac{\left(1-\phi\right)}{\rho_s}\frac{D\rho_s}{D^s t} + \left(1-\phi\right)\left(\nabla \cdot \mathbf{v}_s\right) \tag{2.13}$$

The divergence of the solid velocity can easily be rewritten when the definition of volumetric Cauchy strain is used:

$$\nabla \cdot \mathbf{v}_s = \frac{\partial \varepsilon_V}{\partial t} \tag{2.14}$$

Equation (2.14) can be plugged into (2.13) and (2.12). These last two equations can then be combined. When the assumption is made that $\mathbf{v}_s \cdot \nabla S_\psi \rho_\psi^\kappa$ and $\mathbf{v}_s \cdot \nabla \rho_s$ are negligigle (when small strain is assumed) [42] this yields:

$$\phi \frac{\partial\left(S_\psi \rho_\psi^\kappa\right)}{\partial t} + S_\psi \rho_\psi^\kappa \left[\frac{\partial \varepsilon_V}{\partial t} + \frac{\left(1-\phi\right)}{\rho_s}\frac{\partial \rho_s}{\partial t}\right] - Q_\psi^\kappa = -\nabla \cdot \left(\mathbf{i}_\psi^\kappa + \mathbf{q}_{r\psi}^\kappa\right) \tag{2.15}$$

The mass balance of each component can be derived by summing the contributions from the two liquid phases.

$$\phi \frac{\partial\left(S_l \rho_l^\kappa + S_g \rho_g^\kappa\right)}{\partial t} + \left(S_l \rho_l^\kappa + S_g \rho_g^\kappa\right)\left[\frac{\partial \varepsilon_V}{\partial t} + \frac{\left(1-\phi\right)}{\rho_s}\frac{\partial \rho_s}{\partial t}\right] = -\nabla \cdot \left(\mathbf{i}_l^\kappa + \mathbf{q}_{rl}^\kappa + \mathbf{i}_g^\kappa + \mathbf{q}_{rg}^\kappa\right) \tag{2.16}$$

Note that the production term dropped out. Since Q_ψ^κ represent the movement of a component between the two liquid phases, the sum of Q_l^κ and Q_g^κ must be zero due to mass conservation (i.e. no mass can disappear or be created out of nothing).

2.1.2 Energy conservation equations

A similar procedure can be applied to derive an equation for energy balance. The internal energy content and the energy flux for each fluid phase can be defined as:

$$M_\psi^h = \phi S_\psi \rho_\psi e_\psi \tag{2.17}$$

$$\begin{aligned}\mathbf{q}_{\psi}^{h} &= \mathbf{i}_{\psi}^{h} + e_{\psi}^{a}\mathbf{q}_{r\psi}^{a} + e_{\psi}^{w}\mathbf{q}_{r\psi}^{w} + \phi S_{\psi}\rho_{\psi}e_{\psi}\mathbf{v}_{s} \\ &= \mathbf{i}_{\psi}^{h} + \mathbf{q}_{r\psi}^{h} + \phi S_{\psi}\rho_{\psi}e_{\psi}\mathbf{v}_{s} \end{aligned} \tag{2.18}$$

$\mathbf{i}_{\psi}^{h}$ represents a diffusive energy flux described by Fourier's law. e_{ψ}^{κ} represents the internal energy per unit mass of component κ in phase ψ. The remainder of equation (2.18) represents an advective flux of energy. The velocity term in the advective flux is again decomposed in two parts: one for the solid velocity and the other for the fluid velocity relative to the solid. The internal energy content and energy flux density of the solid can be expressed as:

$$M_{s}^{h} = (1-\phi)\rho_{s}e_{s} \tag{2.19}$$

$$\mathbf{q}_{s}^{h} = \mathbf{i}_{s}^{h} + (1-\phi)\,\rho_{s}e_{s}\mathbf{v}_{s} \tag{2.20}$$

Local thermal equilibrium is assumed. This means that the temperature of the solid, liquid and gas phases at a certain point are considered to be equal. This is a good approximation when the flow velocity is small since the phases then have sufficient time to equilibrate. This assumption allows assembly of a single energy equation. Inserting terms in equation (2.1) and summing the energy balance contributions from the solid, liquid and gas phases under the assumption that $\mathbf{v}_s$ is small gives:

$$\frac{\partial\left(\phi S_{l}\rho_{l}e_{l} + \phi S_{g}\rho_{g}e_{g} + (1-\phi)\rho_{s}e_{s}\right)}{\partial t} - Q^{h} = -\nabla\cdot\left(\mathbf{i}_{m}^{h} + \mathbf{q}_{rl}^{h} + \mathbf{q}_{rg}^{h}\right) \tag{2.21}$$

In which Q^h is the total energy production in all of the phases and $\mathbf{i}_m^h$ is an equivalent heat conduction for all the phases. Using such an equivalent heat conduction is only justified under the assumption of uniform temperature. When the three phases have their individual temperature the equations become a lot more complicated. Heat would be diffused to the surrounding (mathematical) points but it would also be exchanged between the phases at the same point. The reason for this is that in the used approach each phase is present at every point. This is convenient to get equations suitable for continuum models and the finite element method. The latter is based on interpolation of nodal values within an element which becomes questionable for discontinuous phases.

If thermal equilibrium would not be assumed this energy exchange between phases could be integrated in the production terms Q for each phase's energy balance equation. These contributions would cancel out in the summation leading to (2.21). Nevertheless, the heat exchange between the phases at a specific point would have to be investigated and properly modeled since it affects the temperature of each of the phases individually. Instead of equation (2.21), three energy balance equations would have to be used. One for each phase. And each equation would require an expression for its own heat conduction and energy production. But since we assume thermal equilibrium, the single equation (2.21) is sufficient and an equivalent heat conduction is used, represented by the term $\mathbf{i}_m^h$. It depends on the volume fractions of the different phases (through porosity and saturation) and their specific thermal conductivities. The assumption of local thermal equilibrium is often made for geotechnical applications.

2.1.3 Momentum conservation equation

The last conservation equations deals with momentum. In the approach used here each phase is assumed to be present at every point with volume fractions adding up to unity, allowing techniques from continuum mechanics. One of the most fundamental equations is the equation of motion [13].

$$\rho\frac{D\mathbf{v}}{Dt} = \nabla\cdot\sigma + \mathbf{X} \tag{2.22}$$

In which σ is the stress tensor and $\mathbf{X}$ represents a body force. In the absence of electromagnetic forces the body force reduces to the weight of the material. When stress equilibrium is achieved, equation (2.22) reduces to:

$$\nabla\cdot\sigma + \rho_{m}\mathbf{g} = 0 \tag{2.23}$$

In which ρ_m is the density specified at each point by adding the weight contributions of the solid, liquid and gas phase.

$$\rho_{m} = (1-\phi)\,\rho_{s} + \phi S_{l}\rho_{l} + \phi S_{g}\rho_{g} \tag{2.24}$$

The total stress σ can be decomposed into an effective stress and a pressure term according to Bishop's method.

$$\sigma = \sigma' + \left(\chi p_{w} + (1-\chi)\,p_{g}\right)\mathbf{I} \tag{2.25}$$

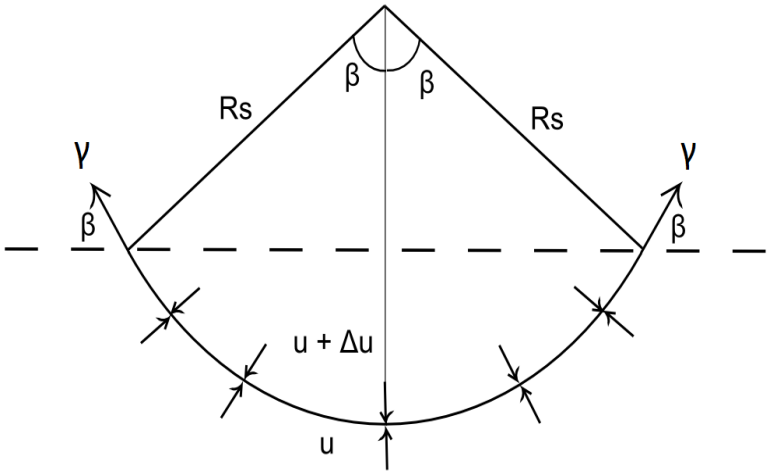

Figure 2.1: The forces acting on the contractile skin. u stands for pressure, γ for surface tension and R_s for the radius of curvature of the contractile skin. Redrawn from figure in [12]

Insertion into equation (2.23) yields:

$$\nabla \cdot (\sigma' + (\chi p_w + (1 - \chi)\, p_g)\, \mathbf{I}) + \rho_m \mathbf{g} = 0 \tag{2.26}$$

In diffential form this becomes:

$$\nabla \cdot (d\sigma' + (d\chi p_w + \chi dp_w + (1 - \chi)\, dp_g - d\chi p_g)\, \mathbf{I}) + d(\rho_m \mathbf{g}) = 0 \tag{2.27}$$

2.2 Water in unsaturated soils

2.2.1 Surface tension and suction

Molecules within a fluid phase mutually attrach each other. Let's consider a free surface (e.g. interface between air and water), although similar principles apply at interfaces between immiscible fluids (e.g. oil and water). A water molecule in the bulk fluid is attracted by its neighboring molecules while a molecule at a free surface is attracted by a reduced number of neighbors and is therefore in an energetically unfavorable position. The formation of free surfaces therefore costs energy [9]. Since systems naturally move from high to low energy states, a water phase takes on a form of minimum surface area. This is the reason why water is ejected in the form of drops when a rock is thrown in a lake. By approaching a spherical shape the ejected water moves towards a lower energy state. The free surface, i.e the interface between air and water, is sometimes referred to as the contractile skin. A pressure difference between the air phase and water phase can be present. The contractile skin will bend towards the phase with the highest pressure [12]. The surface tension within the contractile skin will balance the difference in pressure. A similar effect occurs when a rubber balloon is filled with air. The pressure inside the balloon is higher than the atmospheric pressure. The tension applied by the inflated elastic rubber membrane of the balloon has an effect that is equivalent to a that of the contractile skin. The membrane is curved around the medium of higher pressure, creating a balance of forces. All the forces acting on the contractile skin are displayed in figure 2.1. The pressure difference Δu can be calculated since the forces are in balance. The force downwards due to the difference in pressure can be written as:

$$2\int_0^\beta cos(\theta)\Delta u R_s d\theta = 2\left[sin(\theta)\Delta u R_s\right]_0^\beta = 2sin(\beta)\Delta u R_s \tag{2.28}$$

Which is for obvious reasons similar to the length of the horizontal dotted line $2R_s sin(\beta)$ multiplied by the pressure difference Δu. The weight of the contractile skin has been neglected. Force balance can now be written as:

$$2\gamma sin(\beta) = 2sin(\beta)\Delta u R_s \tag{2.29}$$

In which γ represents the surface tension within the contractile skin. This gives the following expression for the pressure difference Δu.

$$\Delta u = \frac{T_s}{R_s} \tag{2.30}$$

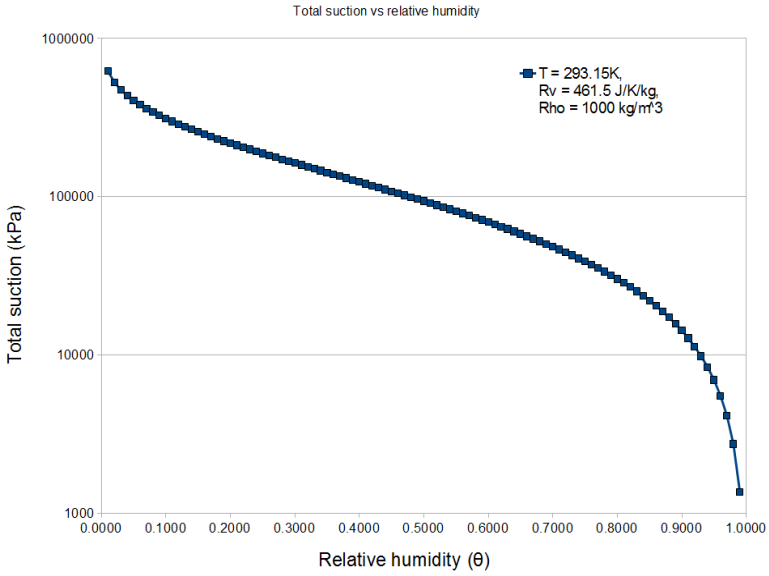

Figure 2.2: Total suction versus relative humidity at T = 293.15 $^{\circ}K$.

Previous calculations were done in a two-dimensional geometry. The contractile skin can have two radii of curvature in a three-dimensional geometry. The pressure difference Δu can then be written as [1]:

$$\Delta u = T_s \left(\frac{1}{R_1} + \frac{1}{R_2} \right) \tag{2.31}$$

When these radii of curvature R_1 and R_2 are equal the pressure difference Δu becomes:

$$\Delta u = \frac{2\gamma}{R_s} \tag{2.32}$$

In unsaturated soils the air pressure is higher than the water pressure. Expressing Δu in terms of air and water gives the well-known equation for matric suction.

$$(u_a - u_w) = \frac{2\gamma}{R_s} \tag{2.33}$$

This equations shows that for a given radius of curvature R_s the pressure difference between the air and water (i.e. matric suction) has a linear dependence on the surface tension γ. It can also be seen that the matric suction shows an inverse dependence on the radius of curvature R_s. This inverse relationship will later be used to explain why capillary action is higher in tubes with a small cross-section. The term surface tension is normally only used for the boundary between a specific phase and air. When two other substances form an interface the term interface tension is used instead, even though the physics behind the phenomenon are similar.

The suction is related to the energy state of soil water [12] [52]. In adition to the matric suction explained previously in this section, an osmotic suction can also occur due to the presence of solutes in the soil water. The variation of the osmotic suction is usually small for geotechnical problems [52]. Or in other words, the gradient of the osmotic component of the free energy is often negligible. Energy differences drive a water flow, this is for instance the basis of expressing water velocity in terms of hydraulic head gradient. Since the variation in the osmotic potential is considered negligible the assumption is made that it will not influence the flow of water. It still influences the energy state of the soil water though. The partial vapor pressure that is in equilibrium with the soil water depends on the water's energy state. The lower the potential energy of the soil water (i.e. higher total suction) the harder it becomes for water to go to the gas phase. The relative humidity is then defined as:

$$\theta = \frac{u_v}{u_{v0}} \tag{2.34}$$

In which u_v represents the vapor pressure and u_{v0} represents the vapor pressure for pure water with a flat surface (i.e. matric suction is zero) at the same temperature. u_{v0} is also known as the saturation

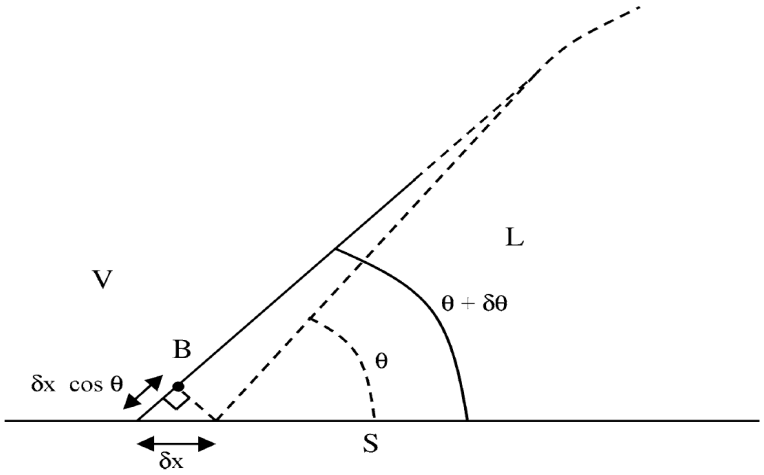

Figure 2.3: The traditional way of deriving Young's equation, based on the idea of local equilibrium. Figure from [40]

vapor pressure. Equation (2.35) relates the relative humidity and the total suction ψ [12]

$$\psi = -R_v \rho_w T \times ln(\theta) \tag{2.35}$$

In which R_v represents the specific gas constant for water vapor. Equation (2.35) shows that at a given temperature the total suction in a soil can directly be expressed as a function of the relative humidity. This relation is illustrated by figure 2.2.

2.2.2 Young's equation and the contact angle

When a liquid and a solid form an interface, the minimization of energy around the contact line gives rise to a contact angle. This angle can be expressed as a function of interface energies. The shape of the contractile skin in a pore represents a minimum energy state. It is therefore determined by both the contact angle and the minimization of the air-water surface area. This motivates the need to investigate the contact angle.

The energy required to create an interface between phases A and B with interface tension γ_{AB} and surface area dA is $dA\gamma_{AB}$. So another way to interpret the interface tension γ_{AB} is to see it as the energy required to create a unit of surface area between the phases A and B. This concept of interface energy is very useful in explaining the phenomenon of contact angle. The equilibrium contact angle θ is the angle that a fluid phase (such as water) makes with a solid phase when in contact with another fluid (such as air). In 1805 Thomas Young (also known for Young's modulus) was the first to find a mathematical relation that expressed θ in terms of the interfacial energies.

$$\gamma_{LV} cos(\theta) = \gamma_{SV} - \gamma_{SL} \tag{2.36}$$

In which S stands for solid, L for liquid and V for vapor/gas. The interface energies depend on temperature. The contact angle θ therefore also has a temperature dependence. The textbook derivation of equation (2.36) normally uses a local derivation. The angle θ that the liquid makes with the soil is seen as a state of minimum energy. This means that the energy will remain constant up to the first order when the position of the contact line is moved a distance δx. See figure 2.3 for the geometry. The assumption is made that the corresponding contact angle change $\delta\theta$ only has a local effect on the position of the LV surface. The new position of the LC surface asymptotically approaches the old position. Therefore the geometry of figure 2.3 suggests that a change in length of the LS interface δx will result in a change $\delta x cos(\theta)$ of the LS surface. If the position of the contact line is independent of the third coordinate this is equivalent to:

$$\delta A_{LV} = \delta A_{SL} cos(\theta) \tag{2.37}$$

The change in energy δU due to this displacement of the contact line can be expressed in terms of these area changes and the accompanying changes in surface energy [40].

$$\begin{aligned} \delta U &= \gamma_{LV} \delta A_{LV} + (\gamma_{SL} - \gamma_{SV})\, \delta A_{SL} \\ &= [\gamma_{LV} cos(\theta) + (\gamma_{SL} - \gamma_{SV})]\, \delta A_{SL} \end{aligned} \tag{2.38}$$

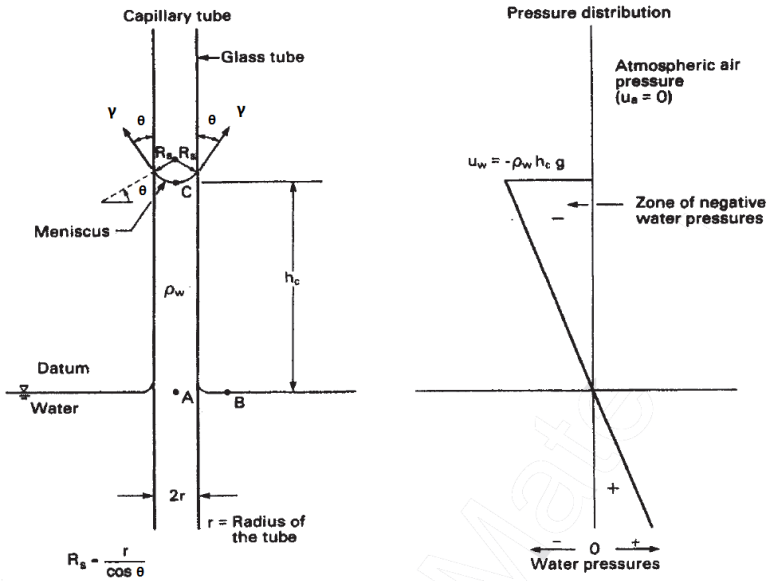

Figure 2.4: Left: Forces working on a column of water in a capillary tube. Right: Pressure distribution in the capillary tube. The atmospheric air pressure equals the water pressure at the water table and is for convenience taken as 0 Pa. Figure from [12]

In which equation (2.37) has been used. Recall that the first order change in energy δU is zero since the system is in a state of minimum energy at contact angle θ. Equation (2.38) therefore reduces to the Young's equation. Even though this local derivation yields Young's equation, which is proven to be correct, it is critisized. First of all the assumption that the position of the LV surface after position change δx approaches that of the old surface is wrong in several scenario's. One example is that of a drop of liquid on a solid surface. The conservation of mass requires that the height of the drop decreases when it spreads out laterally, which contradicts previous assumption. Second of all, the local derivation does not include the effects of gravity on the change in energy δU, even though it does influence the gravitational potential energy. More rigorous derivations have been performed on the basis of thermodynamics by for instance Gibbs, proving the correctness of Young's equation in all general situations in which also gravity applies [40]. The importance of this proof is that the contact angle θ completely depends on material properties in all situations. A specific application of great interest in soil mechanics is the angle that a liquid makes with the soil minerals on the pore walls. This angle will influence the radius of curvature of the water surface in the pore and therefore also the suction (through equation 2.33).

Surface roughness increases the wettable mineral surface area per projected unit area. A complex interplay of equilibrium contact angle and microscale geometry can lead to gas entrapment and the creation of micro-interfaces below the water [32]. The apparent contact angle can therefore show a deviation from the contact angle predicted by Young's equation. This in turn will influence the curvature of the contractile skin in a pore, and therefore also the suction.

2.2.3 Capillarity

The principle of contact angle plays an important role in the phenomenon of capillary rise. When a tube with a small radius is placed in water, adhesive forces will draw the water up along its boundaries. The polar nature of the water molecules can result in strong bonds with the container walls. The water climbing up along the walls of the capillary tube will drag along more water due to the cohesive forces between the water molecules. The rise of water in the tube will eventually stop when gravity counteracts the adhesive and cohesive forces through the weight of the water column. In this equilibrium state the angle θ between water and the container walls is determined by Young's equation (2.36). θ depends on the adhesive forces between water and the capillary tube (i.e. interface energy γ_{SL}) and the interface energies γ_{SV} and γ_{VL}. Young's equation predicts that the more hydrophilic the straw material is (i.e. smaller γ_{SL}) the closer the contact angle will be to zero. A vertical force balance can be derived for the equilibrium state [12], see figure 2.4. The combination of the surface tension of the water and the contact angle with the capillary tube of radius r determine the upward force on the water column. This force can be expressed as $2\pi r\gamma cos(\theta)$. The weight of the water column is the only force acting in the

downwards direction. Atmospheric air pressure acts on the top the column and at the datum so it has no net effect. The weight of the water column can be expressed as $\pi r^2 h_c \rho_w g$ yielding the following vertical force balance equation.

$$2\pi r\gamma cos(\theta) = \pi r^2 h_c \rho_w g \tag{2.39}$$

Rearranging gives the following expression for the capillary height h_c.

$$h_c = \frac{2\gamma}{\rho_w g R_s} \tag{2.40}$$

In which R_s is the radius of the curved surface which is equal to $r/cos(\theta)$. For mathematical convenience the contact angle is often assumed to be 0° [32]. With this assumption R_s is equal to the pore radius r. From equation (2.40) follows that the capillary height reduces as the surface tension reduces. The surface tension of water decreases when the temperature of water increases. At the same time it can also be seen that water will rise higher in a capillary tube with a smaller radius r or smaller equilibrium contact angle θ. As mentioned before this angle depends on the material of the capillary tube, but also on the temperature. On the right side of figure 2.4 the pressure distribution in the capillary tube is displayed. The magnitude of the tensile stress in the water can be obtained from equation (2.33) or by multiplying equation (2.40) by the specific weight $\rho_w g$ of water. Since the water in the capillary tube is in equilibrium a constant hydraulic head is present. The pressure therefore linearly increases down the tube until it reaches atmospheric air pressure at the water table.

The conclusions that could be drawn from the physics of the capillary tube can be extended to other conduits. The porous nature of soils is of particular interest in this thesis. For instance the mineral quartz that composes sand grains has a negative surface charge that strongly attracts polar water molecules. Similar to the capillary experiment, water will be drawn up in the pores until gravity balances the adhesive/cohesive forces.

Remark: In the derivation of the capillary height in equation (2.40) the weight of the water column between h_c and the contact point of the contractile skin and the walls of the capillary tube has not been taken into account. This assumption will be acceptable if h_c is large compared to the radius R_s. It seems like a reasonable assumption especially for fine grained soils since the capillary fringe will be high relative to their small diameter pores. Assumptions of a smooth vertical wall with constant diameter were made in the derivation of the equilibrium height h_c. Both are obviously not valid for soils. So the experiment of the capillary tube is only interesting from a qualitative point of view and not from a quantitative point of view. The qualitative conclusion that finer pores, higher surface tension and lower contact angle result in a higher rise of water remains valid for soils.

Investigating capillary action in angular and slit-shaped pores is more representative for the behavior of a real soil. Pores with these geometries behave differently from cylindrical pores. When angular pores are drained, water will remain in the pore corners. This provides a mechanism for hydraulic continuity in porous media [32]. Investigations in this behavior have lead to retention models developed by researchers such as Tuller (1999). He represents an angular pore by a polygon with n corners. The radius of curvature of the meniscus in each corner can be related to suction. With this formulation the water filled area of a pore can be calculated as function of suction by adding up the contributions at each of the n corners. When the suction reduces below the suction corresponding to the inscribed circle in the angular pore it will completely fill up.

2.2.4 Retention curve

The suction of a saturated soil is zero. The soil can be dried by imposing a fixed relative humidity for instance. The partial vapor pressure which is in equilibrium with the flat water surfaces in a fully saturated soil is higher than the imposed vapor pressure by fixing the relative humidity. Water will evaporate until the suction corresponding to the imposed relative humidity is obtained. The soil is not fully saturated anymore. By gradually drying the soil a relation between the saturation and the suction can be obtained, as shown by Figure 2.2. This relation between the saturation or volumetric water content and the suction of a soil is commonly referred to as the retention curve of a soil. The term soil-water characteristics curve is also commonly used. A special point in the retention curve is the air-entry value [21]. At a certain suction value the radius R_s in equation (2.30) or (2.33) (depending on the shape of the menisci) corresponds to the minimum supported value of R_s in the most prevalent large pores in the soil. When the soil is dried slightly more and the suction increases correspondingly, the radius R_s decreases and the previously mentioned large pores will (partially) drain. Air will replace

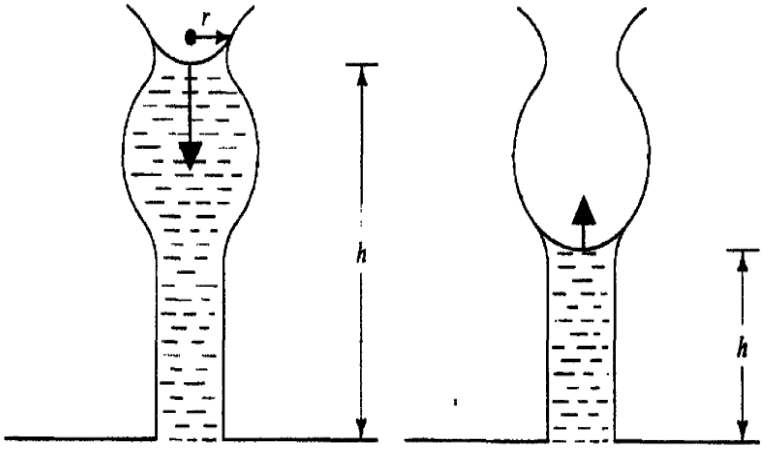

Figure 2.5: The ink bottle effect, one of the causes of soil-water retention curve hysteresis. Both illustrations correspond to the same suction. The downwards arrow on the left indicates the reaction when drying progresses. The upwards arrow on the right indicates the reaction when wetting progresses. Figure from [52]

the water, therefore the name air entry value. This principle is central to the concept of a high air entry disk. Such a disk is normally made of ceramics and it acts as a membrane between air and water [12]. It is used in suction experiments on unsaturated soils where no air is supposed to enter the measuring system. The pores are very small and they will therefore stay filled with water up till high levels of suction, preventing the inflow of air.

The path in saturation / suction space during drying is called the drying curve [24] or the drainage curve [21]. When the soil is wetted again it turns out that the path followed in saturation / suction space deviates from the one during drying. This phenomenon is known as hysteresis of the soil-water retention curve. Four different explanations for this phenomenon are given in literature [24].

1. The ink-bottle effect, see figure 2.5. In a soil the pore space typically consists of large voids connected to each other by pore throats [52]. The radius of these pore throats corresponds to a minimum value of the radius of curvature R_s. It is therefore linked to a maximum value of suction s_{crit} at which a water meniscus covers the pore throat, through equation (2.33). If the suction is increased beyond this point during the drying process, the pore throat and the large void it connects to will empty. On the other hand, at suction s_{crit} on the wetting curve the large void is still empty. The reason is that a lower value of suction is required for the large void to be filled up, due to its larger radius. If the suction is reduced below s_{crit} during wetting, the large void will slowly fill up. So suction s_{crit} corresponds to two different levels of saturation in this example, depending on whether the soil is on the drying or the wetting branch of the retention curve. To summarize: at a given suction the ink-bottle effect will result in higher saturation on the drying curve than on the wetting curve.

2. The contact angle discussed in section 2.2.2 is the equilibrium angle between the water and the soil minerals. This is the angle that will be approached at steady state. When the soil is wetted the water phase advances and the (dynamic) contact angle will be larger. When the water retreats during drying the reverse happens, the (dynamic) contact angle will be smaller than its equilibrium counterpart. The contact angle influences the curvature of the contractile skin, and it therefore also influences the suction as can be seen in equation (2.33). It should be noted however that equation (2.33) was derived on the principle of force balance which may not be valid anymore when the water phase is mobile (no equilibrium anymore).

3. The pore structure may be different during wetting and drying. The void ratio and porosity of expansive clays have a particularly large dependency on the water content [12]. The other hysteresis effects allow for a varying water content at the same suction value. This different water content is associated with different porosity and pore radius values due to the swelling/shrinking nature of clay. This will influence the critical radius of curvature R_s and the suction value associated with it.

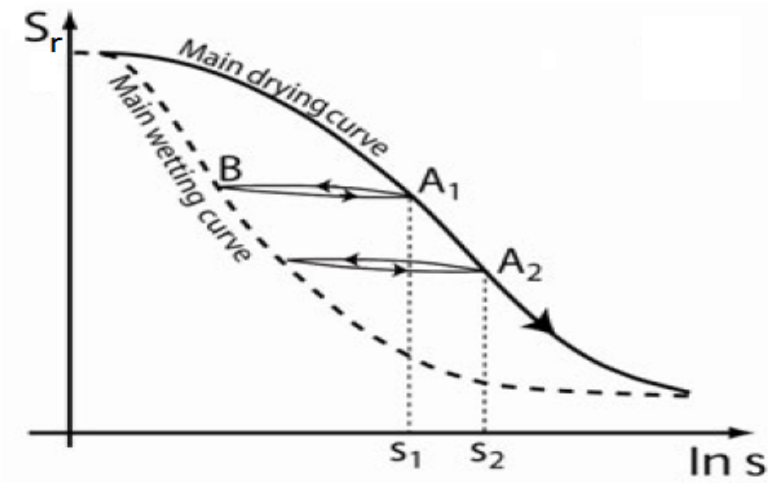

Figure 2.6: A retention curve with hysteresis effects. Saturation S_r is plotted against suction s. Figure from [29]

4. The amount of air bubbles is different during wetting and drying. The presence of air bubbles influences the saturation.

Figure 2.6 serves as an illustration of the concept of hysteresis in the soil water retention curve. This figure shows that the saturation is higher on the drying curve because of the reasons mentioned above. When a soil that is in a state corresponding to a point on the drying curve is suddenly wetted its state will move towards the wetting curve. Even though retention curves show hysteresis effects, it should be noted that they are not often incorporated in mathematical descriptions.

When the soil is gradually dried, the suction increases. The associated decrease in pore water tension stiffens the soil, increases the cohesion and also the apparent pre-consolidation pressure. These effects can be incorporated in constitutive models such as the Barcelona Basic Model (BBM), which is described in section 2.3.2. The tensile stress in the water can go to the order of hundreds of MPa at low relative humidity, as can be seen in figure 2.2. This corresponds to very low saturation levels in a retention curve such as figure in 2.6. At these high values of suction the stability enhancing effects of the tensional pore water will go away since most of the pores are filled with air (i.e. low saturation) [12].

2.2.5 Temperature dependence of retention curve

Villar and Gomez-Espina [54] performed an experiment to investigate the effect of temperature on the retention capacity of MX-80 bentonite. This clay is considered to be a candidate for the construction of a barrier around an underground nuclear waste storage facility.

The experimental procedure can be summarized as follows: first MX-80 with a fixed water content is compacted to a specified density. It is then placed in a closed cell made out of stainless steel. By measuring the relative humidity during the experiment the suction is determined. The suction response during heating/cooling cycles has been measured for the same clay at different water contents. The results are presented in figure 2.7.

Personal interpretation of the experimental results: Interface energies depend on temperature. The contact angle θ expressed by Young's equation (2.36) therefore also depends on temperature, as was discussed in section 2.2.2. The curvature of a meniscus is a balance between the need to satisfy the contact angle at the contact line and the minimization of air-water interfacial area within the pore [32]. Often this surface will not be spherical and the suction will be given by equation (2.32). This is illustrated in figure 2.8. The surface tension/energy of water γ decreases with increasing temperature. So when temperature increases the radii R_1 and R_2 correspond to a lower suction value. If suction would be held constant the radii of curvature would have to decrease to $R_{1'}$ and $R_{2'}$ as illustrated in red in figure 2.8. So if suction is held constant and temperature is increased the pore water would recede more and more to the corners of angular pores and to grain contacts where a high curvature is possible. So for these conditions the water content would decrease, which is in agreement with the experimental results presented in figure 2.7 when following a line of constant suction. Note that the experiment has been performed on clays: the spherical grains displayed in figure 2.8 are not representative for such a soil. It merely illustrates how water retreats into corners where high curvature is possible. Also, the experiment

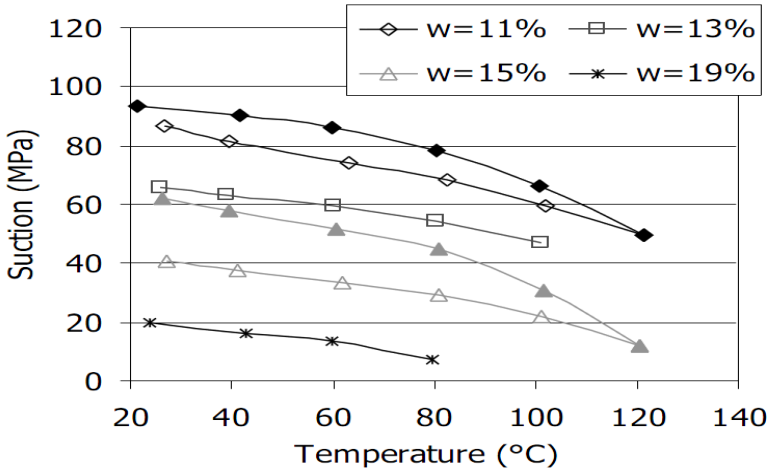

Figure 2.7: Suction response of MX-80 bentonite during heating/cooling cycles at fixed water content. The filled symbols correspond to cooling. Figure from [54]

has been performed in a sealed stainless steel container. The water content could therefore not decrease during the experiment, which can be seen in figure 2.8. The radius of curvature will remain fairly constant and as expected the suction decreases with increasing temperature.

Strong hysteresis effects are also visible. After a complete heating/cooling cycle the suction has increased. This phenomenon can be linked to the causes for hysteresis of the soil water retention curve which are discussed in section 2.2.4. In my opinion a change in the pore structure is the most logical explanation. In section 2.4 the temperature dependency of several mechanical parameters is discussed. Figure 2.12 shows that irrecoverable expansive thermal strain is accumulated during a heating/cooling cycle when suction is fixed. Although the experiment of Villar and Gomez-Espina involves constant water content and not constant suction, the decrease in suction during heating can have resulted in a reduction of the strength of the clay. Suction has the tendency to bind soil grains together. Irrecoverable reconfiguration of the clay particles could have occurred due to the reduction of suction and its stabilizing effects. Also, the tendency of the clay to exhibit volumetric expansion during heating would induce compressive stresses in the test cell with fixed volume. In combination with the reduced cohesion due to the suction decrease this could have altered to pore size distribution.

My hypothesis is that the pores become smaller during the heating of the clay. Larger pores that may have been present form a preferential location for the thermal expansion of the clay. If the larger pores get compressed the prevalence of small pores would increase. This in turn could explain an increase in suction since a larger fraction of the fixed amount of water (closed container) can be stored in the smaller pores. This will allow for a smaller radius of curvature R_s, corresponding to higher suction. On the heating branch of the curves in figure 2.7 the suction decreases. During heating the suction decrease due to the reduced surface tension apparently dominates the suction increase due to the reduction of pore size. When the soil is cooled after having reached its maximum temperature it will have smaller pores at a given temperature than it had before due to the accumulated plastic strain. The suction will be higher accordingly, explaining the difference in suction between the heating and cooling branch of figure 2.7.

2.3 Constitutive models

Constitutive models describe the relationship between stress and strain. Elastic behavior is the easiest to model since no plastic integration is required. The Modified Cam-Clay (MCC) constitutive model is more advanced. It uses an elliptical yield surface in the average mean stress (p'), differential stress (q) space to describe the transition of elastic to elasto-plastic behavior. The Barcelona Basic Model (BBM) is an extension of the MCC, it adds suction as a stress variable. I will introduce the MCC and BBM since these models are used in the modeling of the heater experiment in Chapter 5. Numerous other constitutive models exist such as Drucker-Prager, Hardening soil, Soft soil and many more. Each of these constitutive models has its merits and demerits, but they all follow similar procedures for the formulation of plastic strain.

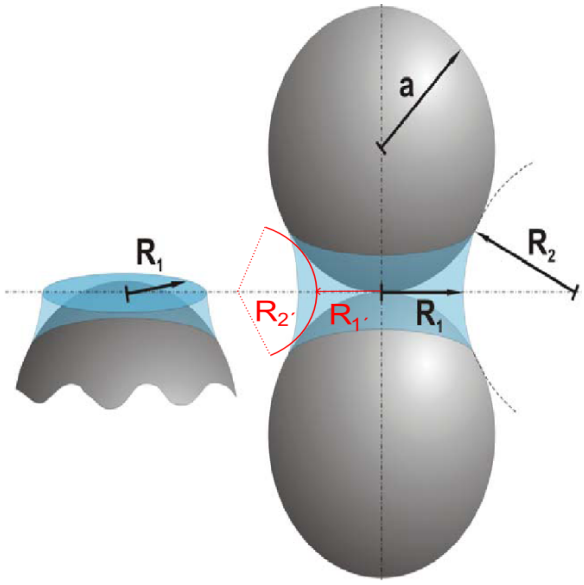

Figure 2.8: Interpretation of the experimental results given in figure 2.7. Radii R_1 and R_2 correspond to an initial temperature and suction. Radii $R_{1'}$ and $R_{2'}$ displayed in red correspond to the same suction but at a different temperature. Figure is modified from [32]

2.3.1 Modified Cam Clay

The Cam-Clay model was developed by Roscoe and Schofield in 1963 [58]. A yield criterion with a logarithmic yield function was developed on the basis of energy considerations. This shape of the yield surface did not match experimentally determined yield loci very well, so it was considered to be somewhat unrealistic. In 1968 Roscoe and Burland derived a different expression for the plastic dissipation of energy, which lead to an elliptical yield surface in the (p', q) space. The model associated with this yield surface came to be known as the Modified Cam Clay model (MCC). The highly innovative nature of the model combined with its relative simplicity make it an historically important model. Additionally, several models such as the BBM extend upon the MCC.

The yield criterion of the MCC can be expressed as follows:

$$f(p', q, p'_0) = q^2 - M^2 p' \left(p'_0 - p'\right) = 0 \tag{2.41}$$

A graphical representation is given in figure 2.9a. Only two parameters are required to define the shape of the yield surface. The first parameter M is used for the slope of the critical state line (CSL). The second parameter, p'_0, denotes the current isotropic preconsolidation stress. It is defined as positive for pressure. The MCC yield surface can also be presented in $(\sigma'_1, \sigma'_2, \sigma'_3)$-space. It then takes on an ellipsoidal shape around the $\sigma'_1 = \sigma'_2 = \sigma'_3$ axis. In this stress space the CSL becomes a cone. For visualization convenience the equivalent two-dimensional p',q space will be used in this section.

The assumption is made that a strain increment can be decomposed into elastic and plastic strain.

$$\varepsilon = \varepsilon^e + \varepsilon^p \tag{2.42}$$

Within the boundaries of the yield surface the plastic strain remains unaltered. There is only variation in the elastic strain. The change in elastic volumetric strain can be expressed as:

$$d\varepsilon_p^e = \kappa^* \frac{dp'}{p'} \tag{2.43}$$

This equation follows from differentiation of the linear relation between the elastic volumetric strain and $ln\,(p')$ as shown in figure 2.9b. This yields the following relation between the effective mean stress increment dp' and the elastic volumetric strain increment ε_p^e.

$$dp' = K d\varepsilon_p^e \,, \qquad K = \frac{p'}{\kappa^*} \tag{2.44}$$

The bulk modulus of the soil linearly increases with increasing effective mean stress. The differential stress q is equal to the difference between the axial stress and the radial stress during compression in

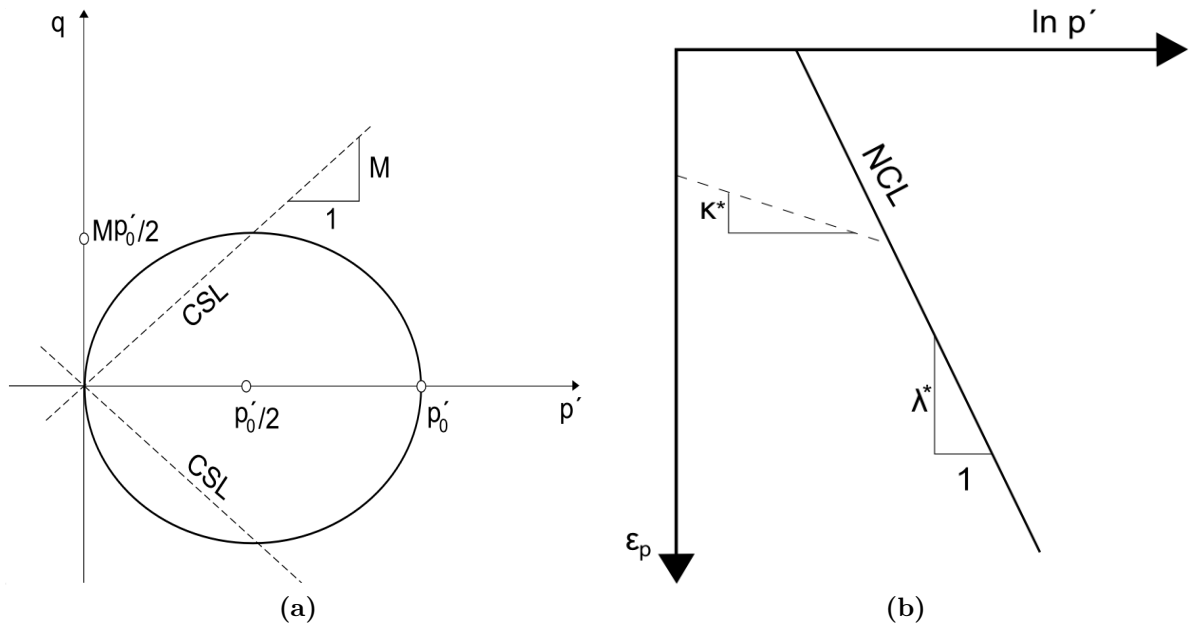

Figure 2.9: a) The elliptical yield locus of the Modified Cam Clay constitutive model. b) Moduli κ^* and λ^* defined in $ln\,(p')$ versus volumetric strain ε_p space. Figures redrawn from [6]

a triaxial apparatus. ε_q^e is the deviation of the major principle strain from one third of the volumetric strain. It can also be interpreted as the elastic axial deviator strain, which is also known as triaxial shear strain [6]. In the MCC q is assumed to have a linear relation with ε_q^e:

$$q = 3G\varepsilon_q^e \tag{2.45}$$

With shear modulus G defined as:

$$G = \frac{3(1-2\nu)}{2(1+\nu)}K \tag{2.46}$$

In PLAXIS the poisson ratio ν is fixed and G is allowed to vary according to the equation above. It may be preferable to allow the poisson ratio to vary and have the shear modulus fixed. Zytynski showed [58] that the Cam-Clay model with constant poisson ratio may not conserve energy during closed stress cycles.

When a stress point is located on the yield surface ($f(p', q, p_0') = 0$), plastic strains can be generated. The mathematical relation that expresses these plastic strain increments is called the flow rule. The gradient of the plastic potential function with respect to the individual stress components is multiplied with a scalar Ω. MCC assumes associated plastic flow, which means that the yield surface $f(p', q, p_0')$ (2.41) is equal to the plastic potential function $g(p', q, p_0')$. So the plastic strain increment vector $\left(d\varepsilon_p^p, d\varepsilon_q^p\right)$ is always perpendicular to the yield surface.

$$\begin{pmatrix} d\varepsilon_p^p \\ \\ d\varepsilon_q^p \end{pmatrix} = \Omega \begin{pmatrix} \frac{\partial f}{\partial p'} \\ \\ \frac{\partial f}{\partial q} \end{pmatrix} = \Omega \begin{pmatrix} M^2\,(2p' - p_0') \\ \\ 2q \end{pmatrix} \tag{2.47}$$

In which the last equality follows from differentiating equation (2.41). In order to find an expression for Ω, the consistency condition is used. During plastic deformation the stress point has to stay on the yield surface, whether it contracts or expands. Mathematically this means that the total differential of f is zero during plastic deformation:

$$\frac{\partial f}{\partial p'}dp' + \frac{\partial f}{\partial q}dq + \frac{\partial f}{\partial p_0'}\frac{\partial p_0'}{\partial \varepsilon_p^p}d\varepsilon_p^p = 0 \tag{2.48}$$

In which the assumption has been made that the hardening parameter p_0' only depends on the volumetric plastic strain ε_p^p. The relation between these parameters can be expressed in terms of λ^* and κ^* by using the following relation.

$$d\varepsilon_p^p = d\varepsilon_p - d\varepsilon_p^e = (\lambda^* - \kappa^*)\,\frac{dp'}{p'} \tag{2.49}$$

During isotropic consolidation p' is equal to p'_0. With this information equation (2.49) becomes:

$$\frac{dp'_0}{d\varepsilon_p^p} = \frac{p'_0}{\lambda^* - \kappa^*} = H \tag{2.50}$$

Which gives the relation between a change in the hardening parameter dp'_0 and a change in the plastic volumetric strain $d\varepsilon_p^p$. Using equation (2.50) and (2.47), the consistency equation (2.48) can be written as:

$$M^2(2p' - p'_0)dp' + 2qdq - M^2p'H\Omega M^2(2p' - p'_0) = 0 \tag{2.51}$$

Solving for Ω gives:

$$\Omega = \frac{dp'}{M^2p'H} + \frac{2qdq}{M^4p'H(2p' - p'_0)} \tag{2.52}$$

Now the plastic strains given in equation (2.47) are fully defined. The total change in strain during plastic yielding can easily be obtained by summing the elastic and plastic contributions which are both function of dp' and dq. In previous derivations the moduli λ^* and κ^* which relate the volumetric strain and the effective mean stress were used. These parameters are closely related to the moduli λ and κ which are defined in the $(\nu - ln(p'))$ space, where ν represents specific volume. The following relation can be derived:

$$\lambda = \nu_0\lambda^* \tag{2.53}$$

$$\kappa = \nu_0\kappa^* \tag{2.54}$$

In which ν_0 represents the specific volume at zero volumetric strain. This relation is used in PLAXIS. If a volumetric strain increment is expressed as a volume change with respect to the current volume (instead of initial volume), ν_0 should be replaced by ν in the equations above. Using the initial volume corresponds to engineering strain and using the current volume corresponds to natural strain. The numerical code CODE_BRIGHT which is introduced in chapter 5 uses ν instead of ν_0 for instance. It should be noted that with this definition λ and λ^* can not both be constant. Having completely defined the behavior of the MCC we notice three different types of behavior depending on ratio of p' to p'_0.

- The yield surface for p' smaller than $p'_0/2$ is called the dry side of the yield surface [23]. Let's start at $q = 0$ and fix p' to a specific value on the dry side. This corresponds to a heavily overconsolidated soil. The differential stress q is now increased untill the yield surface is reached. Before this happens the CSL will be crossed, but it will have no effect for the heavily overconsolidated soil. When the stress state reaches the yield surface negative plastic volumetric strain will be generated because the gradient of the yield surface points in the negative p'-direction. The negative plastic volumetric strain causes the yield surface to shrink. In order for the consistency equation to hold the differential stress q has to decrease accordingly. It will decrease until it reaches the CSL at the point $(p'_0/2, Mp'_0/2)$, see next bullet point.

- Let's now fix p' to $p'_0/2$ and increase the differential stress q until the yield surface is reached. This point in the stress space corresponds to the mid-point of the ellipse which lies on the CSL. The gradient of the yield surface has a non-zero component only in the q direction. This means that $d\varepsilon_p^p$ is zero. Therefore the yield surface will not move and the plastic multiplier Ω goes to infinity. At this stress state an infinite amount of plastic shear strain ε_q^p is generated according to the MCC. The soil collapses

- Finally we can consider what happens on the wet side of the yield curve, where p' is greater than $p'_0/2$. The gradient of the yield function points in the direction of positive direction which means that positive volumetric strain will be generated and the yield surface will expand accordingly. If q is increased, the yield surface will keep expanding until the CSL is reached. At this point an infinite amount of plastic shear strain is generated.

2.3.2 Barcelona Basic Model

In this section a short summary of the main features of the Barcelona Basic Model (BBM) is given. The original version was presented by Alonso, Gens and Josa in 1990 [5]. Traditionally much effort had been

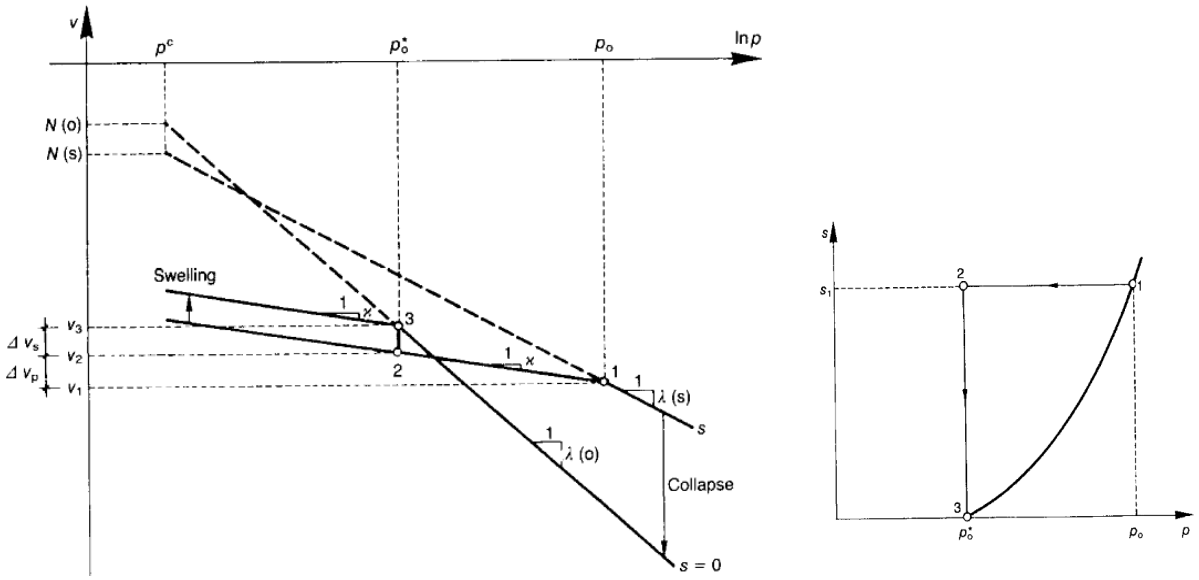

Figure 2.10: Left: Specific volume (ν) versus the logarithm of excess mean stress over air pressure ln(p). The pre-yielding stiffness is indicated by χ but is often also denoted by κ. The stiffness during yielding is represented by λ and it depends on suction in this model. Right: A stress path in p-s space. The yield surface is represented by the solid black curve. Figures from [5]

put in attempts to describe the mechanical behavior of soils when using only one stress variable such as the effective stress. Contributions from several researchers such as Bishop, Fredlund and Morgenstern during the 1960's to 1980's lead to the proposition of using a pair of independent stress variables such as the excess of total stress over air (p) and the suction (s) in order to describe the mechanical behavior of unsaturated soils. Alonso, Gens and Josa used this idea for developing a constitutive model, the BBM. In this model the stiffness of a soil during yielding, $\lambda(s)$, is assumed to be dependent on the suction. This can be seen in figure 2.10a. The elastic loading/reloading stiffness χ or κ is for simplicity assumed to be independent of suction. In later versions or the BBM, including the temperature dependent one, κ does have a suction dependency. This suction dependency of λ is in line with the experimental results displayed in figure (2.12). This figure shows that the elastic stiffness also depends on the suction, but less than the plastic stiffness. The specific volume of a soil under isotropic loading along virgin states is expressed with the following equation.

$$\nu = N(s) - \lambda(s) ln\left(\frac{p}{p^c}\right) = N(s) - \lambda(s)\left(ln(p) - ln(p^c)\right) \tag{2.55}$$

This describes the straight lines with slope λ in figure 2.10a. p^c is a reference stress and $N(s)$ is the specific volume corresponding to this reference stress. Now consider a soil with suction s, mean stress p^c and specific volume $N(s)$. When the suction is kept constant and the soil is loaded to the mean stress p_0, mean stress/specific volume state (1) will be reached, see figure 2.10a. The soil is then unloaded at constant suction to mean stress p_0^*, which is indicated by state (2). If the mean stress is now kept constant and the soil is wetted up till full saturation (i.e. suction decreases), the yield surface is reached again at point (3) and the soil is about to exhibit plastic deformation again. The same stress-suction path is displayed in figure 2.10b. The stress state of the soil at point (1) is positioned on the yield surface. Reduction of the mean stress results in departure from the yield surface, elastic behavior of the soil takes place. When the suction is then decreased the soil experiences an elastic swelling and the stress state of the soil will approach the yield surface again. p_0^* can be interpreted as the preconsolidation pressure at zero suction. When the suction increases the (apparent) preconsolidation pressure p_0 increases. The elastic range of the soil is extended. If on the other hand the mean stress p_0 would have been kept constant at point (1) and the suction would have been decreased, the soil would have experienced a plastic deformation during this entire stress path. This effect is called 'collapse' in figure 2.10a and the yield surface in figure 2.10b is therefore called the load collapse (LC) curve. Additionally there is also a suction increase (SI) yield surface in the BBM, even though it is not shown in 2.10b. The (SI) yield surface represents the stress states at which yielding due to a further increase in suction will initiate.

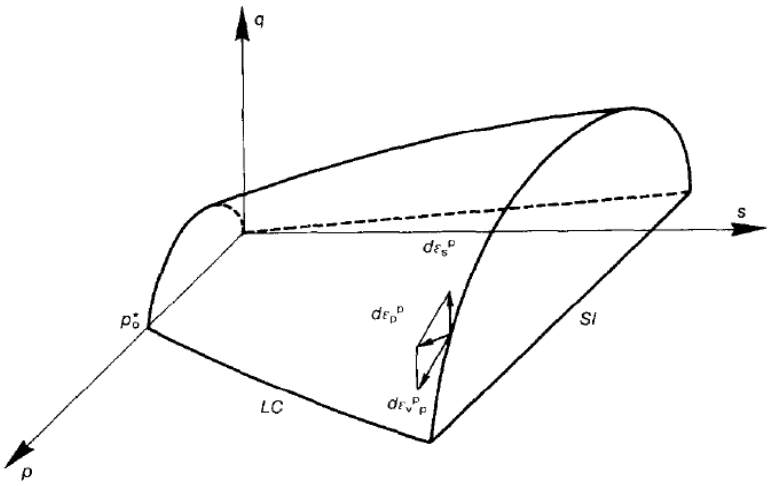

Figure 2.11: BBM yield surface in s, p, q space: Note the similarity with the yield surface of the MCC displayed in figure 2.9a. Figure from [5].

The (LC) and (SI) yield surfaces are assumed to be coupled by the total plastic volumetric strain. The hardening laws for the (LC) and (SI) yield surfaces both depend on the change in total plastic volumetric strain irrespective of its origin. The BBM is formulated as an extension of the Modified Cam Clay model. Figure 2.11 displays the yield surfaces of the BBM. When the soil is fully saturated (i.e. suction s = 0) the yield surface is equal to the MCC yield surface displayed in figure 2.9a. For the complete mathematical description the reader is referred to [5]. As will be mentioned in chapter 5, the temperature extended BBM uses a temperature dependent suction yield surface (SI) and load collapse (LC) yield surface [37]. The soil stiffness also depends on the suction which in turn depends on the temperature through a temperature dependent retention curve.

2.4 Temperature dependence of parameters

Many parameters and relations used in soil mechanics depend on temperature. The current PLAXIS implementation described in section 3.1 already implements several of those. The retention curve is a relation that depends on the temperature, as was explained in section 2.2.5. This temperature dependence can be expressed by [57]:

$$\frac{p_w(T)}{p_w(T_r)} = \left(\frac{a_1 + b_1 T}{a_1 + b_1 T_r}\right)^{b_1} \tag{2.56}$$

In which the parameters a_1 and b_1 are empirical and T_r is a reference temperature. The viscosity of water depends also on the temperature. Water becomes less viscous with increasing temperature. This in turn increases the permeability. Romero and Gens [39]have suggested the following expression for the temperature dependent permeability:

$$k_w(e, w, T) = \kappa^{int}(1 + \alpha_T(T - T_0))10^{ae}\left(\frac{w - w_{ref}}{\frac{e}{Gs} - w_{ref}}\right)^{\lambda} \tag{2.57}$$

In which a and G are empirical functions related to a_1 and b_1 in equation (2.56). λ and α_T are also empirical parameters where the latter has the units K^{-1}. It is used for fitting the relative viscosity over a temperature range. The void ratio is represented by e and suction by s. T_0 is a reference temperature and w_{ref} is a reference water content.

Literature [57] suggests that the effect of temperature on the permeability is significant particularly close to the saturated state due to the temperature dependence of the viscosity. At levels of saturation below 70% the temperature seems to have little effect on the permeability.

Wu [57] shows that the mechanical behavior of soils also depends on temperature. Wu argues that there are two types of soils that exhibit a different class of behavior with respect to changes in temperature. First there is a class of soils that is relatively stable. These soils are characterized by a low-porosity packing. Soils in this class experience swelling when subjected to drained heating or wetting. Then there is also a meta-stable group of soils characterized by high-porosity packing. These soils have a tendency

to collapse when wetted or subjected to drained heating. All the experimental evidence presented by Wu which supports the division of soils into two groups has been done on Boom-clays. It is therefore advisable to keep in mind that this behavior may not apply to other types of soils. The temperature induced swelling of low-porosity packed Boom-clays can have a plastic component as illustrated in Figure 2.12a. A constant net vertical stress is applied to the soils in an oedometer and the suction is kept fixed. A cyclic temperature change is then applied and the volumetric strain response of the soil is measured. The volumetric strain of a Boom-clay with an initial suction of $0.20MPa$ is initially very low, until a temperature of $40°C$ is reached (corresponding to the open circle denoted as the yield point). From this point on the volumetric strain increases much faster with temperature, until the maximum temperature of $80°C$ is reached. When the temperature is then lowered to the initial temperature of $20°C$, it turns out that most of the strain is not recovered. The temperature cycle resulted in an irrecoverable swelling, a thermal plastic strain. The sample with an initial suction of $0.06MPa$ shows a similar pattern, with the exception that the thermal yield surface is triggered almost immediately. The thermal expansion suggests that the samples that were tested were relatively stable.

A normally consolidated Boom-clay (i.e. relatively high porosity packing) will experience collapse when subjected to a heating cycle. The suggestion has been made by Towhata et al. [53] that volume reduction is caused by the increased mobility of water molecules at higher temperature. The charged surfaces of clay particles attract the water dipoles. This results in a layer of water molecules with a very high apparent viscosity. When the temperature increases, the amount of bound molecules decreases since more molecules will have the required kinetic energy to escape. The result is that the clay particles move closer together, which subsequently also results in an increased stiffness due to the increased amount of particle contact points. Apparently the volume reduction is not completely reversible when the temperature is lowered to its initial values again.

The stiffness of clay also displays a temperature dependency when the suction is constant during unloading-reloading in a oedometer. This is illustrated by figure 2.12b, which is taken from [57]. κ_{oed} represents the pre-yielding stiffness , which shows relatively little dependence on temperature and suction. The post-yielding stiffness λ_{oed} displays a larger range of variation. The reader is reminded that a smaller value of κ_{oed} and λ_{oed} represents a stiffer material. The clay seems to become less stiff with increasing temperature. No information is given about whether the soil was closely packed or not prior to the temperature increment. The previous discussion demonstrated that a soil in a high-porosity configuration exhibits a very different volumetric behavior when subjected to a temperature increment than a closely packed soil. A clay with high-porosity packing will experience an irreversible contraction when subjected to heating. The now more densely packed clay will have more particle contact points which will increase the stiffness [53]. The opposite can be expected for a soil that was already close packed prior to heating. Since the initial configuration of the clay determines whether it expands or contracts after heating, it will also determine whether the amount of particle contacts (and therefore the stiffness) increases or decreases as a result of heating. Since the stiffness of the clay in figure 2.12b seems to decrease with temperature, it seems reasonable to assume that it was initially highly compacted. But this deduction should be verified first before the trends displayed in figure 2.12b would be implemented in a constitutive model. Obtaining experimental results for other soil types would also be advisable, since they could exhibit a different behavior than the Boom clays that were investigated.

Wu used these previously presented experimental results to create an extended version of the cap-cone constitutive model. In addition to the net mean stress p' and the deviatoric stress q, the suction s and the temperature T are used. This results in a four-dimensional yield surface. The volumetric plastic strain is used as the internal state variable. For more details the interested reader is referred to [57].

The Suction Increase (SI) and Suction Decrease (SD) yield surfaces have a strong temperature dependence. The same applies to the Load Collapse (LC) yield surface. The (LC) and (SI) yield surfaces are presented in section 2.3.2 dealing with the Barcelona Basic Model. The temperature dependency of the (LC) yield curve means that the apparent pre-consolidation stress of the clay decreases with temperature. This stresses the importance of using a constitutive model for unsaturated clays (and possibly also soils) that integrates the temperature, such as the one proposed by Wu [57].

The temperature dependence of the mechanical behavior is limited to linear elastic thermal expansion in the current PLAXIS THM-implementation, see equation (3.55). No attempt has yet been made to model thermal plastic strain, temperature dependent stiffness, temperature dependent SI/SD yield surfaces and temperature dependent apparent preconsolidation pressure (LD yield surface). The previous discussion has shown the importance of these phenomena for unsaturated clays. Constitutive models that are capable of representing this behavior are planned to be implemented in later stages of the development process. Whether the temperature also has a significant effect on the mechanical behavior

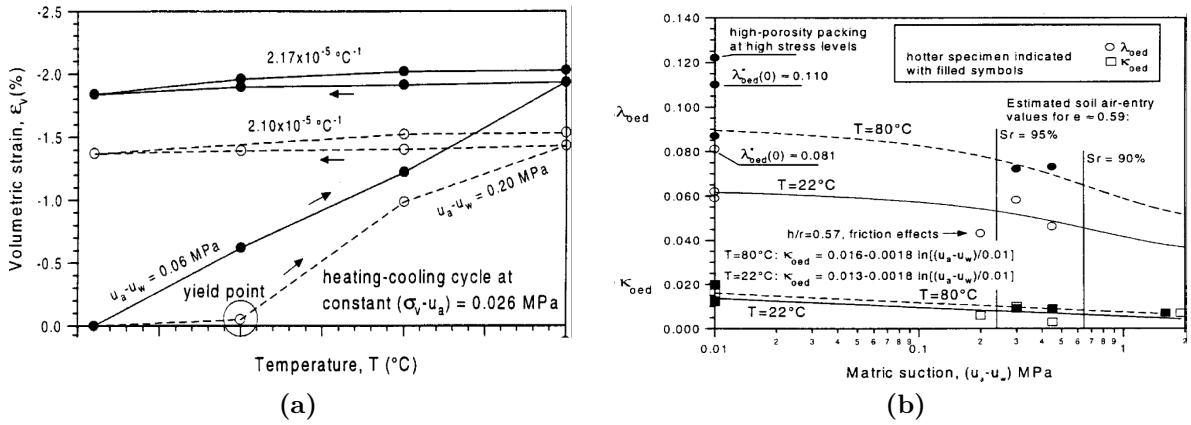

Figure 2.12: Left: Volumetric strain versus temperature for low-porosity packed Boom-clay subjected to a constant load and suction. Right: Oedometer stiffness parameters as function of suction for two different temperatures. Results from [57]

of other unsaturated soils or saturated soils should be investigated.

2.5 Finite element method

In this section a short introduction to the finite element method is given, based on the work of A. Segal [48]. The advection and diffusion of temperature in a porous medium will be used as an example since the equation that governs this process is linear and therefore relatively straight-forward to explain.

2.5.1 Finite element formulation

The advection-diffusion equation of temperature in a porous medium with constant velocity, density and heat capacity is of the form:

$$\frac{\partial T}{\partial t} = D\nabla^2 T - \mathbf{E} \cdot \nabla T \tag{2.58}$$

This equation can be derived directly from the energy balance equation in PLAXIS, see section 3.3 and 4.3.1. Constant D in equation (2.58) is the thermal diffusivity:

$$D = \frac{\lambda}{\rho C} \tag{2.59}$$

And $\mathbf{E}$ is an effective velocity vector:

$$E = \frac{\rho_w C_w \mathbf{V_w}}{\rho C} \tag{2.60}$$

The temperature on the domain Ω can be approximated in the following way:

$$T(\mathbf{x}, t) = \sum_{j=1}^{n} T_j(t)\phi_j(\mathbf{x}) + T_0(\mathbf{x}, t) \tag{2.61}$$

In which $\phi_j(\mathbf{x})$ are linearly independent basis functions that can be freely chosen and $T_j(t)$ are constant with respect to spatial parameters. $T_j(t)$ are to be determined. $T_0(\mathbf{x}, t)$ must be specified to match the non-homogeneous boundary conditions on boundary Γ of domain Ω. In general, if an approximation such as (2.61) would be directly inserted into a differential equation such as (2.58), the unknowns $T_j(t)$ can not be determined since an inconsistent set of equations would be obtained [38]. It is therefore usual to approximate the solution by multiplying it with a test function $v(\mathbf{x})$ and integrating it over the domain Ω. Equation 2.58 therefore becomes:

$$\int_\Omega v\frac{\partial T}{\partial t} d\Omega = \int_\Omega vD\nabla^2 T - v\mathbf{E} \cdot \nabla T d\Omega \tag{2.62}$$

For the integral to exist in equation (2.62), the $\nabla^2 T$ term has to be square integrable. This imposes certain continuity requirements on the test functions since the temperature is expressed in these (2.61).

For instance, if the gradient of the temperature would be discontinuous at a point the Laplacian would be undefined there. Similarly v has to be square integrable, but since no derivates of this function appear in equation (2.62) its gradient can be discontinuous. With the Gauss divergence theorem:

$$\int_\Omega vD\nabla^2 T = -\int_\Omega \nabla v \cdot D\nabla T d\Omega + \int_\Gamma vD\nabla T \cdot \mathbf{n} d\Gamma \tag{2.63}$$

the continuity requirements on T can be reduced, leading to the so called 'weak form'.

$$\int_\Omega v\frac{\partial T}{\partial t} d\Omega + \int_\Omega \left\{ \nabla v \cdot D\nabla T + v\mathbf{E} \cdot \nabla T \right\} d\Omega = \int_\Gamma vD\nabla T \cdot \mathbf{n} d\Gamma \tag{2.64}$$

In which the vector $\mathbf{n}$ is normal to the boundary Γ. In this weak form both the test function v and the basis functions from equation (2.61) have to be continuous so that the gradient is defined. Since the Laplacian of the temperature does not appear anymore in these equations the continuity restrictions on the test functions that accompany it are no longer required. The choice of allowable test functions is larger in the weak form. On boundaries where the temperature is specified the test function v is required to be zero. This is characteristic for an essential boundary condition. On boundaries where the heat flux is specified this heat flux can be entered in the boundary integral of equation (2.64). The heat flux is an example of a so called natural boundary condition. No requirements for test function v apply to such a boundary. Inserting equation (2.61) into equation (2.64) gives:

$$\begin{aligned} &\sum_{j=1}^{n} \frac{\partial T_j}{\partial t} \int_\Omega v\phi_j d\Omega + \sum_{j=1}^{n} T_j \int_\Omega \nabla v \cdot D\nabla \phi_j + v\mathbf{E} \cdot \nabla \phi_j d\Omega = \\ &\int_{\Gamma_h} vg d\Gamma_h - \int_\Omega v\frac{\partial T_0}{\partial t} d\Omega - \int_\Omega \nabla v \cdot D\nabla T_0 d\Omega - \int_\Omega v\mathbf{E} \cdot \nabla T_0 d\Omega \end{aligned} \tag{2.65}$$

In which the boundary integral now only goes over the part of the boundary Γ_h where the heat flux is specified. It now contains the function g which follows from the prescribed boundary heat flux. The unknowns T_j and $\frac{\partial T_j}{\partial t}$ could be moved outside of the integrals since they are not functions of the spatial independent variables $\mathbf{x}$. All vectors contain n elements. In the next section about timestepping it is shown that the time derivatives of the temperature can be approximated by a temperature difference divided by time. The total amount of unknowns in each timestep will be n. A complete set of n equations is therefore required to solve these n unknowns. This can be done by selecting n linearly independent test functions v_i. The so-called Galerkin method defines the test functions as:

$$v_i = \phi_i \ , \quad (i = 1, 2, ..., n) \tag{2.66}$$

With this choice the Galerkin formulation is finally derived. In matrix form this can be written as:

$$\mathbf{M}\dot{\mathbf{T}} + \mathbf{S}\mathbf{T} = \mathbf{F} \tag{2.67}$$

In which $\dot{T}$ is short hand for the vector containing the time derivatives $\frac{\partial T_j}{\partial t}$. T and F are also vectors and $\mathbf{M}$ and $\mathbf{S}$ are matrices. The elements of the matrices and right hand side (RHS) vector F are defined as:

$$m_{ij} = \int_\Omega \phi_i \phi_j d\Omega \tag{2.68}$$

$$S_{ij} = \int_\Omega \left\{ D\nabla \phi_i \cdot \nabla \phi_j + \phi_i \mathbf{E} \cdot \phi_j \right\} d\Omega \tag{2.69}$$

$$F_i = \int_{\Gamma_h} \phi_i g d\Gamma_h - \int_\Omega \phi_i \frac{\partial T_0}{\partial t} d\Omega - \int_\Omega D\nabla \phi_i \cdot T_0 d\Omega - \int_\Omega \phi_i \mathbf{E} \cdot \nabla T_0 d\Omega \tag{2.70}$$

They follow directly from inserting (2.66) in equation (2.65). Up till now it has only been mentioned that the shape functions should be linearly independent but that they can be chosen freely. In the finite element method these shape functions are interpolation functions. They are equal to one at node j to which they correspond and zero on all other nodes. From equations (2.61) it follows that the unknown T_j represents the value at node j, since all interpolation functions except ϕ_j are zero there. The PLAXIS interpolation functions presented in section 3.5 can serve as example. Examples of interpolation techniques required to compute (2.68)-(2.70) are also given in this section.

2.5.2 Timestepping

The system of linear differential equations (2.67) can be solved in multiple ways. In most solvers the time derivative $\dot{T}$ is approximated in the following way:

$$\dot{\mathbf{T}} = \frac{\mathbf{T^{k+1}} - \mathbf{T^{k}}}{\Delta t} \tag{2.71}$$

In which k is used for the current time level and $k+1$ for the next one. The θ-method expresses the vectors **ST** and **F** as a convex combination at time level k and k+1:

$$\mathbf{M}\frac{\mathbf{T}^{k+1} - \mathbf{T}^{k}}{\Delta t} + \theta\mathbf{S}\mathbf{T}^{k+1} + (1-\theta)\mathbf{S}\mathbf{T}^{k} = \theta\mathbf{F}^{k+1} + (1-\theta)\mathbf{F}^{k} \ , \ 0 \leq \theta \leq 1 \tag{2.72}$$

An explicit method has $\theta = 0$ and a fully implicit method has $\theta = 1$. Explicit methods are normally a lot faster than implicit methods, since the latter always require the solving of a set of equations. A disadvantage of explicit methods is that they can give rise to stability problems if the timestep is not small enough. A fully implicit method on the other hand is unconditionally stable. If θ is chosen to be one, just as in PLAXIS, equation (2.72) reduces to:

$$\left(\mathbf{M} + \Delta t\mathbf{S}\right)\mathbf{T}^{k+1} = \mathbf{M}\mathbf{T}^{k} + \Delta t\mathbf{F}^{k+1} \tag{2.73}$$

This system has n equations and n unknowns. For each timestep the linear system of equation (2.73) has to be solved. This procedure is described in section 2.7. The advection-diffusion equation described in this section was linear under the assumptions presented. If the velocity would have depended on the temperature (through viscosity for instance), the partial differential equation (2.58) would have been non-linear. Such a problem can also be solved with the finite element method, but it requires non-linear iterations. This principle is explained in the next section.

2.6 Non-linear solution schemes

Under the assumptions presented in previous section, the advection diffusion equation can be solved as a linear set of equations, (2.73). If matrix **M**, **S** and vector **F** would have depended on the unknowns **T**, the fully implicit solution scheme would have become:

$$\left(\mathbf{M}^{k+1} + \Delta t\mathbf{S}^{k+1}\right)\mathbf{T}^{k+1} = \mathbf{M}^{k+1}\mathbf{T}^{k} + \Delta t\mathbf{F}^{k+1} \tag{2.74}$$

This set of equations is non-linear in the unknowns $\mathbf{T}^{k+1}$. The most common numerical method to solve such a system of equations is the Newton-Raphson method. Equation (2.74) can be rewritten to: [7]

$$\mathbf{R}\left(\mathbf{T}^{k+1}\right) = \left(\mathbf{M}^{k+1} + \Delta t\mathbf{S}^{k+1}\right)\mathbf{T}^{k+1} - \Delta t\mathbf{F}^{k+1} - \mathbf{M}^{k+1}\mathbf{T}^{k} = \mathbf{0} \tag{2.75}$$

In order to find the correct vector of unknowns $\mathbf{T}^{k+1}$ that solves equation (2.75) a series of approximations $\mathbf{T}_i^{k+1}$ will be done until $\mathbf{R}\left(\mathbf{T}_i^{k+1}\right)$ has approached $\mathbf{0}$ up to a satisfactory degree. The series of estimates $\mathbf{T}_i^{k+1}$ are based on a first order Taylor approximations of the form:

$$\mathbf{R}\left(\mathbf{T}_{i+1}^{k+1}\right) \approx \mathbf{R}\left(\mathbf{T}_i^{k+1}\right) + \mathbf{K}d\mathbf{T}_i^{k+1} = \mathbf{0} \tag{2.76}$$

This equation forms the basis of the iterative Newton-Raphson scheme. Matrix **K** is usually referred to as the stiffness matrix and is defined as:

$$\mathbf{K} = \begin{pmatrix} \frac{\partial R_1\left(\mathbf{T}^{k+1}\right)}{\partial T_1^{k+1}} & \frac{\partial R_1\left(\mathbf{T}^{k+1}\right)}{\partial T_2^{k+1}} & \cdots & \frac{\partial R_1\left(\mathbf{T}^{k+1}\right)}{\partial T_n^{k+1}} \\ \frac{\partial R_2\left(\mathbf{T}^{k+1}\right)}{\partial T_1^{k+1}} & \frac{\partial R_2\left(\mathbf{T}^{k+1}\right)}{\partial T_2^{k+1}} & & \\ \vdots & & \ddots & \\ \frac{\partial R_n\left(\mathbf{T}^{k+1}\right)}{\partial T_1^{k+1}} & & & \frac{\partial R_n\left(\mathbf{T}^{k+1}\right)}{\partial T_n^{k+1}} \end{pmatrix}_{\mathbf{T}^{k+1}=\mathbf{T}_i^{k+1}} \tag{2.77}$$

In which the subscript j in T_j^{k+1} and $R_j\left(\mathbf{T}^{k+1}\right)$ represent the j-th element of their respective vector. The stiffness matrix contains the derivatives of vector $\mathbf{R}\left(\mathbf{T^{k+1}}\right)$ with respect to the unknowns $\mathbf{T}^{k+1}$.

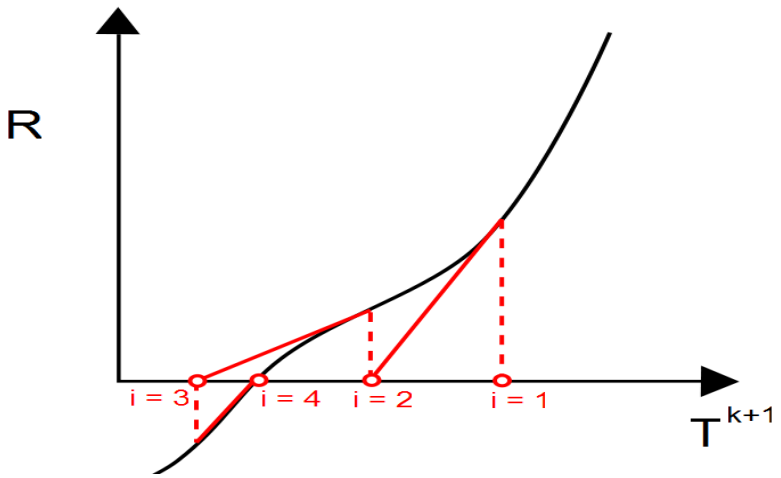

Figure 2.13: Iterative Newton-Raphson scheme illustrated for a one-dimensional case. At each iteration the slope 'K' of the curve is calculated. This slope is used to calculate the next estimate for T^{k+1}. In this example the approximation is close enough to zero at iteration 4.

Expressions for these derivatives are obtained in an analytical way. They are then evaluated at the temperature vector $\mathbf{T}^{k+1} = \mathbf{T}_i^{k+1}$ of the current iteration i. Equation (2.76) can be used to estimate the change in the temperature vector $d\mathbf{T}_i^{k+1}$ in iteration i.

$$\mathbf{K} d\mathbf{T}_i^{k+1} = -\mathbf{R}\left(\mathbf{T}_i^{k+1}\right) \tag{2.78}$$

The temperature vector at the next iteration therefore becomes:

$$\mathbf{T}_{i+1}^{k+1} = \mathbf{T}_i^{k+1} + d\mathbf{T}_i^{k+1} \tag{2.79}$$

With this new estimate the vector $\mathbf{R}\left(\mathbf{T}_{i+1}^{k+1}\right)$ can be evaluated. Due to the non-linearity of equation (2.74) this new vector $\mathbf{R}\left(\mathbf{T}_{i+1}^{k+1}\right)$ obtained by a first order Taylor approximation will most likely not be zero. Vector $\mathbf{R}\left(\mathbf{T}_{i+1}^{k+1}\right)$ will instead serve as starting point for the next iteration as defined by equation (2.76). Iterations will continue until $\mathbf{0}$ has been approached up to a satisfactory level. Vector norms can be used to measure this distance. The tolerance setting in PLAXIS is used to specify the minimum convergence that has to be achieved. A one-dimensional example to illustrate the Newton-Raphson technique is given in figure 2.13. The Newton-Raphson method generally has very fast convergence if it converges. Divergence is possible though if the initial guess for the first iteration is unfavorable.

2.7 Linear solvers

Within each non-linear iteration a linear systems of equations such as (2.78) has to be solved which has the form:

$$Ax = b \qquad A \in \mathbb{R}^{n \times n},\ x \in \mathbb{R}^n,\ b \in \mathbb{R}^n \tag{2.80}$$

In which vector x is the desired unknown. The most straight-forward way to obtain x would be to multiply both sides of the equation with the inverse of (non-singular) matrix A. But the computation of the inverse of a matrix is very expensive. Therefore several other solution strategies have been developed. This field of research is still evolving. The solution methods are normally subdivided into direct methods and in iterative methods. The intention of this section is to give a short introduction in both groups of solution strategies.

2.7.1 Direct solution methods

A well known algorithm from this group of linear solvers is the LU-decomposition. The explanation for this method is based on the work of C. Vuik [55]. The matrix A is decomposed into a Lower-triangular and an Upper-triangular matrix in such a way that the product LU will yield the original matrix A. With the principle of Gaussian elimination these triangular matrices can be used to solve x in equation (2.80).

The upper diagonal matrix U is computed by subsequently multiplying matrix A with a Gauss transformation matrix M_k.

$$M_{n-1}M_{n-2}...M_2M_1A = U \tag{2.81}$$

The structure of matrix M_{k-1} will result in removal of all lower diagonal entries in the $k-1$th column of matrix A_{k-1}. The latter can be defined as:

$$A^{(k-1)} = M_{k-1}...M_1A = \begin{bmatrix} A_{11}^{(k-1)} & A_{12}^{(k-1)} \\ 0 & A_{22}^{(k-1)} \end{bmatrix} \begin{matrix} k-1 \\ n-k+1 \end{matrix} \\ \begin{matrix} k-1 & n-k+1 \end{matrix} \tag{2.82}$$

In which the square block $A_{11}^{(k-1)}$ with dimensions $k-1$ has been made upper triangular already. Block $A_{22}^{(k-1)}$ is defined as:

$$A_{22}^{(k-1)} = \begin{bmatrix} a_{kk}^{(k-1)} & \cdots & a_{kn}^{(k-1)} \\ \vdots & & \vdots \\ a_{nk}^{(k-1)} & \cdots & a_{nn}^{(k-1)} \end{bmatrix} \tag{2.83}$$

The definition of Matrix M_k requires that $a_{kk}^{(k-1)}$ is non-zero. It contains the multipliers l_{ik}, which are defined as:

$$l_{ik} = a_{ik}^{(k-1)}/a_{kk}^{(k-1)} \qquad\qquad i = k+1, \cdots, n \tag{2.84}$$

Or in other words, multiplier l_{ik} divides the i-th entry in column k of matrix $A^{(k-1)}$ by the entry on the diagonal in that column. This is only done for entries below the diagonal. These multipliers are then used to create Gauss vector $\alpha^{(k)}$.

$$\alpha^{(k)} = (0, \cdots, 0, l_{k+1,k}, \cdots, l_{nk})^T \tag{2.85}$$

Gauss transformation matrix M_k is now defined as:

$$M_k = I - \alpha^{(k)}e_k^T \tag{2.86}$$

In which e_k is the k-th column of the identity matrix I. The product $\alpha^{(k)}e_k^T$ results in a matrix which is subtracted from the identity matrix. Matrix A^k is then obtained by multiplying M_k and $A^{(k-1)}$.

$$A^{(k)} = M_kA^{(k-1)} = \begin{bmatrix} 1 & 0 & & \cdots & 0 \\ 0 & \ddots & & & \\ & & 1 & & \\ \vdots & & -l_{k+1,k} & 1 & \\ & & \vdots & & \ddots \\ 0 & & -l_{n,k} & & 1 \end{bmatrix} A^{(k-1)} = \begin{bmatrix} A_{11}^{(k)} & A_{12}^{(k)} \\ 0 & A_{22}^{(k)} \end{bmatrix} \tag{2.87}$$

In which $A_{11}^{(k)}$ is again a square upper diagonal matrix, but now with dimensions k. The multipliers in the k-th column of matrix M_k have resulted in the removal of all the entries below the k-th diagonal in matrix $A^{(k-1)}$. The result is that the row and column dimensions of the upper diagonal part of matrix $A^{(k)}$ have increased by one compared to $A^{(k-1)}$. Repeating this procedure $n-1$ times according to equation (2.80) will finally give the upper diagonal matrix U.

The lower triangular matrix L can be obtained from equation (2.81) in the following way:

$$A = (M_{n-1}\cdots M_1)^{-1}M_{n-1}\cdots M_1A = (M_{n-1}\cdots M_1)^{-1}U = LU \tag{2.88}$$

In which L can be rewritten as:

$$L = (M_{n-1}\cdots M_1)^{-1} = M_{n-1}^{-1}\cdots M_1^{-1} = \prod_{i=1}^{n-1}\left(I + \alpha^{(i)}e_i^T\right) \tag{2.89}$$

The last step follows directly from the definition of the inverse. The determinant of matrix M_i is one and when the transpose of the matrix of cofactors is constructed the minus signs before vector $\alpha^{(i)}$ falls away. The product in the last step of (2.89) can be rewritten as:

$$L = \prod_{i=1}^{n-1}\left(I + \alpha^{(i)}e_i^T\right) = I + \sum_{i=1}^{n-1}\alpha^{(i)}e_i^T \tag{2.90}$$

The last step follows from the fact that multiplication of $\alpha^{(i)}e_i^T$ with $\alpha^{(i+1)}e_{i+1}^T$ returns a zero matrix. Equation (2.90) proves that matrix L is indeed lower triangular, with entries of 1 on the diagonal. Having decomposed the matrix A into L and U the vector x can be easily solved. Substituting $Ux = y$ the following system can be solved first:

$$Ly = b \tag{2.91}$$

Which is straight-forward due to the lower triangular nature of matrix L. Since vector y is now solved the unknown vector x can be computed directly due to the upper triangular nature of U.

$$Ux = y \tag{2.92}$$

The set of floating point numbers is a subset of the real numbers. Floating point operations can therefore naturally result in rounding errors. It can be proven [55] that the accuracy improves when the elements in the computed U and L matrices are small. Techniques have therefore been developed to reduce the magnitude of these elements. With a method called partial pivoting the rows and columns of matrix $A^{(k)}$ can be interchanged. With this operation the largest values of matrix $A^{(k)}$ can be placed on the diagonal. Because of this all the multipliers in α^{k+1} which directly appear in matrix L are smaller than one. This will improve the accuracy of the solution. Additionally, row and column interchanges are necessary when the diagonal contains elements that are zero since the LU algorithm would otherwise break down.

A downside of pivoting techniques is that they can destroy the band structure of matrix A. Banded matrices often appear during finite element discretization if proper element numbering techniques are used. It can be proven that the upper bandwidth of A is passed on to matrix U and the lower bandwidth of A is passed on to matrix L. Banded matrices are very preferable since they require far less memory for storage and the decomposition and solving can be done much faster. When rows and/or columns are interchanged during (partial) pivoting with the aim of improving the accuracy of the solution this banded structure can be destroyed, which results in a loss of all the beneficial traits of such matrices.

PLAXIS 2D currently uses the PARDISO solver from Intel's MKL library which is based on the principle of LU decomposition. It uses efficient storage techniques for sparse matrices and uses row/column permutations to reduce the amount of fill-in that can appear during LU decomposition [17]. Fill-in is the phenomenon that the zero entries of a sparse matrix are replaced by non-zero entries after LU decomposition which is not desirable since it requires more memory for storage. Having introduced the basics of direct solution methods it is interesting to turn to another category of solvers: the iterative solution methods.

2.7.2 Iterative solution methods

In the previous section it has been mentioned that the decomposition of A into L and U can introduce fill-in. Whenever matrix A is large and sparse the amount of work to create L and U and the amount of memory required to store them may be very large. In these situations it is beneficial to use iterative solution methods since they are usually memory efficient [49]. Iterative methods are of the form:

$$x^{(k+1)} = x^{(k)} + M^{-1}\left(b - Ax^{(k)}\right) \tag{2.93}$$

In which the choice of matrix M determines the iterative method. The residual $b - Ax^{(k)}$ from the k-th iteration is used to come to a new estimation $x^{(k+1)}$ of vector x. It is apparent that if this iteration process converges, x is a possible but not necessary solution. It is possible that a non-zero residual vector becomes close to zero after multiplication with matrix M^{-1}. It is therefore essential to always verify that the final estimate of x gives a residual that falls within the accuracy requirements. An example of the choice of M is the diagonal of matrix A. This choice leads to the point Gauss Jacobi method. It can be proven that any method of the form (2.93) will converge if the spectral radius ρ of the matrix $M^{-1}(M - A)$ is smaller than 1. The spectral radius is defined as: [55]

$$\rho(A) = \max\left(|\lambda|, \text{ where } \lambda \in \text{ spectrum of A}\right) \tag{2.94}$$

The spectrum of A is defined as the set of eigenvectors of matrix A. For the point Jacobi method the spectral radius is for instance always smaller than one if matrix A is strictly diagonally dominant (i.e. all elements on the diagonal are larger than the elements in the rest of the matrix). Other choices of M lead to the block Gauss Jacobi and the Gauss Seidel method for instance. A very popular method for symmetric and positive definite matrices (i.e. $x^T Ax > 0$ for any x) is the Conjugate Gradient (CG)

method. This method is also used in PLAXIS 3D [18].
Equation (2.80) is equivalent to finding the extremum of the following quadratic equation [49]:

$$f(x) = \frac{1}{2}x^T Ax - b^T x + c \tag{2.95}$$

as long as matrix A is symmetric. This follows from taking the gradient of equation (2.95) and recognizing that it should equals zero at the only extremum that the quadratic form has. If matrix A is also positive definite, then finding the point $x = A^{-1}b$ is equivalent to finding the (only) minimum point of the quadratic form (2.95). The most straightforward way to find this minimum is to follow the negative gradient (steepest descent) during each step of the iterative procedure and take the minimum in that direction. Even though this method will always converge, it turns out that it is not always the fastest way to reach the point $x = A^{-1}b$.

An idea is to use n search directions vectors d_i. If these search directions are linearly independent they can be used to construct any vector in $\mathbb{R}^n$. During step i of the iterative procedure we can add a scalar multiple $\alpha_{(i)}$ of search vector $d_{(i)}$ to $x_{(i)}$ in order to get $x_{(i+1)}$.

$$x_{(i+1)} = x_{(i)} + \alpha_{(i)} d_{(i)} \tag{2.96}$$

The (unknown!) error vector is defined as:

$$e_{(i)} = x_{(i)} - x \tag{2.97}$$

The error is closely related to the residual:

$$r_{(i)} = b - Ax_{(i)} = -Ae_{(i)} = -\nabla f(x_{(i)}) \tag{2.98}$$

The A-inner product is defined as:

$$(y, z)_A = y^T Az \tag{2.99}$$

If the vectors $d_{(i)}$ are chosen to be A-orthogonal (conjugate) to each other, requiring that $e_{(i+1)}$ is A-orthogonal to $d_{(i)}$ will allow us to express $\alpha_{(i)}$ in terms of the known matrix A, search vector d_i and residual $r_{(i)}$. It turns out that this is equivalent to finding the minimum $f(x_{(i+1)})$ along the search direction d_i.

$$d_{(i)}^T Ae_{(i+1)} = d_{(i)}^T r_{i+1} = -d_{(i)}^T \nabla f(x_{(i+1)}) = 0 \text{ (due to A-orthogonality of } d_{(i)} \text{ and } e_{(i+1)}) \tag{2.100}$$

The gradient $\nabla f(x_{(i+1)})$ is perpendicular to the search direction $d_{(i)}$ which means that $x_{(i+1)}$ is an extremum along that line (minimum due to positive definite nature of A). Equation (2.96) shows that $x_{(i)}$ is built up from a linear combination of all search directions $x_{(j)}$ with $i > j$. $x_{(i)}$ will therefore be a point on the hyperplane $x_{(0)} + \mathbb{D}_{(i)}$ with:

$$\mathbb{D}_{(i)} = \text{span}(d_{(0)}, \cdots, d_{(i-1)}) \tag{2.101}$$

It can be proven that the CG method chooses (through (2.96)) the point within this hyperplane for which $x_{(i)}$ gives the lowest 'energy norm' $||e_{(i)}||_A$.

$$||e_{(i)}||_A = (e_{(i)}, e_{(i)})_A = e_{(i)}^T Ae_{(i)} \tag{2.102}$$

In each iteration a new search direction is added to $x_{(i+1)}$ (2.96), and the 'energy' norm is guaranteed to be minimal for the linear combination of search directions $\mathbb{D}_{(i+1)}$ that are used. The search vectors are constructed from the n orthogonal residual vectors in the following way:

$$d_{(i+1)} = r_{(i+1)} + \beta_{(i+1)} d_{(i)}, \ \beta_{(i+1)} = \frac{r_{(i+1)}^T r_{(i+1)}}{r_{(i)}^T r_{(i)}} \tag{2.103}$$

When iteration n is performed, n linearly independent search vectors are used and any vector in $\mathbb{R}^n$ can be constructed, including x. $x_{(n)}$ is equal to x since this point corresponds to the lowest energy norm and the CG method always guarantees that the minimum energy norm is reached for the set of allowed vectors. The CG algorithm is therefore always guaranteed to converge in n steps even though it is possible that fortunate choice of x_0 will result in a combination of search vectors that allow faster construction of x. For large matrices it may not be feasible to perform all n iterations. If the residual

has reduced sufficiently (according to a set accuracy level) the iterative procedure can be stopped and the corresponding $x_{(i)}$ will be returned. Convergence is in general faster when the ratio $\lambda_{(1)}/\lambda_{(n)}$ is small (with $\lambda_{(1)} > \lambda_{(2)} > \cdots > \lambda_{(n)}$). The equipotential planes in the quadratic form (2.95) are then more spherical. If all the eigenvalues are equal then the equipotential planes are spherical and the residual, which points in the negative direction of the gradient (see equation 2.98), will point in the same direction as the error $e_{(0)}$. The first search vector $d_{(0)}$ is taken as $r_{(0)}$ so instant conversion will be achieved.

Multiplying both sides of equation (2.80) by a matrix B^{-1} gives:

$$B^{-1}Ax = B^{-1}b \tag{2.104}$$

By choosing a suitable matrix B the eigenvalues of matrix $B^{-1}A$ will be more clustered, which can improve the convergence behavior and result in faster computation of x. This technique is called preconditioning. Many choices for matrix B are available. Just as matrix A, matrix $B^{-1}A$ has to be positive determinate and symmetric for the CG-method to work. In this section about iterative methods I only scratched the surface of all the available methods. I would recommend the work of J.R. Shewchuk [49] to the interested reader for a full derivation and description of the CG-method.

2.7.3 LU decomposition vs CG

The CG method requires as many iterations as the dimensions of matrix A to obtain an exact solution. Since the dimensions of matrix A can be very large, the iterative procedure is usually stopped when the residual has decreased below a specified value. The speed of the CG solver therefore depends on the accuracy requirements that are imposed. Solvers based on the principle of LU-decomposition are less flexible, they always have to decompose matrix A into matrices L and U. For coarse meshes the matrix A will be small and LU decomposition will be faster than the CG-method. When the size of the matrix A grows with increasing mesh density, there will be a point at which the CG solver starts to outperform the solver based on LU decomposition.

During each time step in the finite element method, a non-linear set of equations has to be solved. This is usually done with the Newton-Raphson method described in section 2.6. For each non-linear iteration, a set of linear equations has to be solved according to equation (2.78). Selecting the right linear solver is therefore crucial for the performance of the finite element code. A mesh in PLAXIS 2D generally has less nodes than a mesh in PLAXIS 3D. For this reason PLAXIS 2D uses a solver based on the principle of LU-decomposition while PLAXIS 3D uses a CG solver.

CODE_BRIGHT gives the users the freedom to choose between a LU decomposition solver and a CG solver. If a CG solver is used it is important to tune its accuracy requirements on the non-linear tolerance level. For instance: using high non-linear tolerance in combination with very stringent linear accuracy requirements is undesirable. Even though the linear equations (2.78) during each non-linear iteration are solved with a very high level of accuracy, the final approximation for the unknown vector $\mathbf{T}_{i+1}^{k+1}$ in equation (2.79) would be relatively inaccurate. Solving the linear systems with a very high level of accuracy would in this case result in a waste of CPU time, demonstrating the importance of using consistent linear solver accuracy and non-linear tolerance.

Chapter 3

PLAXIS implementation

3.1 PLAXIS implementation of the balance equation

In this section the THM-equations are presented as they are implemented in PLAXIS. A detailed derivation of the balance equations was given in section 2.1. Table 3.1 contains all the symbols used.

3.2 Water mass balance

The water mass balance is described in the following way in PLAXIS [36], notice the close resemblance to equation (2.16).

$$\phi \frac{\partial}{\partial t}\left(S\rho_w + (1-S)\rho_v\right) + \left(S\rho_w + (1-S)\rho_v\right)\left[\frac{\partial \varepsilon_v}{\partial t} + \frac{(1-\phi)}{\rho_s}\frac{\partial \rho_s}{\partial t}\right] = -\nabla \cdot (\mathbf{J}_w + \mathbf{J}_v) \tag{3.1}$$

In which the following approximation has been made:

$$\rho_w \approx \rho_l^w \tag{3.2}$$

Which is reasonable since the mass of dissolved air in the liquid phase is negligible compared to the mass of water. Also, the variable ρ_v is used instead of ρ_g^w and p_w for p_l for convenience. The relative advective and diffusive fluxes for each phase that are present in equation (2.16) have been grouped together to form a liquid water- ($\mathbf{J}_w$) and a vapor- ($\mathbf{J}_v$) mass flux. PLAXIS uses the following formulation for the liquid water flux [36]:

$$\mathbf{J}_w = \rho_w \mathbf{V}_w = \rho_w \left(\frac{k_{rel}}{\mu}\kappa^{int}(\nabla p_w + \rho_w \mathbf{g})\right) \tag{3.3}$$

which only contains an advective component. The reader should be attentive of the sign convention used. PLAXIS uses the mechanical sign convention which means that tension is considered positive and pressure negative. So the equations are expressed in terms of tension instead of pressure. This often results in a change of sign in front of a pressure/tension term as can be seen in equation (3.8) for instance. The atmospheric air tension is used as a reference level. The water tension p_w and the absolute stress σ are also expressed relative to this level. The relative air tension is always assumed to be zero. The implications of this assumption are discussed in appendix B.

The dynamic viscosity μ which appears in the water flux equation (3.3) is a function of temperature. With increasing temperature the viscosity of water decreases and the permeability of the soil increases [57]. PLAXIS uses table (3.2) for the viscosity. Linear interpolation is performed and the viscosity outside the plotted domain is assumed to be constant.

Discussion about the temperature dependence of the permeability:
The permeability of a soil is defined as:

$$k_w = \frac{\kappa^{int}\rho_w g}{\mu} \tag{3.4}$$

The water flux which is implemented in PLAXIS is expressed in equation (3.3). This is approximately equivalent to:

$$\mathbf{J}_w = -k_w \nabla h \tag{3.5}$$

Table 3.1: A list of all the symbols used in the THM-description of PLAXIS. Bold face represents a vector. The term tension indicates that p is negative for compression.

Symbol	Description
t	Time (seconds)
x	Horizontal in-plane coordinate (m)
y	Vertical in-plane coordinate (m)
z	Out-of-plane coordinate (m)
S	Saturation (-)
T	Temperature (K)
ρ_w	Density of water ($kg\ m^{-3}$).
ρ_{w0}	Water density at reference pressure and temperature ($kg\ m^{-3}$).
ρ_v	Density of water vapor ($kg\ m^{-3}$).
$\rho_v s$	Saturated density of water vapor ($kg\ m^{-3}$).
ρ_s	Density of solid particles ($kg\ m^{-3}$).
ρ_m	Density of bulk soil (solids + water + gas) ($kg\ m^{-3}$).
μ	dynamic viscosity ($Pa\ s$)
$k_{rel}(S)$	Relative permeability: ratio of permability at given saturation to permeability in full saturation (-)
κ^{int}	Intrinsic permeability (m^2)
$\mathbf{V}_w$	Averaged water velocity on a plane (not physical velocity in pore) (ms^{-1})
$\mathbf{J}_w$	Mass flux of liquid water ($kg\ m^{-2}s^{-1}$)
$\mathbf{J}_v$	Mass flux of water vapor ($kg\ m^{-2}s^{-1}$)
ε_V	Volumetric Cauchy strain (-)
p_g^w	Partial water vapor tension (Pa)
p_g^w	Saturated partial water vapor tension (Pa)
θ	Relative humidity (-)
p_{atm}	Atmospheric reference tension
p_g	Relative (to atmospheric) gas tension
p_w	Relative water tension (Pa)
p_c	Suction (Pa)
β_{sT}	Volumetric expansion coefficient of soil grains (K^{-1})
$\beta_{DT,x}$	Skeletal thermal expansion coefficient in x-direction (K^{-1})
$\beta_{DT,y}$	Skeletal thermal expansion coefficient in y-direction (K^{-1})
$\beta_{DT,z}$	Skeletal thermal expansion coefficient in z-direction (K^{-1})

Symbol	Description
β_{wT}	Thermal expansion coefficient of water (K^{-1})
β_{wp}	Compressibility of water (Pa^{-1})
ϕ	Porosity (-)
χ	Parameter linked to the degree of saturation, introduced by Bishop (-)
$\mathbf{g}$	Gravity (ms^{-2})
m^w	Molar mass of water ($kg\ mol^{-1}$)
R	Gas constant ($J\ mol^{-1}K^{-1}$)
R_v	Specific gas constant for water vapor (461.5 $J\ kg^{-1}K^{-1}$)
f_{Tv}	Vapor diffusion enhancement factor (-)
D_v	Vapor diffusion coefficient (m^2s^{-1})
D_{v0}	Vapor diffusion coefficient for completely dry soil(m^2s^{-1})
D_{pv}	Hydraulic vapor diffusion coefficient ($kg\ m^{-1}s^{-1}Pa^{-1}$)
D_{Tv}	Hydraulic vapor diffusion coefficient ($kg\ K^{-1}m^{-1}s^{-1}$)
p_{w0}	Reference tension water (Pa)
T_0	Reference temperature (K)
C_s	Specific heat capacity of solid ($J\ kg^{-1}\ K^{-1}$)
C_w	Specific heat capacity of water ($J\ kg^{-1}\ K^{-1}$)
C_g	Specific heat capacity of gas ($J\ kg^{-1}\ K^{-1}$)
C_{as}	Convective heat transfer coefficient ($WK^{-1}m^{-2}$)
T_a	Air temperature at convective heat transfer boundary (K)
e_g	Internal energy of the gas phase per mass unit ($J\ kg^{-1}$)
e_w	Internal energy of the water phase per mass unit ($J\ kg^{-1}$)
e_s	Internal energy of the solid phase per mass unit ($J\ kg^{-1}$)
λ	Averaged thermal conductivity of the soil, water, gas mixture ($WK^{-1}m^{-1}$)
Q	Energy production per unit volume (Wm^{-3})

In which h represents the hydraulic head. With the current permeability implementation in PLAXIS which is given by equation (3.4) the permeability would keep increasing due to the monotonous decrease in viscosity with rising temperature.

Equation (2.57) also gives an empirical expression for the permeability that takes into account temperature variations. It might be an interesting alternative to the current permeability implementation in PLAXIS. The empirical parameters a and G can be expressed in a_1 and b_1 which are already used to describe the temperature dependence of the retention curve in PLAXIS, see equation (3.33). One of the goals of PLAXIS is to give accurate results while requiring as few input parameters as possible. Even though equation (2.57) contains the additional empirical parameter λ it might be possible to correlate it to other parameters. That way the user would not have to be confronted with new parameters that have to be determined in the laboratory.

In section 2.4 it was mentioned that Wu [57] indicates that the permeability does not have a large temperature dependence at saturation levels below 70%. One way to implement this behavior in PLAXIS would be to extend $k_{rel}(S)$ to $k_{rel}(S,T)$. At levels of saturation below 70% the change in the viscosity with temperature could be matched by a change in relative permeability. This way the permeability would remain unaffected by temperature at low saturation levels. Further research would be required to investigate whether this temperature extension of $k_{rel}(S)$ is feasible.

Having discussed the liquid water flux, it is now time to focus on the water vapor flux. The vapor flux in unsaturated soils is assumed to be completely diffusive in nature and can be expressed as [36]:

$$\mathbf{J}_v = -D_v \nabla \rho_v \tag{3.6}$$

Which is Fick's law of diffusion. D_v is the vapor diffusion coefficient in a porous material, which is a function of temperature, gas tension and sample tortuosity. It can be related to the saturation in the following way [8] [26] [11]:

$$D_v = D_{v0}(1 - S) \tag{3.7}$$

When the saturation increases, the pore space available for gas diffusion reduces. This means that a vapor density gradient of fixed magnitude should result in a smaller vapor mass flux. This is what equation (3.7) in combination with (3.6) represents. The vapor diffusion coefficient does not depend on temperature in the current implementation. Such a relation would make sense since molecular diffusion for a fixed density gradient would increase with temperature. The reason for this is that the molecules becomes more mobile. In section 4.2 the effect of the vapor flux and variable vapor diffusion coefficient is investigated.

The vapor flux is set to zero for points below the phreatic surface, since all the pores are assumed to be filled with water and no gas flux is possible. So the vapor flux is only defined in the unsaturated zone.

The reader is reminded that pressure variables are referred to as tension since they are positive for tension and negative for pressure. The partial tension of the water vapor can be expressed as a function of the suction which in turn is defined as the difference between the liquid water tension and the air tension.

$$p_c = -(p_g - p_w) \tag{3.8}$$

in which p_c indicates the capillary tension. Recall that the atmospheric and water tension terms are expressed relative to the atmospheric tension. The assumption was made that the relative gas tension is zero, so the capillary tension equals the water tension p_w. Due to the relation between capillary tension and partial vapor tension explained in section 2.2, the flux of water vapor can be expressed in terms of liquid water tension. Kelvin's relationship for relative humidity in a porous medium is given by [42]:

$$\theta = \frac{p_g^w}{p_{gS}^w} = exp\left(\frac{-p_c m^w}{\rho_w RT}\right) \tag{3.9}$$

In which m^w represents the molar mass of water. This is equivalent to:

$$\theta = \frac{p_g^w}{p_{gS}^w} = exp\left(\frac{-p_w}{\rho_w R_v T}\right) \tag{3.10}$$

In which R_v is the specific gas constant of water vapor. In deriving this expression the assumption has been made that the osmotic suction is negligible. With this assumption ψ in equation (2.35) can be

Table 3.2: Dynamic viscosity relative to the dynamic viscosity at $T = 20°C$ as implemented in PLAXIS [36].

Temperature ($°C$)	μ_T/μ_{20}
0	1.783433134
5	1.515968064
10	1.304391218
20	1.000000000
30	0.796407186
40	0.651696607
50	0.545908184
60	0.466067864
70	0.403193613
80	0.354291417
90	0.314371257
100	0.281437126

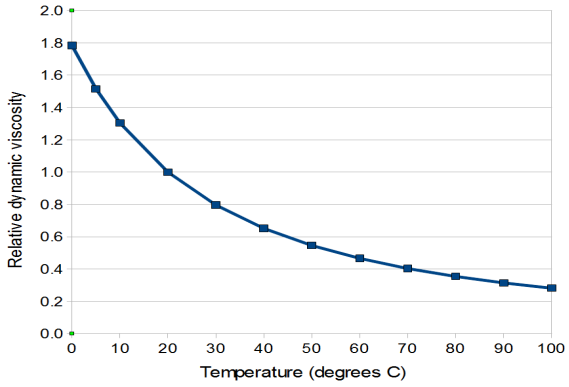

replaced with p_w and the same result would be obtained. Using the ideal gas law, the vapor density can be expressed as [42]:

$$\rho_v = \theta \rho_{vS} \tag{3.11}$$

Inserting equations (3.11) and (3.10) into (3.6) leads to:

$$\mathbf{J}_v = -D_v \nabla \rho_v = -D_v \nabla \left(\theta \rho_{vs}\right) = -D_v \left(\theta \nabla \rho_{vs} + \rho_{vs} \nabla \theta\right) = -D_v \left(\theta \frac{\partial \rho_{vs}}{\partial T} \nabla T + \rho_{vs} \left[\frac{\partial \theta}{\partial T} \nabla T + \frac{\partial \theta}{\partial p_w} \nabla p_w\right]\right) \tag{3.12}$$

Applying the chain rule leads to:

$$\frac{\partial \theta}{\partial T} = \frac{\theta p_w}{\rho_w R_v T^2} + \frac{\theta p_w}{\rho_w^2 R_v T} \frac{\partial \rho_w}{\partial T} \tag{3.13}$$

$$\frac{\partial \theta}{\partial p_w} = \frac{-\theta}{\rho_w R_v T} + \frac{\theta p_w}{\rho_w^2 R_v T} \frac{\partial \rho_w}{\partial p_w} \tag{3.14}$$

The following terms are neglected in equations (3.13) and (3.14) due to their relatively small magnitude:

$$\frac{\partial \rho_w}{\partial T} \frac{\theta p_w}{\rho_w^2 R_v T} \tag{3.15}$$

$$\frac{\partial \rho_w}{\partial p_w} \frac{\theta p_w}{\rho_w^2 R_v T} \tag{3.16}$$

Giving the final expressions:

$$\frac{\partial \theta}{\partial T} \approx \frac{\theta p_w}{\rho_w R_v T^2} \tag{3.17}$$

$$\frac{\partial \theta}{\partial p_w} \approx \frac{-\theta}{\rho_w R_v T} \tag{3.18}$$

Inserting equations (3.17) and (3.18) into equation (3.12) yields:

$$\mathbf{J}_v = -\left(D_v \left(\theta \frac{\partial \rho_{vS}}{\partial T} + \frac{\rho_v p_w}{\rho_w R_v T^2}\right) \nabla T - \frac{D_v \rho_v}{\rho_w R_v T} \nabla p_w\right) \tag{3.19}$$

This demonstrates that the vapor flux depends on the gradients of the liquid water tension and temperature. The vapor flux can now be written as:

$$\mathbf{J}_v = -\left(D_{Tv} \nabla T + D_{pv} \nabla p_w\right) \tag{3.20}$$

In which the hydraulic and thermal diffusion coefficients are respectively:

$$D_{pv} = D_v \frac{\partial \rho_v}{\partial p_w} \approx -\frac{D_v \rho_v}{\rho_w R_v T} \tag{3.21}$$

$$D_{Tv} = D_v \frac{\partial \rho_v}{\partial T} \approx D_v \left(\theta \frac{\partial \rho_{vS}}{\partial T} + \frac{\rho_v p_w}{\rho_w R_v T^2} \right) \tag{3.22}$$

The relation between saturated vapor density and temperature is described with an empirical function [56]:

$$\rho_{vS} = 10^{-3} \exp(19.891 - 4974/T) \tag{3.23}$$

Which completes the equations describing the vapor flux of water. The following expression is used for the liquid density of water:

$$\frac{\rho_w}{\rho_{w0}} = 1 - \beta_{wP} \left(p_w - p_{w0} \right) - \beta_{wT} \left(T - T_0 \right) \tag{3.24}$$

In which ρ_{w0} is the density of water at reference temperature T_0 and reference pressure p_{w0}. The derivative of water density with time therefore is:

$$\frac{\partial \rho_w}{\partial t} = \frac{\partial \rho_w}{\partial p_w} \frac{\partial p_w}{\partial t} + \frac{\partial \rho_w}{\partial T} \frac{\partial T}{\partial t} \approx -\beta_{wP} \rho_w \frac{\partial p_w}{\partial t} - \beta_{wT} \rho_w \frac{\partial T}{\partial t} \tag{3.25}$$

In which the approximation $\rho_{w0} \approx \rho_w$ has been made. With equation (3.25), the first term of the water mass balance equation (3.1) can now be rewritten as:

$$\begin{aligned} &\phi \frac{\partial}{\partial t} \left(S \rho_w + (1 - S) \rho_v \right) = \phi \rho_w \frac{\partial S}{\partial t} + \phi S \frac{\partial \rho_w}{\partial t} - \phi \rho_v \frac{\partial S}{\partial t} + \phi (1 - S) \frac{\partial \rho_v}{\partial t} \\ &= \phi \left(\frac{\partial S}{\partial p_w} \frac{\partial p_w}{\partial t} + \frac{\partial S}{\partial T} \frac{\partial T}{\partial t} \right) \rho_w + \phi S \left(-\rho_w \beta_{wP} \frac{\partial p_w}{\partial t} - \rho_w \beta_{wT} \frac{\partial T}{\partial t} \right) \\ &- \phi \rho_v \left(\frac{\partial S}{\partial p_w} \frac{\partial p_w}{\partial t} + \frac{\partial S}{\partial T} \frac{\partial T}{\partial t} \right) + \phi \left(1 - S \right) \frac{\partial \rho_v}{\partial t} \end{aligned} \tag{3.26}$$

When making the same assumptions (3.15) and (3.16) leading to (3.17) and (3.18), the last term in equation (3.26) can be rewritten as:

$$\begin{aligned} &\phi \left(1 - S \right) \frac{\partial \rho_v}{\partial t} = \phi (1 - S) \frac{\partial \theta \rho_{vs}}{\partial t} = \phi (1 - S) \left[\theta \frac{\partial \rho_{vs}}{\partial T} \frac{\partial T}{\partial t} + \rho_{vs} \left(\frac{\partial \theta}{\partial T} \frac{\partial T}{\partial t} + \frac{\partial \theta}{\partial p_w} \frac{\partial p_w}{\partial t} \right) \right] \\ &= \phi (1 - S) \left[\theta \frac{\partial \rho_{vs}}{\partial T} \frac{\partial T}{\partial t} + \rho_{vs} \left(-\frac{\partial p_w}{\partial t} \frac{\theta}{\rho_w R_v T} + \frac{\partial T}{\partial t} \frac{\theta p_w}{\rho_w R_v T^2} \right) \right] \\ &= \phi (1 - S) \left[\frac{\partial T}{\partial t} \left(\theta \frac{\partial \rho_{vs}}{\partial T} + \frac{p_w \rho_v}{\rho_w R_v T^2} \right) - \frac{\partial p_w}{\partial t} \frac{\rho_v}{\rho_w R_v T} \right] \end{aligned} \tag{3.27}$$

The following expression can be obtained from this:

$$\frac{\partial \rho_v}{\partial t} = \left[\frac{\partial T}{\partial t} \frac{D_{Tv}}{D_v} + \frac{\partial p_w}{\partial t} \frac{D_{pv}}{D_v} \right] \tag{3.28}$$

Note the close correspondence between equation (3.28) and the vapor flux (3.20). The time derivative of vapour density can be expressed in terms of the vapor diffusion coefficient D_v and the hydraulic and thermal diffusion coefficients D_{pv} and D_{Tv}. The term $\frac{D_{Tv}}{D_v}$ describes how much the vapor density changes per degree Kelvin and the term $\frac{D_{pv}}{D_v}$ represents the change in density per Pascal of pressure. Some finite element codes like ROCMAS [42] add a dimensionless thermal diffusion enhancement factor to control the magnitude of the vapor flux response to a temperature gradient. A new thermal diffusion coefficient D'_{pv} is in that case substituted for D_{pv}:

$$D'_{Tv} = f_{Tv} D_{Tv} \tag{3.29}$$

Such a thermal diffusion enhancement factor could in the future also be introduced in PLAXIS if this would result in a better match between numerical and experimental data. Equation (3.29) should then be substituted both in equation (3.20) and (3.28). This is necessary to get a consistent expression for the time derivative of the vapour flux. The time derivative of (3.20) and the gradient of (3.28) multiplied with $-D_v$ should be the same since the order of differentiation can be interchanged for a function with continuous derivatives.

$$-\frac{\partial \left(D_{Tv} \nabla T + D_{pv} \nabla p_w \right)}{\partial t} = -\frac{\partial D_v \nabla \rho_v}{\partial t} = \frac{\partial \mathbf{J}_v}{\partial t} = -D_v \nabla \left(\frac{\partial \rho_v}{\partial t} \right) = -D_v \nabla \left[\frac{\partial T}{\partial t} \frac{D_{Tv}}{D_v} + \frac{\partial p_w}{\partial t} \frac{D_{pv}}{D_v} \right] \tag{3.30}$$

The right hand side corresponds with equation (3.28) multiplied with $-D_v$. If the thermal diffusion enhancement factor would not be added simultaneously in equations (3.20) and (3.28), the LHS and the RHS of (3.30) would not have the same dependency on f_{Tv}. Equation (3.30) would not hold anymore, representing a contradiction.

Under the assumption that the solid density can be expressed in similar forms as (3.24) and the solid compressibility β_{sp} is negligible, the second term in equation (3.1) can be rewritten as [36]:

$$\begin{aligned}(S\rho_w + (1-S)\rho_v)\left[\frac{\partial \varepsilon_v}{\partial t} + \frac{(1-\phi)}{\rho_s}\frac{\partial \rho_s}{\partial t}\right] &= (S\rho_w + (1-S)\rho_v)\left[\frac{\partial \varepsilon_v}{\partial t} - (1-\phi)\beta_{sT}\frac{\partial T}{\partial t}\right] \\ &= (S\rho_w + (1-S)\rho_v)\frac{\partial \varepsilon_v}{\partial t} - (S\rho_w + (1-S)\rho_v)(1-\phi)\beta_{sT}\frac{\partial T}{\partial t} \end{aligned} \tag{3.31}$$

Inserting equations (3.26), (3.27) and (3.31) into (3.1) yields the final form of the water mass balance:

$$\begin{aligned}&\phi\left[(\rho_w - \rho_v)\frac{\partial S}{\partial p_w} - S\rho_w\beta_{wP} - (1-S)\frac{\rho_v}{\rho_w R_v T}\right]\frac{\partial p_w}{\partial t} \\ &+\left[\begin{array}{c}\phi(\rho_w - \rho_v)\frac{\partial S}{\partial T} - \phi S\rho_w\beta_{wT} + \phi(1-S)\left(\theta\frac{\partial \rho_{vS}}{\partial T} + \frac{\rho_v p_w}{\rho_w R_v T^2}\right) \\ -(S\rho_w + (1-S)\rho_v)(1-\phi)\beta_{sT}\end{array}\right]\frac{\partial T}{\partial t} \\ &+(S\rho_w + (1-S)\rho_v)\frac{\partial \varepsilon}{\partial t} + \nabla\cdot(\mathbf{J}_w + \mathbf{J}_v) = 0\end{aligned} \tag{3.32}$$

The temperature dependence of the retention curve in PLAXIS was already described in section 2.4, equation (2.56) [57]:

$$\frac{p_w(T)}{p_w(T_r)} = \left(\frac{a_1 + b_1 T}{a_1 + b_1 T_r}\right)^{b_1} \tag{3.33}$$

In which a_1 and b_1 are empirical functions that can depend on the saturation and T_r is a reference temperature. This temperature dependence of the suction is coupled to a Van Genuchten retention curve:

$$S(\phi_p, T) = S_{res} + (S_{sat} - S_{res})\left[1 + (g_{a,T}|\phi_p|)^{g_n}\right]^{g_c} \tag{3.34}$$

In which ϕ_p represents the pressure head at reference temperature [34].

$$\phi_p = -\frac{p_w}{\rho_w g} \tag{3.35}$$

and $g_{a,T}$ includes the temperature dependency:

$$g_{a,T} = g_a\left(\frac{a_1 + b_1 T}{a_1 + b_1 T_r}\right)^{b_1} \tag{3.36}$$

The coefficients g_a, g_n and g_c are empirical. S_{res} represents the residual saturation that remains even at high levels of suction. S_{sat} is the saturation of the soil when its pores are filled with water. Some air bubbles often remain so S_{sat} can be less than one.

In line with PLAXIS' philosophy it would be desirable to confront the end user only with empirical parameters that are essential. Research would be required to investigate whether the additional parameters a_1 and b_1 can be related to the empirical parameters g_c, g_a, void ratio and saturated permeability. Another option would be to extend the data sets that are already used for hydro-mechanical analysis in PLAXIS 2010. These data sets already suggest values for the permeability and g_c and g_a when a type of soil is selected. For instance, the USDA data set contains suggestions for soil types like silt, loamy sand, sandy clay and many more. When extended these groups could possibly also suggest values for the empirical parameters g_c, g_a for each soil type.

The following assumption is already made in the hydro-mechanical PLAXIS 2010 to reduce the amount of empirical parameters by one [34].

$$g_c = \left(\frac{1 - g_n}{g_n}\right) \tag{3.37}$$

It has been shown that the isothermal van Genuchten equation shows good agreement with experimental results for low and intermediate values of suction. The accuracy decreases at high levels of suction [34].

3.3 Energy balance

Equation (2.21) gives an expression for energy balance under the assumption that the solid velocity $\mathbf{v}_s$ is small.

$$\frac{\partial}{\partial t}\left(\phi S_l \rho_l e_l + \phi S_g \rho_g e_g + (1-\phi)\rho_s e_s\right) - Q^h = -\nabla \cdot \left(\mathbf{i}_m^h + \mathbf{q}_{rl}^h + \mathbf{q}_{rg}^h\right) \tag{3.38}$$

The diffusive heat flux in the porous multiphase medium is described by Fourier's law:

$$\mathbf{i}_m^h = -\lambda \nabla T \tag{3.39}$$

It is the result of the assumption that the individual diffusive heat fluxes of the phases can be represented by a single heat flux with the following expression for the thermal conductivity λ [36].

$$\lambda = (1-\phi)\lambda_s + \phi S \lambda_w + \phi(1-S)\lambda_g \tag{3.40}$$

In which λ_s, λ_l and λ_g represent the solid, liquid and gas thermal conductivities respectively. The general energy balance equation (3.38) contains two different advective energy terms. Each term also contains a contribution from the water and dry air components of the respective phase. In PLAXIS the advective energy flux is represented by only one term which is expected to be dominant: the energy advection due to the advection of liquid water. The energy balance equation now reduces to:

$$\frac{\partial}{\partial t}\left(\phi S_l \rho_l e_l + \phi S_g \rho_g e_g + (1-\phi)\rho_s e_s\right) = -\nabla \cdot \left(\mathbf{i}_m^h + \mathbf{J}_{Aw}\right) + Q^h \tag{3.41}$$

In which the following expression is used for the advective water energy flux $\mathbf{J}_{Aw}$

$$\mathbf{J}_{Aw} = C_w T \mathbf{J}_w = \rho_w C_w T \mathbf{V}_w \tag{3.42}$$

Where the vector $\mathbf{V}_w$ describes the velocity of the water and C_w is a specific heat capacity term. Equation (3.3) gives and expression for the velocity of water. Several physical phenomena can be captured by the source term Q^h. Examples are the energy production due to radioactive decay or the mechanical energy dissipation due to velocity gradients. PLAXIS uses the following description [36]:

$$Q^h = \sigma_w : \nabla \mathbf{V}_w + \sigma_s : \nabla \mathbf{V}_s + Q'^h = (\phi S_w p_w \nabla \cdot \mathbf{V}_w - \tau_w) + (1-\phi) 3K' \beta_{DT} \frac{\partial \varepsilon_v}{\partial t} + Q'^h \tag{3.43}$$

In which the first part of equation (3.43) represents mechanical energy dissipation and $Q^{'}$ represents other heat production terms like for instance radioactive decay. τ_w is a viscous energy dissipation term. The operator ':' represents double contraction with the following definition (using Einstein summation convention):

$$\mathbf{A} : \mathbf{B} = A_{ij} B_{ij} \tag{3.44}$$

But mechanical energy dissipation can be neglected in most practical applications [36]. The energy dissipation term is therefore not integrated in the current implementation. The LHS of equation (3.38) is simplified assuming local thermal equilibrium [36]:

$$\frac{\partial}{\partial t}\left(\phi S_l \rho_l e_l + \phi S_g \rho_g e_g + (1-\phi)\rho_s e_s\right) \approx C\rho \frac{\partial T}{\partial t} \tag{3.45}$$

In which:

$$C\rho = (1-\phi) C_s \rho_s + \phi S C_w \rho_w + \phi(1-S) C_g \rho_g \tag{3.46}$$

The divergence of the heat fluxes can be rewritten as:

$$-\nabla \cdot \left(\mathbf{i}_m^h + \mathbf{J}_{Aw}\right) = \nabla \cdot (\lambda \nabla T) - \nabla \cdot (\rho_w C_w T \mathbf{V}_w) \tag{3.47}$$

In which the last term becomes:

$$\begin{aligned} &\nabla \cdot (\rho_w C_w T \mathbf{V}_w) = C_w \left(\rho_w \mathbf{V}_w \cdot \nabla T + \rho_w T \nabla \cdot \mathbf{V}_w + T \mathbf{V}_w \cdot \nabla \rho_w\right) \\ &= C_w \left(\rho_w \nabla T + T \nabla \rho_w\right) \cdot \left(\frac{k_{rel}}{\mu} \kappa^{int} \left(\nabla p_w + \rho_w \mathbf{g}\right)\right) + \rho_w C_w T \left[\nabla \cdot \left(\frac{k_{rel}}{\mu} \kappa^{int} \left(\nabla p_w + \rho_w \mathbf{g}\right)\right)\right] \end{aligned} \tag{3.48}$$

With the equations (3.42) - (3.48), equation (3.41) becomes:

$$C\rho\frac{\partial T}{\partial t} - \nabla\cdot(\lambda\nabla T) + C_w\left(\rho_w\nabla T + T\nabla\rho_w\right)\left(\frac{k_{rel}}{\mu}\kappa^{int}\left(\nabla p_w + \rho_w\mathbf{g}\right)\right) + \rho_w C_w T\left[\nabla\cdot\left(\frac{k_{rel}}{\mu}\kappa^{int}\left(\nabla p_w + \rho_w\mathbf{g}\right)\right)\right] - Q^h = 0 \tag{3.49}$$

At the ground surface an extra term is added due to a fixed air temperature T_a. This extra term has the form:

$$C_{as}\left(T - T_a\right) \tag{3.50}$$

In which C_{as} is a convective heat transfer coefficient for the ground surface.

3.4 Momentum conservation equation

The effective stress can be coupled to strain in the following way:

$$d\sigma' = \mathbf{M}\left(d\varepsilon - d\varepsilon_T\right) \tag{3.51}$$

Where $d\varepsilon$ is the total strain differential, $d\varepsilon_T$ is the thermal strain differential and M is the material stress-strain matrix describing the constitutive model. The negative dependence on the thermal strain differential is intuitively clear. When the temperature of a material is increased it has the tendency to change in volume. If the material is confined but a temperature change results in an expansive thermal strain, it has to be balanced by a mechanical strain with the same magnitude but with opposite sign in order to have a total strain of zero (i.e. confinement). The minus sign in front of the thermal strain in this case means that an expansive thermal strain results in a compressive stress since the volume cannot increase. The equation describing the conservation of momentum is given by equation (2.27). Inserting (3.51) into this equation gives:

$$\nabla\cdot\left(\mathbf{M}\left(d\varepsilon - d\varepsilon_T\right) + \left(d\chi p_w + \chi dp_w + \left(1-\chi\right)dp_g - d\chi p_g\right)\mathbf{I}\right) + d(\rho_m\mathbf{g}) = 0 \tag{3.52}$$

In PLAXIS the stress and strain matrices are implemented as column vectors that store their six independent components.

$$\sigma = \left(\sigma_{xx}, \sigma_{yy}, \sigma_{zz}, \sigma_{xy}, \sigma_{yz}, \sigma_{xz}\right)^T \tag{3.53}$$

And column vector $\mathbf{m}$ replaces the identity matrix $\mathbf{I}$.

$$\mathbf{m} = \left(1,1,1,0,0,0\right)^T \tag{3.54}$$

The following expression is used for the thermal strain differential.

$$d\varepsilon_T = \mathbf{B}_{DT}\mathbf{m}dT = \begin{pmatrix} \beta_{DT,x} & 0 & 0 & 0 & 0 & 0 \\ 0 & \beta_{DT,y} & 0 & 0 & 0 & 0 \\ 0 & 0 & \beta_{DT,z} & 0 & 0 & 0 \\ 0 & 0 & 0 & 0 & 0 & 0 \\ 0 & 0 & 0 & 0 & 0 & 0 \\ 0 & 0 & 0 & 0 & 0 & 0 \end{pmatrix}\begin{pmatrix} 1 \\ 1 \\ 1 \\ 0 \\ 0 \\ 0 \end{pmatrix} dT \tag{3.55}$$

The volumetric thermal expansion coefficient of the solid grains can be expressed as a function of the skeletal thermal expansion coefficients [20].

$$\beta_{sT} = \beta_{DT,x} + \beta_{DT,y} + \beta_{DT,z} \tag{3.56}$$

In PLAXIS the assumption is made that the relative air tension is always zero. Also, the term with $d\chi$ is neglected and gravity is assumed to be constant. Under these assumptions (3.52) reduces to the following expression for the momentum balance equation:

$$\nabla\cdot\left[\mathbf{M}\left(d\varepsilon - \mathbf{B}_{DT}\mathbf{m}dT\right) + \chi dp_w\mathbf{m}\right] + d\rho_m\mathbf{g} = 0 \tag{3.57}$$

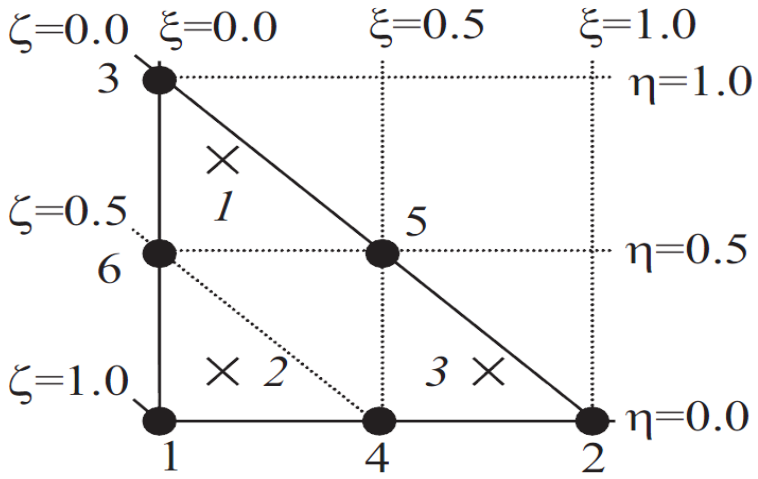

Figure 3.1: Local coordinate system in which the interpolation functions are expressed. The black dots represent nodes and the crosses represent Gaussian integration points. Figure from [35].

3.5 Interpolation functions and integration rules in PLAXIS

The weak form of the energy, momentum and water mass balance equations can be derived according to the methods presented in section 2.5. These can be used in a relatively straight-forward way to derive the Galerkin formulation. The volume integrals that appear in the Galerkin formulation can be reduced to surface integrals in PLAXIS 2D due to plane conditions. These surface integrals can be computed as a sum of the surface integrals over each of the elements. And the surface integral over a specific element can be computed in a local coordinate system (ξ, η). The local and the global coordinate systems are related through the Jacobian matrix:

$$\begin{pmatrix} \frac{\partial \phi_i}{\partial x} \\ \frac{\partial \phi_i}{\partial y} \end{pmatrix} = \begin{pmatrix} \frac{\partial \xi}{\partial x} & \frac{\partial \eta}{\partial x} \\ \frac{\partial \xi}{\partial y} & \frac{\partial \eta}{\partial y} \end{pmatrix} \begin{pmatrix} \frac{\partial \phi_i}{\partial \xi} \\ \frac{\partial \phi_i}{\partial \eta} \end{pmatrix} \tag{3.58}$$

In order to have a one to one mapping the Jacobian matrix should not be singular. An auxiliary coordinate is used for convenience.

$$\zeta = 1 - \xi - \eta \tag{3.59}$$

Within this local coordinate system the shape functions are then defined as follows for a triangular element with 6 nodes: [35].

$$\phi_1 = \zeta\,(2\zeta - 1) \tag{3.60}$$
$$\phi_2 = \xi\,(2\xi - 1) \tag{3.61}$$
$$\phi_3 = \eta\,(2\eta - 1) \tag{3.62}$$
$$\phi_4 = 4\zeta\xi \tag{3.63}$$
$$\phi_5 = 4\xi\eta \tag{3.64}$$
$$\phi_6 = 4\eta\zeta \tag{3.65}$$
$$\tag{3.66}$$

For a visual representation, see figure 3.1. Note that each interpolation function ϕ_i is zero on all nodes except for node i. Numerical calculation of integrals that appear in the Galerkin formulation can be done with a technique called Gaussian integration. For the 6-noded element presented in figure 3.1 three integration points are used in PLAXIS. No values are stored at these integration points, but with the use of the interpolation functions an estimate can be obtained. See equation (2.61) for instance. The integral is then approximated in the following way for a 6-noded element in PLAXIS:

$$\int_S F(\xi,\eta)d\xi d\eta \approx \sum_{i=1}^{3} F(\xi_i,\eta_i)w_i \tag{3.67}$$

In which the weights w_i are given in table 3.3.

Table 3.3: Location and weights of the Gaussian integration points used for a 6-noded element in PLAXIS. [35]

Point	ξ_i	η_i	w_i
1	1/6	2/3	1/3
2	1/6	1/6	1/3
3	2/3	1/6	1/3

3.6 Solution scheme

The Galerkin formulation will give rise to a set of matrix-vector multiplications with a form similar to (2.67). The vector T will contain nodal values of the pressure, displacement and temperature. The vector $\dot{T}$ contains the time derivatives of these quantities. In addition to the RHS-vector $\mathbf{F}$, matrix $\mathbf{M}$ and $\mathbf{S}$ are not constant either but depend on temperature, pressure and displacement. This set of equations is therefore non-linear. A fully implicit method (i.e. $\theta = 1$ in equation (2.72)) is used for timestepping. In order to solve the resulting non-linear set of equations the Newton-Raphson method will be used. This method is described in section 2.6. In PLAXIS the stiffness matrix $\mathbf{K}$ is estimated only during the first iteration of each timestep and is then held constant. During each non-linear iteration a set of linear equations like (2.78) has to be solved. This is done by using Intel's PARDISO solver which is based on the LU decomposition principle explained in section 2.7.

Chapter 4

Verification of model implementation

4.1 1D nonporous verification

In Appendix A a set of equations has been derived describing the temperature and strain evolution in a homogeneous nonporous column of material. The geometry of the model is displayed in figure 4.1. Standard fixities are applied which means that the displacement are fixed in both directions at the bottom and horizontal displacement are fixed at the sides while vertical displacements are allowed. No movement restrictions are applied to the top of the column. The temperature at the bottom is fixed at a constant T_0 and a constant heat flux Q_0 is applied at the top. At time $t = 0$ the column has a uniform temperature T_0. More information about the geometry, parameters and boundary conditions can be found in table 4.2. The temperature evolution is described with the following equation (A.31):

$$T(y,t) = \frac{8Q}{\lambda\pi^2}\sum_{i=0}^{\infty}\frac{(-1)^i}{(2i+1)^2}\sin\left(\left(i+\frac{1}{2}\right)\pi y\right)e^{-\frac{\pi^2\lambda t(1+i)^2}{C_s\rho_s}} - \frac{Q}{\lambda}y + T_0 \tag{4.1}$$

And ε_{yy} is described by (A.35):

$$\varepsilon_{yy} = (T - T_0)\left(\beta_{DT,Y} + \frac{\nu}{1-\nu}\left(\beta_{DT,X} + \beta_{DT,Z}\right)\right) \tag{4.2}$$

During the first step of the verification the temperature is plotted against time for a fixed point. The THM implementation calculates temperatures at stress points. The point $y = 0.997m$ has been chosen since it is the stress point closest to the top boundary where a fixed heat flow will cause the temperature to rise quickly. The verification of the THM-implementation has been performed for different time-steps. The results are displayed in figure 4.2. The steady state end temperature which is achieved by the analytical solution and the THM-implementation are the same, independent of the time step used. Although it can be seen that the accuracy of the solution obtained in PLAXIS depends on the length of the time step. When the time step size is reduced the results produced by the THM-implementation grow towards the analytical solution. In this case a time step of 4000 seconds produces such a good fit to the analytical solution that they perfectly overlap in figure 4.2. The figure demonstrates the importance of having an appropriate time step in obtaining a correct solution.

For the next step in the verification procedure a comparison is done between the analytical result and model prediction for the temperature in a cross-section at $t = 100000$ *sec*. Because this end time is much lower than that in figure 4.2 a smaller timestep of 1000 *sec* was affordable. Figure 4.3 demonstrates that the analytical results match those of the THM implementation very well.

Finally a comparison of the analytical strains in the y direction and the those calculated by the THM-model has been done. ϵ_{yy} now plotted against position y along the same cross section of figure 4.3. The results are plotted in figure 4.4. A good correspondence is obtained again.

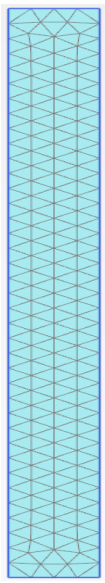

Figure 4.1: Geometry of the homogeneous nonporous column of material.

Table 4.1: The geometry used in PLAXIS for the 'one-dimensional time-dependent heat conduction in a nonporous medium' verification

Shape	rectangular
Width	0.1m
Height	1m
Coarseness	medium
Elements	304
Element type	15 node
Fixities	standard

Table 4.2: Parameters used for the 'one-dimensional time-dependent heat conduction in a nonporous medium' verification. The parameters represent a certain type of steel.

y_{bot}	0.0	m
y_{top}	1.0	m
T_0	273.15	K
Q	-773.15	$W\ m^{-2}$
λ	14.6	$W\ m^{-1}K^{-1}$
C_s	460	$J\ kg^{-1}K^{-1}$
ρ_s	7800	$kg\ m^{-3}$
ν	0.30	-
E	$2 * 10^5$	Pa
$\beta_{DT,X}$	$1 * 10^{-5}$	K^{-1}
$\beta_{DT,Y}$	$1 * 10^{-5}$	K^{-1}
$\beta_{DT,Z}$	$1 * 10^{-5}$	K^{-1}

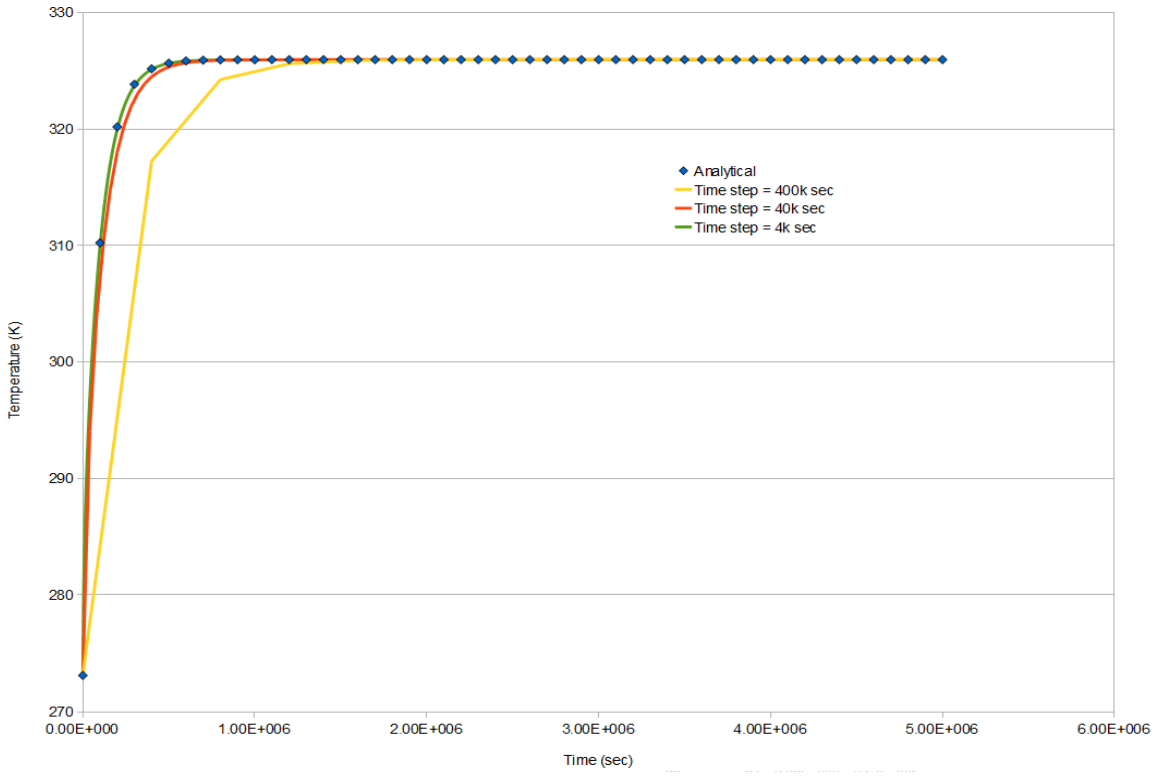

Figure 4.2: Temperature vs time at $y = 0.997$ for different timesteps. Linear interpolation is performed between the data points for visualisation purposes. The analytical solution is plotted for reference.

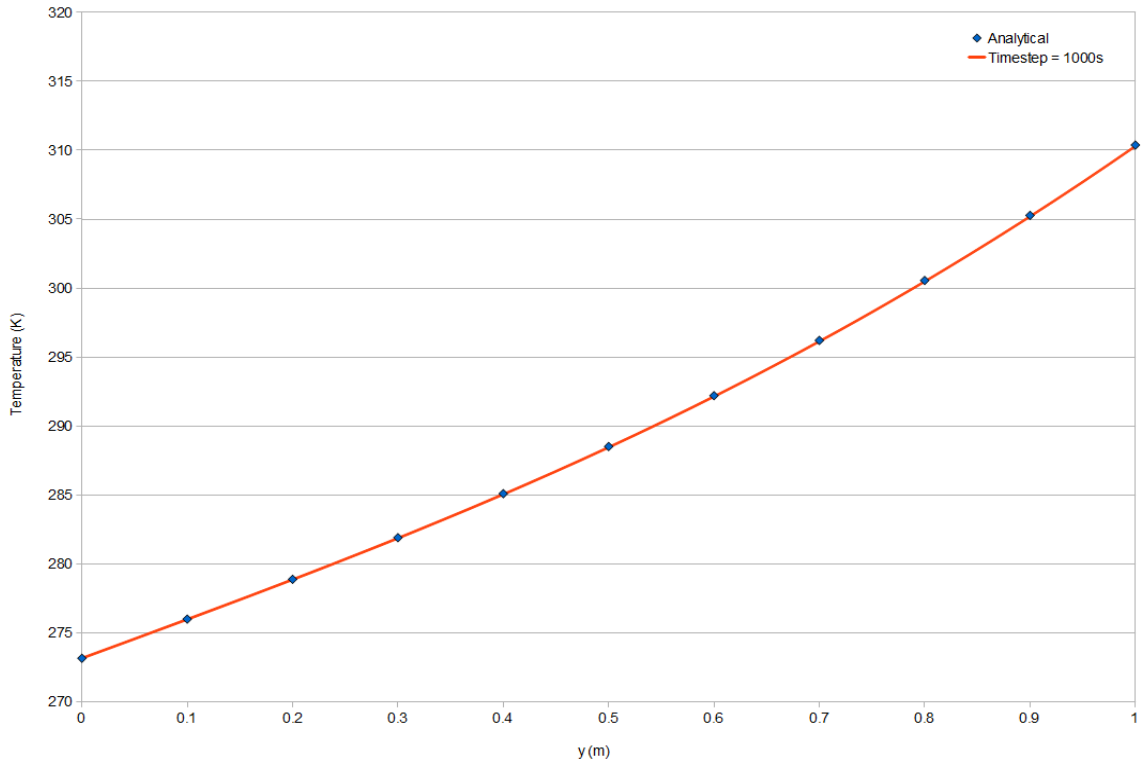

Figure 4.3: Temperature vs position y at $t = 100000$ *sec*. The analytical solution is plotted for reference.

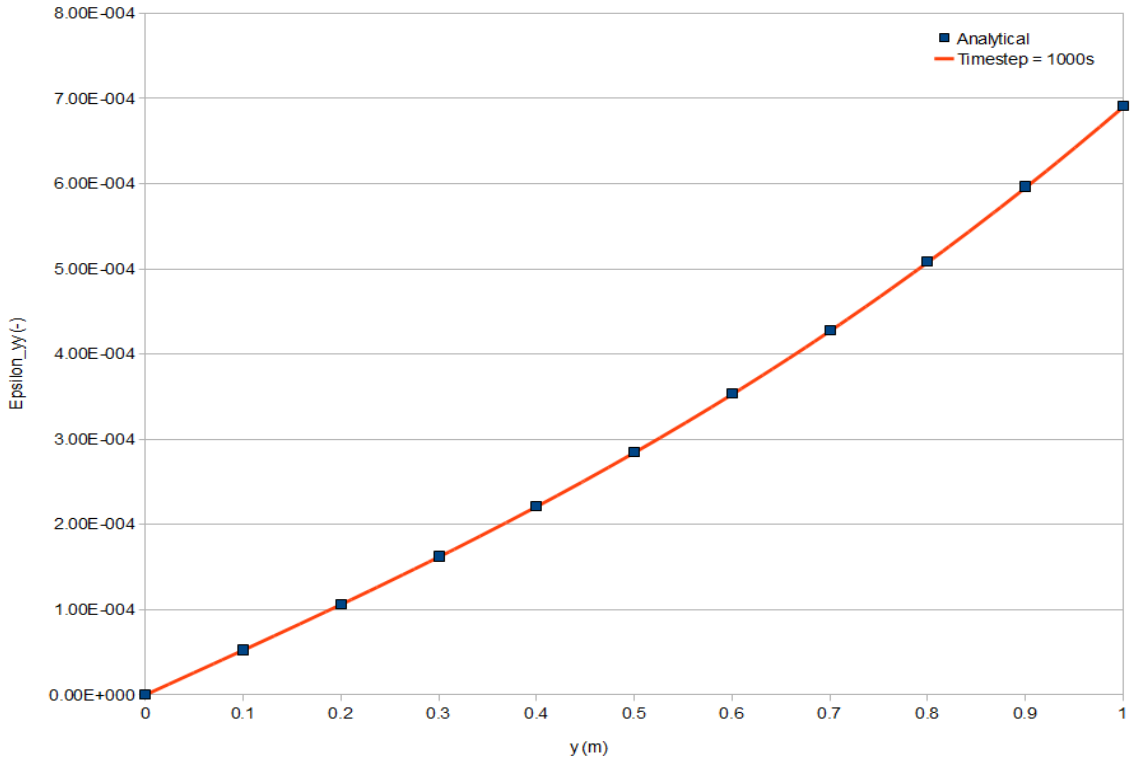

Figure 4.4: Strain in direction y vs position y at $t = 100000$ *sec*. The analytical solution is plotted for reference.

4.2 Vapor diffusion

In this section the correct numerical implementation of the vapor flux is investigated in PLAXIS. Special attention is given to the effect of having a variable vapor diffusion coefficient as expressed by equation (3.7). A uniform temperature will be used to isolate the effect of the suction. The PLAXIS geometry and the (artificial) soil used in the investigations are specified in table 4.3. Figure 4.5 shows the geometry. The thermal parameters are not included in table 4.3, since the initial temperature and the fixed temperature at the top and bottom boundaries are the same. The temperature will therefore be uniform since no heat generation is present in the current model. Viscous dissipation is currently not implemented in PLAXIS as mentioned in section 3.3.

In the current THM-development implementation the water flow through a seepage boundary is zero. In other words: the sum of the liquid water mass- and vapor mass fluxes is zero. This means that the current development implementation basically models the soil's response when an impermeable layer (e.g. a geomembrane) covers the ground surface. One way of interpreting this is that all the water vapor that leaves the soil column at the top condensates and immediately re-enters as liquid water, satisfying the imposed zero net flux.

The program 'PLAXIS Output' currently only produces output for the liquid tension. When using this information and the equations specified in section 3.1, all the unknowns related to the vapor flux can be calculated. These calculated values are then compared with the output of a modified PLAXIS THM-kernel. This modified kernel writes all unknowns related to the vapor flux to unformatted output files, allowing for a comparison with the unknowns calculated from the water tension profiles. If a good match is obtained the correct code implementation of the vapor flux equations has been verified.

First of all a vertical cross-section is made in PLAXIS Output, extending from the bottom to the top. A set of points describing the liquid tension along this curve is then obtained. When no vapor diffusion takes place the pore water pressure profile is hydrostatic as shown in figure 4.5. A deviation from the hydrostatic pressure profile is present when a vapor flux takes place. This effect is demonstrated in figure 4.6a. The largest pore water tension deviation is produced by the constant vapor diffusion coefficient case. This is not surprising since the constant vapor diffusion coefficient D_{v0} is always larger than the variable vapor diffusion coefficient D_v, see equation (3.7). The constant vapor diffusion coefficient deviates the most from the hydrostatic case in which no vapor diffusion takes place (i.e. D_{v0} is zero).

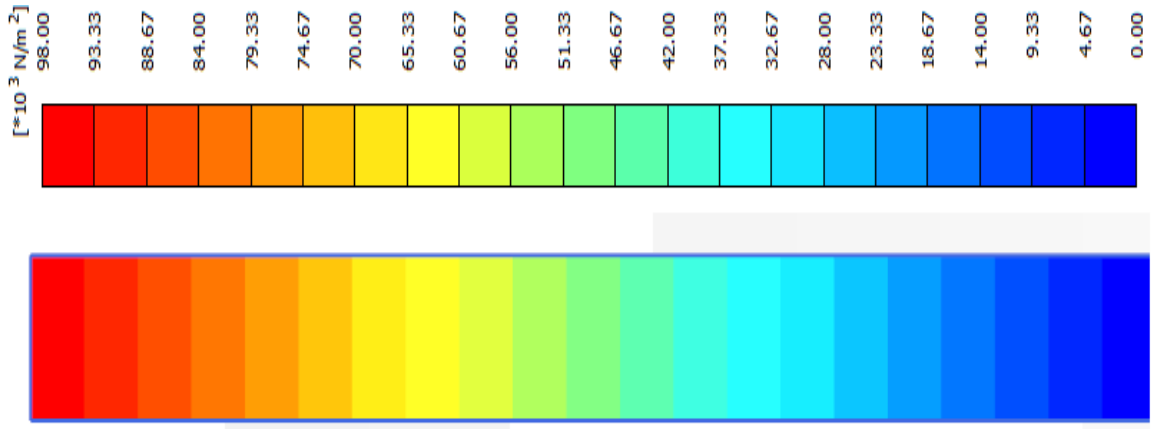

Figure 4.5: PLAXIS model used for the vapor diffusion investigations. The model is rotated 90 degrees to the left in this figure. The bottom of the soil column corresponds to the right side of the rotated figure. Since the phreatic surface is set to the bottom of the soil column, the suction p_w is zero here. The hydrostatic gradient presented in this figure is the steady state solution for the unsaturated column when no vapor diffusion takes place.

Table 4.3: Model parameters used in the first vapor diffusion investigation

Model parameter	Value
Shape	rectangular
Width	1.0m
Height	10.0m
y_{bot}	0.0m
y_{top}	10.0m
Coarseness	fine
Elements	540
Element type	15 node
Fixities	standard
Top hydraulic boundary condition	Seepage (default)
Sides hydraulic boundary condition	closed
Bottom hydraulic boundary condition	Fixed head (0.0m)
t_{final}	$1.0 * 10^9$d (to ensure steady state)

Material parameter	Value
def. model	elastic
ret. model	Van Genuchten
subsoil/topsoil	subsoil
ρ_s	2800 $(kg\ m^{-3})$
ρ_w	1000 $(kg\ m^{-3})$
ν	0.20 (-)
E	$1 * 10^7$ (Pa)
D_{v0}	$1 * 10^{-5}$ $(m^2 s^{-1})$
k	$1.760 * 10^{-6}$ (m/s)
ψ_{unsat}	$1 * 10^4$ m
e_{init}	0.5 $(-)$
T	293.15 (K)

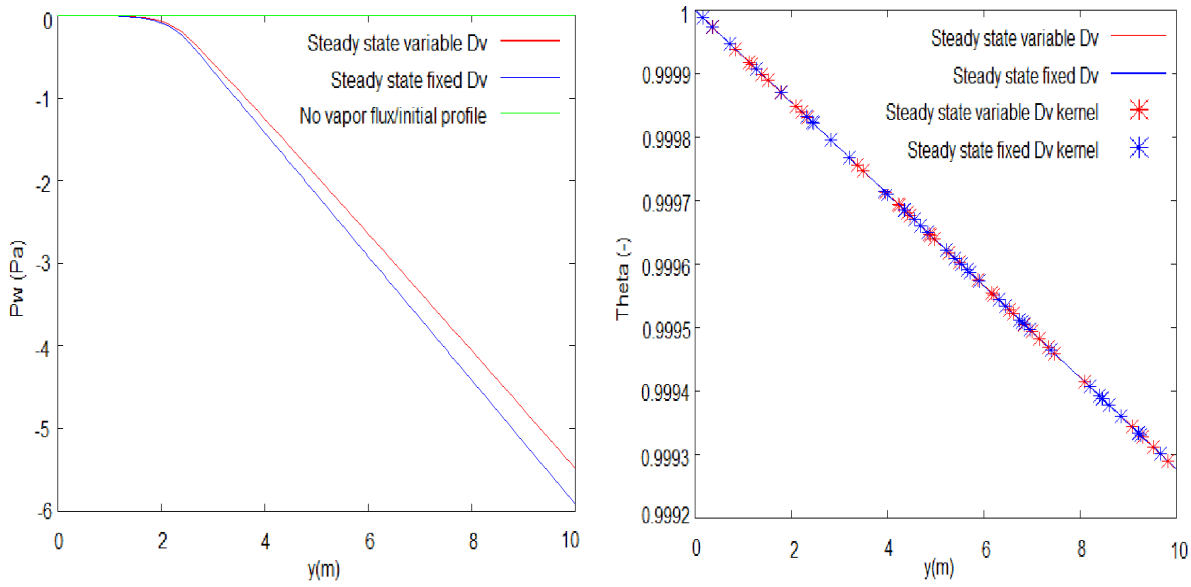

(a) **(b)**

Figure 4.6: a) Water tension relative to the hydrostatic case. When vapor transport is modeled the suction is reduced. b) Relative humidity. The solid lines are calculated from the pressure profile produced by PLAXIS Output. The crosses are values written to file by the modified PLAXIS kernel.

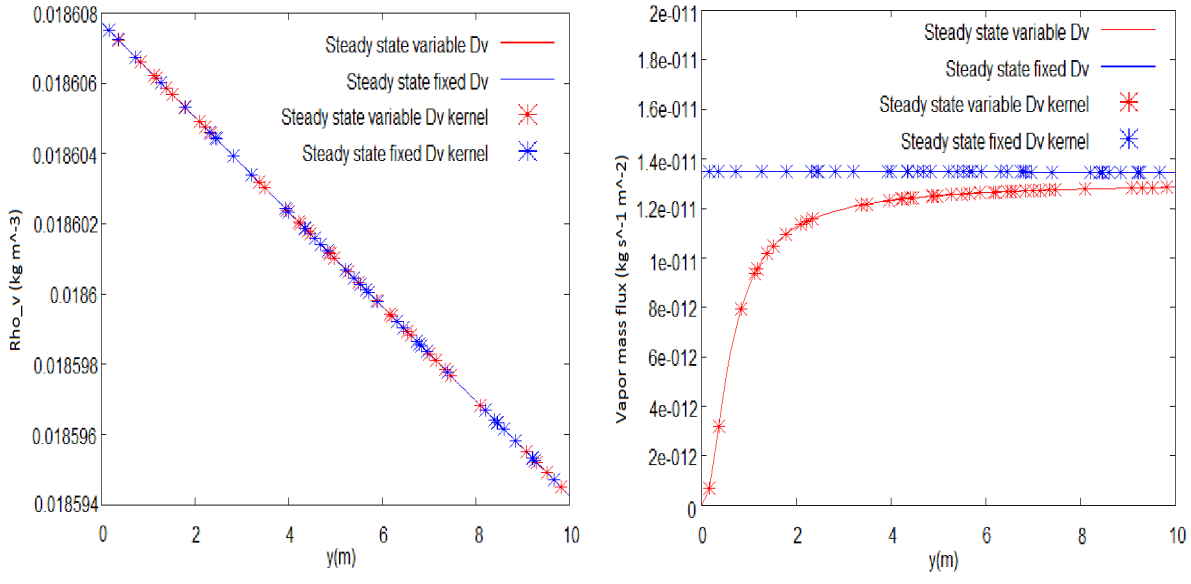

(a) **(b)**

Figure 4.7: The solid lines are calculated from the pressure profile produced by PLAXIS Output. The crosses are values written to file by the modified PLAXIS kernel. a) Vapor density. b) Vapor flux.

Nevertheless, the largest tensional deviation occurs at the top of the column and is only 6 Pa. This is very small compared to the hydrostatic reference tension of 98000 Pa at this elevation.

In figure 4.6b the relative humidity is plotted. Equation (3.10) is applied to the pressure profile obtained from PLAXIS Output. The results are represented by the solid line. The values written directly from the calculation kernel are indicated by crosses. It can be seen that the calculated and the written values agree perfectly. This verifies the correct implementation of the relative humidity equation (3.10). In this investigation, having a constant or variable vapor diffusion coefficient has a negligible effect on the relative humidity. The reason for this is that their respective water tension profiles are almost the same.

The calculated relative humidity values are then inserted into equations (3.11) and (3.23). The resulting vapor density profile is represented by a solid line in figure 4.7a. These calculated values are again compared with the values written from the calculation kernel. Because a perfect match is obtained the conclusion is drawn that the numerical implementation of the vapor density equation is correct.

The kernel of PLAXIS calculates the vapor flux by using equation (3.20). D_{pv} is calculated by using the approximation (3.21). The correct numerical implementation of these equations can be verified by using the water tension profile obtained from PLAXIS Output in combination with the previously calculated vapor density profile. In order to calculate the vapor mass flux according to equation (3.20), the water tension gradient must be determined. In this one-dimensional geometry this reduces to the derivative of the water tension in the y-direction. Even though the lines in figures 4.6a,b and 4.7a are solid, they are formed by interpolating between the finite set of values obtained from PLAXIS Output. The derivative of the water tension in the y-direction therefore has to be determined by using a finite difference approximation scheme. Equations for variable grid spacing have been derived using a form similar to the uniform grid spacing equations as defined in [10]. Taylor expansions are summed to obtain an expression for the derivative. For points at the top and bottom a forward and backward derivative with the same order of precision is used respectively.

$$F'(y_i) = \frac{-F(y_{i+2}) + 4F(y_{i+1}) - 3F(y_i)}{3\Delta y_i - \Delta y_{i+1}} \tag{4.3}$$

$$F'(y_i) = \frac{F(y_{i-2}) - 4F(y_{i-1}) + 3F(y_i)}{3\Delta y_{i-1} - \Delta y_{i-2}} \tag{4.4}$$

Δy_i is the spacing between point i and $i+1$. If the spacing of the points would have been a constant Δy, then these approximations would have second order accuracy. A central difference scheme is used for the interior points since in the case of uniform spacing it approximates derivatives with second order accuracy.

$$F'(y_i) = \frac{F(y_{i+1}) - F(y_{i-1})}{\Delta y_{i-1} + \Delta y_i} \tag{4.5}$$

Figure 4.7b shows that a very good match is obtained between the calculated vapor mass flux and the vapor mass flux directly written to output files by the modified PLAXIS kernel. This verifies that the numerical implementation of the water tension part of equation (3.20) is correct.

The vapor mass flux could instead have been calculated by using equation (3.6). This way the effect of the approximation (3.21) can be investigated. The gradient of the vapor density can be obtained by using the results from figure 4.7a in combination with the finite difference approximation scheme. The vapor flux which is obtained in this way can be compared with the values written by the kernel, which are still based on equation (3.20). The resulting figure will be indistinguishable from figure 4.7b. This verifies that the effect of approximation (3.21) is negligible in this case.

Close to the phreatic surface the vapor mass flux is influenced significantly by whether or not a variable vapor diffusion coefficient is used. This is not surprising since the saturation is very close to one in this region. Most of the pore space is filled with liquid water, reducing the magnitude of the vapor mass flux when a variable vapor diffusion coefficient is used. Since a steady state is obtained and the model is one-dimensional, the water mass balance equation (3.32) reduces to:

$$\frac{\partial}{\partial y}\left(\mathbf{J}_w + \mathbf{J}_v\right) = 0 \tag{4.6}$$

Or in other words, the sum of the liquid and the vapor mass flux of water is constant. Earlier in this section it was discussed that the sum of these fluxes at the top of the column is equal to zero. With this boundary condition, equation (4.6) means that the sum of the liquid and the vapor mass fluxes is zero in the entire column at steady state. The calculated vapor mass flux profile has been compared with

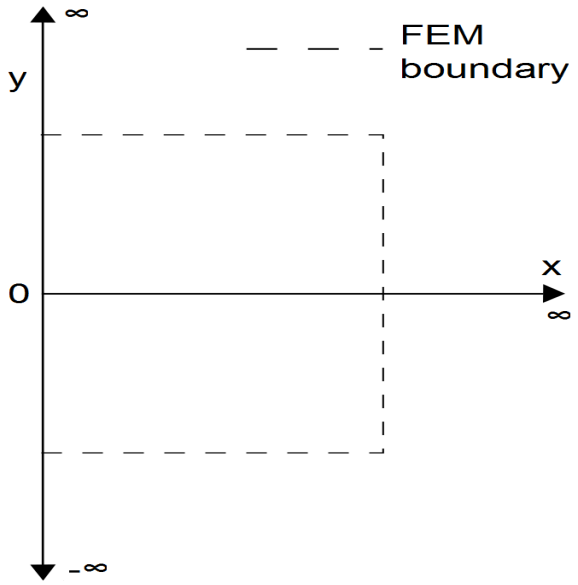

Figure 4.8: The analytical solution requires the use of a semi-infinite half-plane. Since infinity can not be represented in PLAXIS, the boundaries of the model have to be finite. It is therefore necessary to ensure that the temperature disturbance is not influenced by these boundaries during the modeling procedure.

the liquid water mass flux profile obtained from PLAXIS Output, and they are exactly opposite so that their sum is zero.

Remark: In the current implementation, the total water mass flux through the seepage boundary at the top of the model is zero. This is equivalent to modeling the response of a soil covered by a geomembrane. Another alternative would be to prescribe the relative humidity at an air-soil boundary. With such a boundary condition drying of a soil can be modeled. Instead of a suction reduction displayed in figure 4.6a, the suction would increase in the entire column by prescribing $\theta < 0.99$ at the air-soil interface.

4.3 2D Temperature advection-diffusion

4.3.1 Analytical solution

In this section an analytical solution is presented for one-dimensional advection and two-dimensional diffusion of heat. The aim of these equations is to verify the proper implementation of the energy balance equation. In order to do this it is important to minimize the effects of the water mass balance and momentum balance equations. The PLAXIS implementation of these equations are restated here for convenience:

$$\phi \frac{\partial}{\partial t}\left(S\rho_l^w + (1-S)\,\rho_g^w\right) + \left(S\rho_l^w + (1-S)\,\rho_g^w\right)\left[\frac{\partial \varepsilon_V}{\partial t} + \frac{(1-\phi)}{\rho_s}\frac{\partial \rho_s}{\partial t}\right] = -\nabla\cdot\left(\mathbf{J}_l^w + \mathbf{J}_g^w\right) \tag{4.7}$$

$$\nabla\cdot\left(\mathbf{M}\left(d\varepsilon - d\varepsilon_T\right) + \chi p_w \mathbf{I}\right) + \rho_m \mathbf{g} = 0 \tag{4.8}$$

The analytical solution to the one-dimensional advection and two-dimensional diffusion of temperature presented in this section is based on the assumption of a constant horizontal water velocity. The derivation will use the assumption of a semi-infinite half-plane, see figure 4.8. Since infinite distances can not be dealt with in PLAXIS it is important to verify that the temperature evolution is not influenced by the (finite) boundaries when running the model. At a certain point in time the temperature solution will become influenced by the finite boundaries and the analytical and numerical results are expected to diverge. A water velocity field cannot be directly imposed in PLAXIS since it depends on the unknown P_w through the equation for $\mathbf{J}_l^w$. However, by selecting a proper set of parameters and boundary conditions such a velocity field can be approximated. By looking at the water mass balance it is easy to see that using a

fully saturated scenario already leads to a large reduction of terms.

$$\phi \frac{\partial \rho_l^w}{\partial t} + \rho_l^w \left[\frac{\partial \varepsilon_V}{\partial t} + \frac{(1-\phi)}{\rho_s} \frac{\partial \rho_s}{\partial t} \right] = -\nabla \cdot (\mathbf{J}_l^w) \tag{4.9}$$

Constant water density can be enforced by setting the compressibility and thermal expansion coefficient of water to zero. Constant solid density can also be enforced by setting its thermal expansion coefficient to zero. Finally, the volumetric strain rate will approach zero when the bulk modulus is made sufficiently large. The result of using these parameters is that the divergence of the water flux in equation (4.9) is approximately zero. This means that the amount of water leaving a reference volume is the same as the amount that enters. By setting zero influx of water at the top and the bottom and a fixed horizontal velocity on the left, a constant horizontal velocity field is a solution. When using a constant intrinsic permeability and viscosity this will translate into a uniform horizontal pressure gradient.

A set of equations will now be presented for the advection-diffusion equation on a half-plane with constant horizontal water velocity. When using constant water density, heat capacity and horizontal water velocity the energy balance equation (3.49) implemented in PLAXIS can be rewritten as:

$$\frac{\partial T}{\partial t} = D \left(\frac{\partial^2 T}{\partial x^2} + \frac{\partial^2 T}{\partial y^2} \right) - E \frac{\partial T}{\partial x} \tag{4.10}$$

In which:

$$D = \frac{\lambda}{C\rho} \tag{4.11}$$

$$E = \frac{\rho_w C_w V_x}{C\rho} \tag{4.12}$$

Equation (4.10) expresses the energy balance in a convenient advection-diffusion form. The temperature solution will propagate with effective velocity E (4.12). At the same time the heat diffusivity D (4.11) will smoothen any discontinuities that might be present. The following boundary conditions will be used.

$$T(x,y,0) = T_0 \qquad 0 < x < \infty \qquad -\infty < y < \infty \tag{4.13}$$

$$T(0,y,t) = T_L \qquad y < 0 \qquad t > 0 \tag{4.14}$$

$$T(0,y,t) = \frac{1}{2}(T_L + T_R) \qquad y = 0 \qquad t > 0 \tag{4.15}$$

$$T(0,y,t) = T_R \qquad y > 0 \qquad t > 0 \tag{4.16}$$

$$\left.\frac{\partial T}{\partial x}\right|_{x \to \infty} = 0 \qquad -\infty < y < \infty \qquad t > 0 \tag{4.17}$$

$$\left.\frac{\partial T}{\partial y}\right|_{x \to \pm\infty} = 0 \qquad 0 < x < \infty \qquad t > 0 \tag{4.18}$$

$$\tag{4.19}$$

The analytical solution to equation (4.10) with these given boundary conditions is presented by F.J. Leij and J.H. Dane [22]:

$$T(x,y,t) = \frac{x}{\sqrt{4\pi D}} \int_0^t \tau^{-3/2} \left\{ \frac{T_L}{2} \operatorname{erfc}\left[\frac{y}{\sqrt{4D\tau}} \right] + \frac{T_R}{2} \operatorname{erfc}\left[-\frac{y}{\sqrt{4D\tau}} \right] \right\} \exp\left[-\left(\frac{x - Et}{\sqrt{4D\tau}} \right)^2 \right] d\tau$$
$$- \frac{T_0}{2} \left\{ \operatorname{erfc}\left[\frac{x - Et}{\sqrt{4Dt}} \right] + \exp\left(\frac{Ex}{D} \right) \operatorname{erfc}\left[\frac{x + Et}{\sqrt{4Dt}} \right] \right\} + T_0 \tag{4.20}$$

$$\tag{4.21}$$

In which τ is a dummy variable and erfc() is the complementary error function:

$$\operatorname{erfc}(x) = 1 - \operatorname{erf}(x) = 1 - \frac{2}{\sqrt{\pi}} \int_0^x \exp^{-\tau^2} d\tau = \frac{2}{\sqrt{\pi}} \int_x^\infty \exp^{-\tau^2} d\tau \tag{4.22}$$

The use of Laplace and Fourier transforms is central to the derivation of (4.20). An alternative solution has been derived by Bruch and Street [22]. This solution has the desirable property that the domain

is only infinite in the x-direction while being bounded between 0 and n_0 in the y-direction. Under the following assumptions:

$$T(x,y,0) = 0 \qquad x > 0 \qquad 0 < y < n_0 \tag{4.23}$$
$$T(0,y,t) = T_i \qquad 0 < y < \varepsilon \qquad t > 0 \tag{4.24}$$
$$T(0,y,t) = 0 \qquad \varepsilon < y < n_0 \qquad t > 0 \tag{4.25}$$
$$T(\infty,y,t) = \text{bounded} \qquad 0 < y < n_0 \qquad t > 0 \tag{4.26}$$
$$\left.\frac{\partial T}{\partial y}\right|_{y=0} = 0 \qquad x > 0 \qquad t > 0 \tag{4.27}$$
$$\left.\frac{\partial T}{\partial y}\right|_{y=n_0} = 0 \qquad x > 0 \qquad t > 0 \tag{4.28}$$
$$\tag{4.29}$$

The following solution to equation (4.10) can then be derived.

$$C(x,y,t) = \frac{\varepsilon T_i}{2n_0}\left\{\text{erfc}\left[\frac{x-Et}{\sqrt{4Dt}}\right] + \exp\left(\frac{Ex}{D}\right)\text{erfc}\left[\frac{x+Et}{\sqrt{4Dt}}\right]\right\} + \sum_{n=1}^{\infty}\left\{\frac{T_i}{n\pi}\sin\left(\frac{n\pi\varepsilon}{n_0}\right)\cos\left(\frac{n\pi y}{n_0}\right)\right.$$
$$\cdot\left[\exp\left(\frac{x}{2}\left[\frac{E}{D} - \sqrt{\left(\frac{E}{D}\right)^2 + \left(\frac{2n\pi}{n_0}\right)^2}\right]\right)\cdot\text{erfc}\left(\frac{x - Dt\sqrt{\left[\frac{E}{D}\right]^2 + \left[\frac{2n\pi}{n_0}\right]^2}}{\sqrt{4Dt}}\right)\right.$$
$$\left.\left. + \exp\left(\frac{x}{2}\left[\frac{E}{D} + \sqrt{\left(\frac{E}{D}\right)^2 + \left(\frac{2n\pi}{n_0}\right)^2}\right]\right)\cdot\text{erfc}\left(\frac{x + Dt\sqrt{\left[\frac{E}{D}\right]^2 + \left[\frac{2n\pi}{n_0}\right]^2}}{\sqrt{4Dt}}\right)\right]\right\} \tag{4.30}$$
$$\tag{4.31}$$

Both approaches can be used to verify the proper code implementation of the energy balance equation. With equation (4.20) an initial uniform temperature T_0 can be selected while equation (4.30) uses $T_0 = 0$. Since temperature is measured in degrees Kelvin in PLAXIS this would mean that the soil temperature is initially at absolute zero. Even though this does not represent a physically acceptable situation the analytical equation can still be used to verify the proper code implementation of the energy balance equation. An advantage of equation (4.30) is that the y-direction is bounded with zero heat flux. The analytical boundary conditions for equation (4.30) only assume that the x-boundary is infinite in contrary to equation (4.20) which assumes that both the x- and the y-directions are infinite. Therefore only the x-boundary in PLAXIS has to be investigated to make sure that its effect on the solution is negligible. There will always be some small disturbance though since the thermal diffusion equation is parabolic. Analytically, the temperature at a point x_0 at t_0 will influence any other point x_1 at arbitrary t_1. This will not occur in the finite element implementation since the temperature gradients are based on shape functions which are only non-zero on a limited domain. It may take several time-steps before a temperature disturbance may be 'felt' at another point.

The equations presented in this section have not been compared with the numerical results from PLAXIS yet due to the problem described in section 4.3.2. As soon as this problem is fixed the equations presented above can be used for verifying the proper implementation of the energy balance equation.

4.3.2 Complications with the advection-diffusion of temperature

The current development implementation still experiences a problem when there is an inflow of water through a boundary on which the conductive heat flux has been fixed. This problem is illustrated by figure 4.9. The sides of the displayed square have a length of 1 meter. The temperature on the left boundary is fixed to $273.15°K$ and the temperature on the right boundary is fixed to $313.15°K$. Zero conductive heat flux has been specified on the top and bottom boundaries. Water flows from the top to the bottom of the model with a velocity of 1 centimeter per day. The temperature at the inflow boundary decreases far below the lowest fixed boundary temperature of $273.15°K$. A similar problem occurs at the outflow boundary. Here the temperature rises far above the highest fixed boundary condition of $313.15°K$.

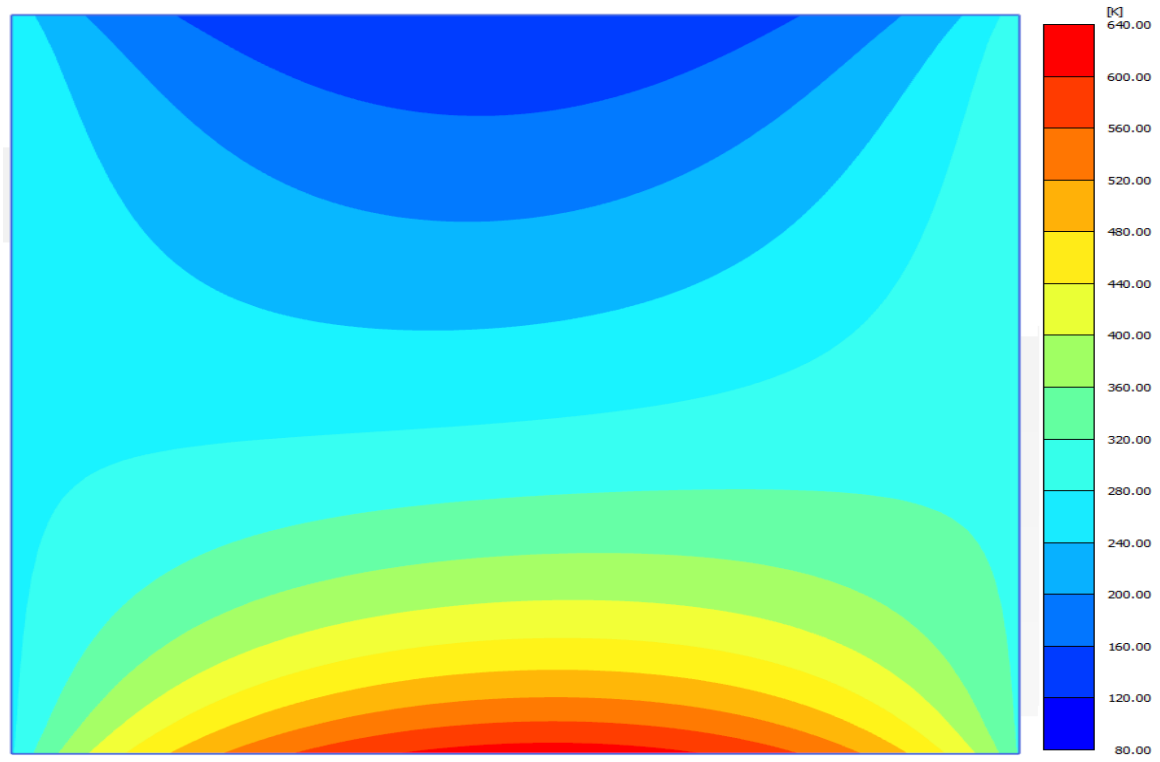

Figure 4.9: Temperature cross-section. The conductive heat flux at the top and bottom boundaries is set to zero. The flow of water through the top and bottom boundaries results in a temperature that falls outside the range of the fixed temperatures at the left and right boundaries.

The vertical conductive heat flux is plotted in figure 4.10. It becomes apparent that the boundary conditions of zero conductive heat flux are not met on the inflow and outflow boundaries. Instead, the conductive heat flux is exactly the opposite of the advective heat flux specified by equation (3.42). It turns out that the advective heat flux boundary integral is currently not correctly implemented in the finite element implementation. When this problem is fixed, the implementation of the advection-diffusion equation can be verified with the method described in section 4.3.1.

Remark: The numerical implementation of the advection-diffusion equation has notorious complications when it comes to boundary conditions. For instance, imagine a one-dimensional advection-diffusion model in which the water flows from the left to the right. A higher value of the advected quantity is imposed on the outflow boundary and the flow is advection-dominant. The red line in figure 4.11 shows the analytical steady state solution. The approximation made by a finite difference implementation of the advection-diffusion equation is given by the black dotted line. This solution displays non-physical oscillations in order to satisfy the prescribed boundary conditions.

The same oscillations will take place with a straight-forward finite element implementation of the advection diffusion equation when the flow is advection dominant [48]. These oscillations are the result of the inability of the mesh to represent the steep slopes of the analytical solution. Techniques such as upstreaming or (adaptive) mesh refinement may be used to deal with these problems, although they also have their limitations. It would be desirable not to impose any thermal boundary condition on the outflow boundary, but this would lead to an incomplete set of equations in the finite element method. Further research is required in order to correctly implement the temperature advection-diffusion equation in PLAXIS. The current THM-model is still in an early phase of development.

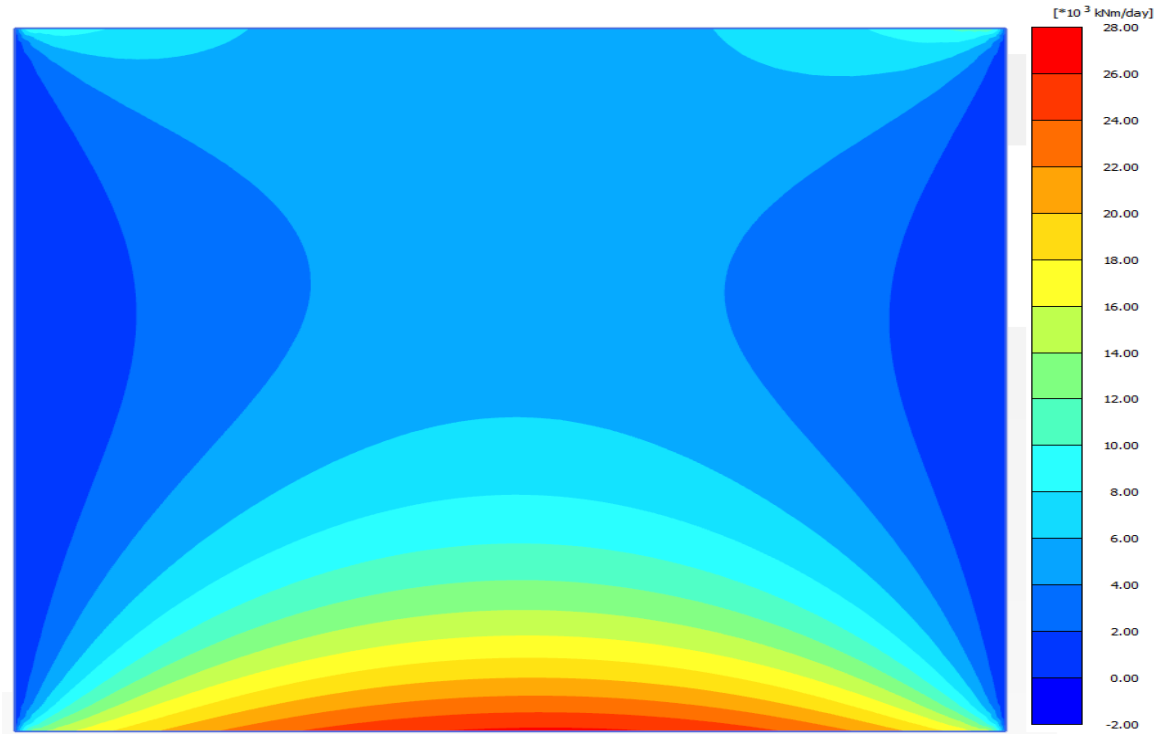

Figure 4.10: Cross-section of the vertical conductive heat flux. Zero conductive heat flux has been specified on the top and bottom boundaries. This figure shows that these boundary conditions are not met due to the inflow of water.

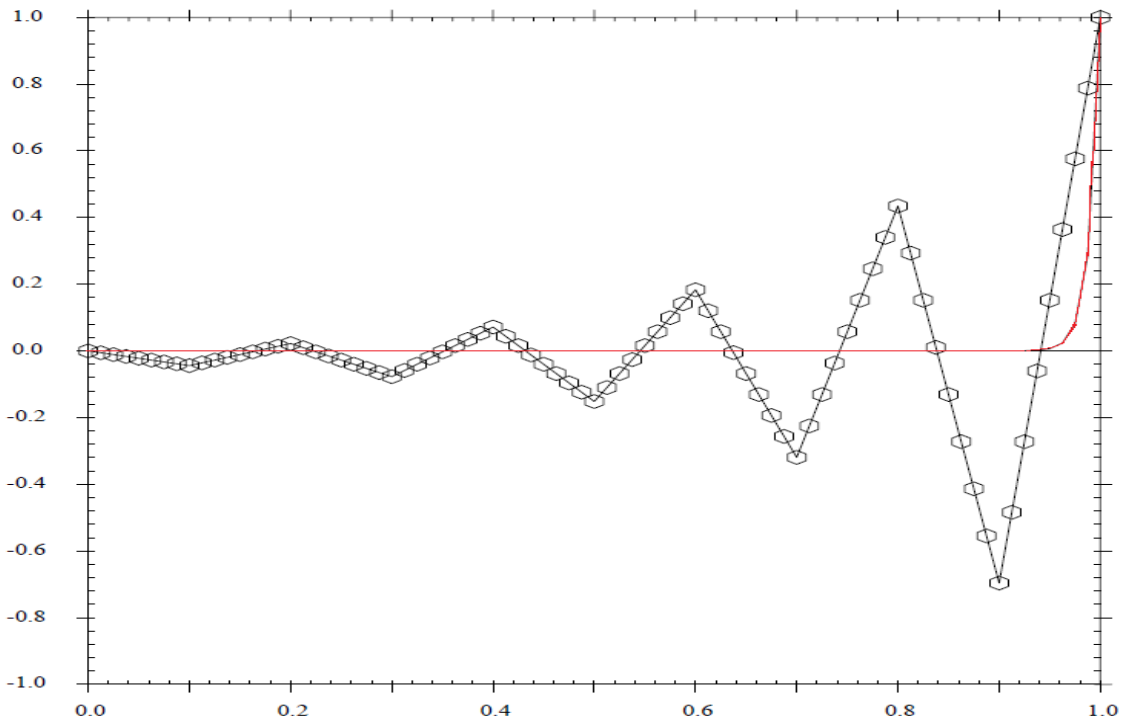

Figure 4.11: The horizontal axis represents the spatial coordinate and the vertical axis represents the advected quantity. The analytical solution of the one-dimensional advection-diffusion equation is presented in red. The numerical solution is presented as a black-dotted line. This numerical solution has been obtained with a finite difference method. The same oscillatory behavior can take place with finite element methods [48]. Figure from [48].

Chapter 5

Code comparison: PLAXIS and CODE_BRIGHT

In chapter 4 the results from PLAXIS have been compared with analytical equations. This was done in an attempt to verify the proper code implementation of the governing equations. This however gives no information about how well the model compares to experimental results. In order to investigate this, comparisons are made between the model predictions of PLAXIS and the geotechnical finite element package CODE_BRIGHT [30]. The latter has been extensively verified and validated in international benchmark tests such as EVEGAS, CATSIUS CLAY and C2S2 [31]. The goal of this code comparison is to obtain good agreement between the THM-kernel of PLAXIS and CODE_BRIGHT. Establishing this correspondence would mean that the THM-behavior of PLAXIS can be linked to experimental results, since this has already been done for CODE_BRIGHT [41] [45]. CODE_BRIGHT has been created by the research group of Gens, Alonso and Olivella at the department of geotechnical engineering and geosciences at the polytechnical university of Catalonia (UPC).

5.1 Mock-up test

Most conceptual designs for the storage of nuclear waste envisage the placement of canisters in horizontal drifts or vertical boreholes [45]. Compacted expansive clay is used as a buffer between the canisters and the host rock. A shotcrete plug can then be installed to close the drift or borehole [16]. Due to the heat generated in the canisters and the groundwater that hydrates the expansive clay, a complex thermo-hydro-mechanical scenario is created. The FEBEX research project was initiated in order to study the behavior of clay in repository conditions [25]. The project consisted of three parts. In one part a full scale investigation in a drift at a test site in Grimsel (Switzerland) was performed. The heterogeneities in the host rock such as cracks, fractures and geological contacts pose a challenge. In order to have full control of the boundary conditions such as water influx, external boundary temperature and internal heat generation, a large model was created in the laboratory which tried to mimic the geometry of the full scale test site. Heaters were used to represent the canisters. These heaters were installed in a large steel confining structure with a cylindrical shape [16]. Tight-fitting bentonite blocks were installed around the heater, see figure 5.1. The experiment performed with this large model is refered to as the FEBEX mock-up test. The results obtained from this experiment have been compared with a numerical simulation of the experiment in "CODE_BRIGHT" and a good match was obtained [45]. The next section will therefore be focused on matching this heater experiment in PLAXIS.

5.2 Preparation

The balance equations used in CODE_BRIGHT are very similar to those implemented in PLAXIS. This provides a good starting point for the matching procedure that will be used here. CODE_BRIGHT uses the temperature extended Barcelona Basic Model for unsaturated soils. It uses this constitutive model in order to match the results from the experimental mock-up test which is described in section 5.1. This temperature extended BBM uses a temperature dependent suction yield surface [37]. The apparent preconsolidation pressure can also assume a temperature dependency. The soil stiffness depends on the suction which in turn depends on the temperature through a temperature dependent retention curve. No

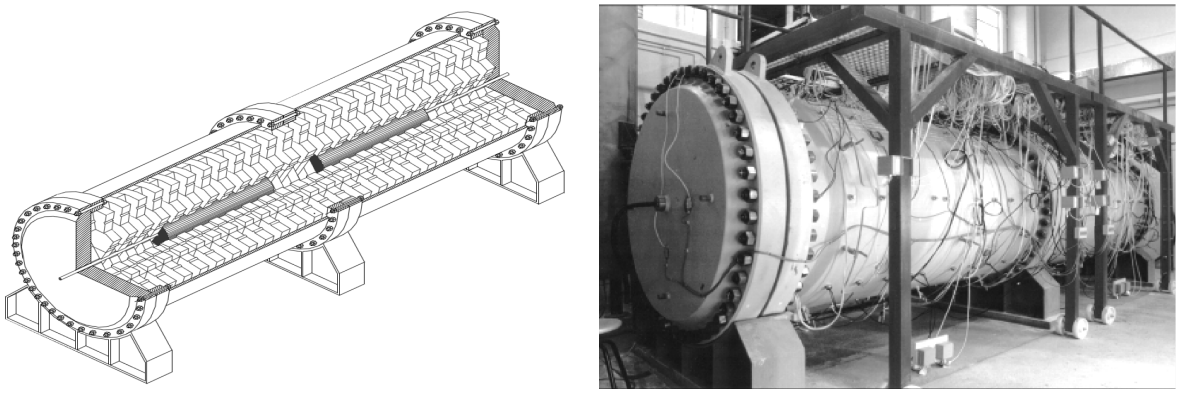

(a) **(b)**

Figure 5.1: a): The configuration of the mock-up experiment. The steel confining structure contains two cylindrical heaters. Interlocking bentonite blocks are placed around the heaters. Placement of the sensors is not displayed in this figure. The bentonite can be hydrated at the contact with the confining structure. b): A photograph showing the laboratory configuration. Figures from [25]

temperature dependent constitutive model for unsaturated soils is available yet in PLAXIS. Temperature only appears as an unknown in the balance equations. Section 2.4 demonstrates that the effect of temperature on the mechanical behavior of clays can not be neglected. Without the implementation of a temperature dependent constitutive model in PLAXIS it is to be expected that model output for the mock-up experiment will show differences compared to the model output of CODE_BRIGHT since a large range of temperatures has been measured. By modeling a fully saturated version of the mock-up test and selecting a suitable set of parameters the temperature extended BBM will reduce to the MCC which can be modeled in PLAXIS. With this simplified scenario a code comparison can be performed since temperature now only appears in the balance equations and not in the constitutive model. The results of PLAXIS and CODE_BRIGHT should be similar in this case. As soon as temperature dependent constitutive models are implemented in PLAXIS, the next step towards matching the real mock-up test can be done.

The following set of equations defines the parameters used in the temperature dependent BBM as implemented in CODE_BRIGHT:

$$d\varepsilon_v^e = \frac{\kappa_i(s)}{1+e}\frac{dp'}{p'} + \frac{\kappa_s(p',s)}{1+e}\frac{ds}{s+0.1} + (\alpha_0 + 2\alpha_2\Delta T)dT \tag{5.1}$$

Equation (5.1) describes the elastic volumetric strain as function of suction, temperature and effective mean stress. The term $\frac{\kappa_i(s)}{1+e}$ is equivalent to $\frac{\kappa_i(s)}{\nu}$ which is similar to κ^* as expressed in equation (2.54) and (2.43) with the only difference that ν is used instead of ν_0. So κ_i is equivalent to κ in the MCC, describing the elastic slope in the specific volume vs $\ln(p')$ graph.

$$\kappa_i(s) = \kappa_{i0}(1 + \alpha_i s) \tag{5.2}$$

Equation (5.2) describes the suction dependency of κ_i, which is an adaptation of the constant κ in the original BBM presented in section 2.3.2.

$$\kappa_s(p',s) = \kappa_{s0}(1 + \alpha_{sp} ln\left(\frac{p'}{p_{ref}}\right) exp(\alpha_{ss} s) \tag{5.3}$$

κ_s presented in equation (5.3) has a similar function as κ_i, but κ_s describes the specific volume response to a change in suction s. In contrast to the constant κ_s in the original BBM, κ_s in this updated model depends on the effective mean stress and suction.

$$p_0 = p^c \left(\frac{p_0^*(T)}{p^c}\right)^{\frac{\lambda(0)-\kappa_{i0}}{\lambda(s)-\kappa_{i0}}} \tag{5.4}$$

The apparent preconsolidation pressure p_0 expressed in equation (5.4) depends on the temperature dependent saturated preconsolidation pressure $p_0^*(T)$ expressed in equation (5.5) and on the suction

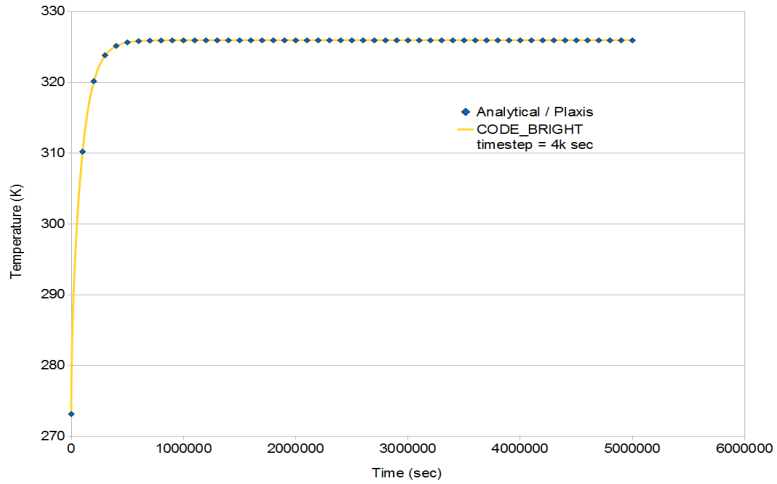

Figure 5.2: Matching CODE_BRIGHT for the simple one-dimensional non-porous geometry. See figure 4.2 for reference.

dependent plastic yielding parameter $\lambda(s)$ described by equation (5.6).

$$p_0^*(T) = p_0^* + 2(\alpha_1 \Delta T + \alpha_3 \Delta T|\Delta T|) \tag{5.5}$$

$$\lambda(s) = \lambda(0)\left[(1-r)exp(-\beta s) + r\right] \tag{5.6}$$

$$p_s = p_{s0} + ks\ exp(-\rho \Delta T), \Delta T = T - T_{ref} \tag{5.7}$$

p_s in equation (5.7) gives the temperature dependent suction increase (SI) yield surface.

$$\rho_l = \rho_{l0}\left(1 + \beta_{wP}(P_l - P_{l0}) + \beta_{wT} T\right) \tag{5.8}$$

The liquid density as function of temperature and pressure is given in (5.8).

$$\mu_l = Aexp\left(\frac{B}{273.15 + T}\right) \tag{5.9}$$

Viscosity depends on temperature according to expression (5.9).

$$\kappa^{int} = \kappa_0 \frac{\phi^3}{(1-\phi^2)} \frac{(1-\phi_0^2)}{\phi_0^3}\mathbf{I} \tag{5.10}$$

κ^{int} in equation (5.10) describes the intrinsic permeability as function of reference porosity ϕ_0. Selecting $\phi_0 = 0$ enables a trigger that makes the intrinsic permeability independent of porosity changes.

$$\lambda_T = \lambda_{sat}^{Se} \lambda_{dry}^{1-Se} \tag{5.11}$$

Finally, λ_T give the thermal conductivity as function of the effective saturation and the dry and saturated thermal conductivities. It should be noted that CODE_BRIGHT measures temperature in degrees Celcius. Water pressure is positive but other compressive stresses are negative.

5.3 Matching 1D non-porous

As a preliminary investigation an attempt is made to match the temperature evolution of the one-dimensional column of material described in section 4.1 with CODE_BRIGHT. Figure 5.2 shows that CODE_BRIGHT matches PLAXIS and the analytical solution perfectly.

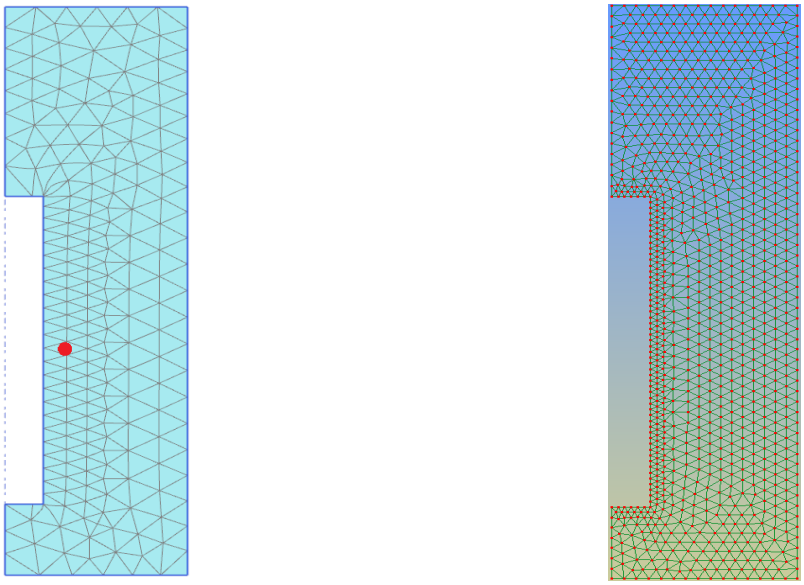

(a) (b)

Figure 5.3: The axisymmetric geometry of the heater is in accordance with the CODE_BRIGHT tutorial. The radius of the heater is 0.81 meters and the height is 3.0 meters. The heating element has a radius of 0.17 meter. a) PLAXIS geometry and mesh with 15-noded elements. b) CODE_BRIGHT geometry and mesh with 3-noded elements. The red dot in figure a) gives the location of the point at which time graphs are made in PLAXIS and CODE_BRIGHT.

5.4 Saturated non-linear elastic heater

The Barcelona Basic model is an extension of the modified Cam-Clay model and reduces to it when suction goes to zero, see section 2.3.2. So by modeling a fully saturated soil and selecting parameters in such a way that the temperature dependence of the BBM falls away, the same constitutive model is used in PLAXIS and CODE_BRIGHT. Elastic behavior is guaranteed by making the yield surface sufficiently large and ensuring that the stress state stays within it during the entire duration of the experiment. The goal is to obtain similar results in CODE_BRIGHT and PLAXIS under these conditions. This would verify that the balance equations and the solution scheme of PLAXIS and CODE_BRIGHT give similar results.

The axisymmetric geometry of the heater is constructed according to the CODE_BRIGHT tutorial, see figure 5.3. Figure 5.1 shows that the heater is placed horizontally, which means that gravity is a function of the angular coordinate θ and can not be modeled with axisymmetry. However, the weight γ is currently used as an input parameter in PLAXIS and is equal to the density multiplied by the gravity. In order to obtain the density, the weight is divided by the gravity, which will give problems when the gravity is set to zero. Since setting zero gravity is not possible in the current version of PLAXIS the heater experiment will be modeled with normal gravity pointing in the negative y direction, even though this is not physical. But since the aim of this code comparison is merely to obtain good agreement between PLAXIS and CODE_BRIGHT this is not a problem. The effect of the non-physical gravity should be the same in both scenario's if PLAXIS and CODE_BRIGHT work similarly.

5.4.1 Model parameters CODE_BRIGHT

The model parameters used in this code comparison are taken from the mock-up test [45] and from CODE_BRIGHT's heater tutorial [37]. Since only (non-linear) elastic fully saturated behavior will be investigated, parameters dealing with the yield surface and the suction behavior have been altered. Table 5.1 shows all the input parameters that are used for CODE_BRIGHT during the code comparison. The saturated preconsolidation pressure p_0^* has been made sufficiently large to ensure elastic behavior during the entire experiment. The values for the plastic yielding parameter λ which are expressed in equation (5.6) are for convenience left on their default values specified by [45] and [37]. They will have no mechanical effect though since yielding will not occur. The same can be said about the parameters associated with the yield suction p_{s0}. Constant viscosity will be assumed for simplicity.

Table 5.1: Input parameters used during phase one of the code comparison. The parameters used in CODE_BRIGHT and PLAXIS are plotted next to each other.

CODE_BRIGHT		
Parameter	Value	Unit
κ_{io}	0.04	-
κ_{so}	0.0	-
$\lambda(0)$	0.15	-
ν	0.4	-
α_{ss}	0.0 -	
α_i	0	-
α_{sp}	0	-
α_0	$1.5 * 10^{-4}$	$^\circ C^{-1}$
α_1	0	-
α_2	0	-
α_3	0	-
T_0	20	$^\circ C$
p_{ref}	0.01	MPa
β	0.05	MPa^{-1}
r	0.75	-
p_0^*	1000	MPa
p^c	0.1	MPa
p_{s0}	1000	MPa
ρ	0.2	$^\circ C^{-1}$
k	0.1	-
M	3.0	-
α	0.3	-
e_0	0.667	-
λ_{dry}	0.47	$Wm^{-1}K^{-1}$
λ_{sat}	1.15	$Wm^{-1}K^{-1}$
κ_0	1.9×10^{-21}	m^{-2}
ϕ_0	0.0	-
ρ_{l0}	1000	$kg\ m^{-3}$
β_{wP}	4.58×10^{-4}	MPa^{-1}
β_{wT}	2.1×10^{-4}	$^\circ C^{-1}$
A	$1.002\ \times 10^{-9}$	$MPa\ s$
B	0	-
C_s	1000	$Jkg^{-1}K^{-1}$
ρ_s	2770	$kg\ m^{-3}$

PLAXIS		
Parameter	Value	Unit
κ	0.04	-
λ	0.15	-
p^c	10^9	Pa
ρ_s	2770	$kg\ m^{-3}$
C_s	1000	$J\ kg^{-1}K^{-1}$
λ_s	131×10^9	$J\ day^{-1}K^{-1}$
λ_w	51.84×10^9	$J\ day^{-1}K^{-1}$
β_{wP}	4.58×10^{-10}	Pa^{-1}
β_{wT}	2.1×10^{-4}	K^{-1}
k	$1.61\ \times 10^{-9}$	$m\ day^{-1}$
β_{DT}	$1.5\ \times 10^{-4}$	K^{-1}
e_{init}	0.667	-
ϕ_{init}	0.4	-
c_k	1.0×10^{15}	-
μ_{20}	1.16×10^{-8}	$Pa\ day$
$\beta_{DT,x}$, $\beta_{DT,y}$, $\beta_{DT,z}$	$0.5 * 10^{-4}$	$^\circ C^{-1}$
β_{sT}	$1.5 * 10^{-4}$	$^\circ C^{-1}$

CODE_BRIGHT uses the software package GID for visualization purposes. The free version of this program restricts the amount of internal nodes to 1010. Since the largest gradients are expected in the vicinity of the heater the mesh will be refined there. The global mesh density will then be increased until the 1010 node restriction is reached. The resulting mesh is displayed in figure 5.3b.

5.4.2 Model parameters PLAXIS

The model parameters used in PLAXIS are specified in table 5.1. The units used in PLAXIS are days, Newtons and meters, so all quantities are expressed in these units. Similar to CODE_BRIGHT the viscosity of water is assumed to be constant (μ_{20}) for simplicity. The saturated hydraulic conductivity k in PLAXIS is selected by using $\kappa^{int} = \kappa_0$ from the CODE_BRIGHT entry of table 5.1:

$$k = \frac{\kappa^{int}\rho_w g}{\mu_{20}} = \frac{1.9 \times 10^{-21} \times 1000 \times 9.81}{1.002 \times 10^{-3}} = 1.86 \times 10^{-14} m\ s^{-1} = 1.61 \times 10^{-9} m\ day^{-1} \tag{5.12}$$

The thermal conductivity in PLAXIS and CODE_BRIGHT is calculated differently. CODE_BRIGHT uses equation (5.11) while PLAXIS uses (3.40). The code comparison will use fully saturated conditions. The thermal conductivity in CODE_BRIGHT therefore reduces to the saturated thermal conductivity.

Or in other words, $\lambda = \lambda_{sat}$. By using this equality and equation (3.40) an expression for λ_s is derived.

$$\lambda_s = \frac{\lambda_{sat} - \phi\lambda_w}{(1-\phi)} = 1.52 W m^{-1} K^{-1} = 131.0 kJ\ day^{-1} m^{-1} K^{-1} \tag{5.13}$$

By setting $\phi_0 = 0$ in CODE_BRIGHT the intrinsic permeability became independent of volumetric strain. The value c_k in table 5.1 influences the change of permeability in PLAXIS when a soil is compressed. Using a value of 1.0×10^{15}, as suggested by the user manual, will also make the permeability independent of the volumetric strain in the PLAXIS model.

The mesh used in the PLAXIS model uses the default medium mesh density. Just as in CODE_BRIGHT the mesh is refined around the boundary of the heater. The standard 15-noded elements are used. The resulting mesh has approximately 3000 nodes which is more than the 1010 nodes used in CODE_BRIGHT. Experimentation with the models has shown that the higher nodal density of PLAXIS can better capture peak volumetric strains and peak effective mean stresses. The coarser mesh of CODE_BRIGHT has problems with this.

5.4.3 Boundary conditions

The heater generates approximately 500W. This translates to approximately 260 Watt per square meter on the boundaries of the heater if the assumption is made that heat flux on the boundary of the heater is homogeneous. The outer radial boundary has a fixed temperature of 20 degrees Celcius. The initial temperature of the soil is set to the same temperature. All the other boundaries have zero heat flux assigned to them. The material is free to slide along the boundaries, but the boundaries themselves can not move outwards. Also, all boundaries are closed for water flow to avoid the problem with the advective transport of heat in PLAXIS, which is described in section 4.3.2. The soil and the water expand as a reaction to the heating. Due to the fixed boundaries the total volume can not increase which will result in an increase in pressure. The clay in the heater is pre-stressed to 10 MPa and the soil is fully saturated with an initial water pressure of 1 MPa. The latter is done to ensure full saturation during the entire heating phase and to make the effects of the non-physical gravity on the pore water pressure negligible. A time span of 100 days will be modeled.

5.4.4 Results and discussion

In PLAXIS the thermal volumetric expansion β_{sT} of the soil grains is calculated by summing the expansion of the soil in the x, y and z directions. This was expressed by equation (3.56). The volumetric thermal expansion of the solid grains was assumed to be equal to the volumetric thermal expansion of the soil itself. This assumption was based on the work of Khalili [20]. In CODE_BRIGHT the volumetric thermal expansion of the soil is given by parameters α_0, see table 5.1. The thermal expansion of the solid grains (α_s) can be entered independently. CODE_BRIGHT's manual gives the following description of α_s:

α_s: *Linear thermal expansion coefficient for grains (not volumetric) (default=0.0). This does not produce thermal expansion of the medium.*

This suggests that the value of α_s should be equal to $\beta_{DT,x} = \beta_{DT,y} = \beta_{DT,z}$ which is $0.5 \times 10^{-4}\ ^\circ C^{-1}$ according to the Plaxis entry of table 5.1. But the results of CODE_BRIGHT and PLAXIS compare much better when α_s is chosen to be equal to the volumetric thermal expansion of the soil grains β_{sT} which is $1.5 \times 10^{-4}\ ^\circ C^{-1}$. Maybe the '*(not volumetric)*' part of the description emphasizes that the volumetric expansion of the soil grains does not produce volumetric expansion of the soil itself in CODE_BRIGHT. Or the manual has not been updated properly. Since the proper value of α_s is unclear, figures will be displayed for $\alpha_s = 0.5 \times 10^{-4}\ ^\circ C^{-1}$ and $\alpha_s = 1.5 \times 10^{-4}\ ^\circ C^{-1}$. The cross-sections of different quantities at $t = 100$ days are plotted in figures 5.4 - 5.7.

Temperature

The temperature cross-sections plotted in figure 5.4 are very similar for all the three models. Since the soil in the heater is fully saturated and the boundaries are closed for water flow the water mass flux will be very small. The maximum temperature obtained in all three models is exactly 351.0 $^\circ K$. This similarity is not surprising since the advective energy flux is very small due to the negligible pore

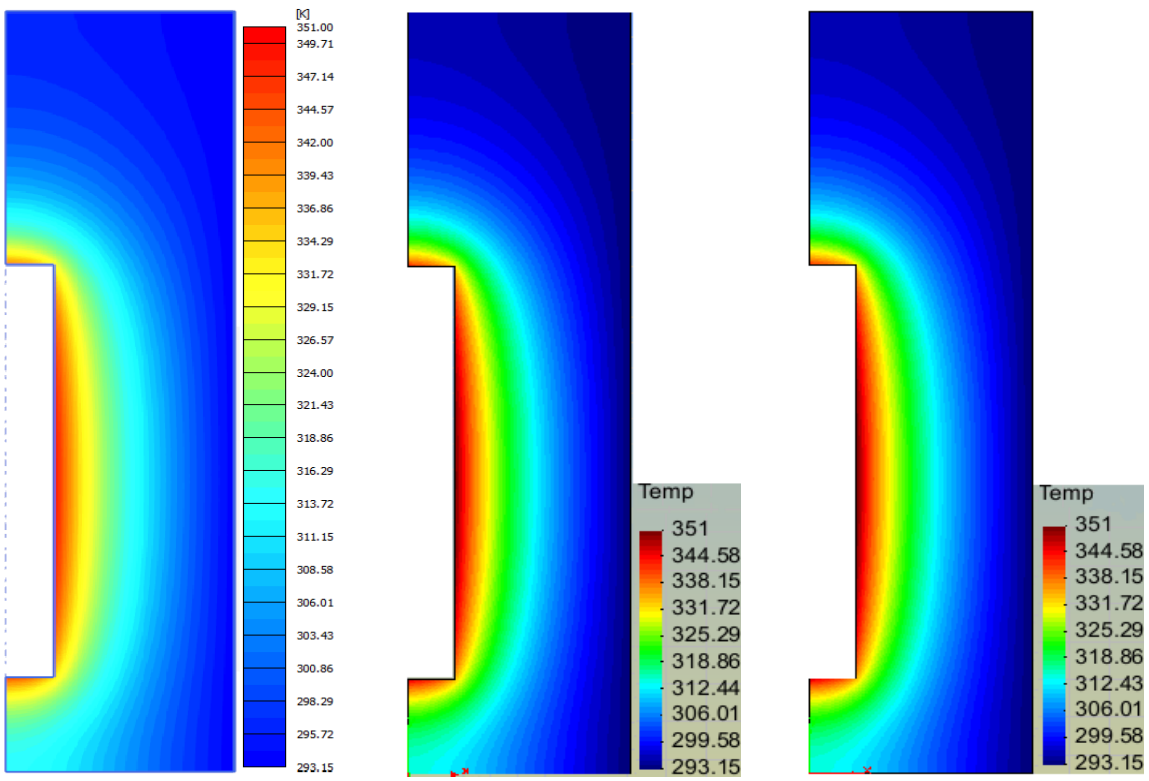

Figure 5.4: Temperature [K] at t=100 days: a) PLAXIS. b) CODE_BRIGHT with $\alpha_s = 1.5 \times 10^{-4}\ ^{\circ}C^{-1}$. c) CODE_BRIGHT with $\alpha_s = 0.5 \times 10^{-4}\ ^{\circ}C^{-1}$

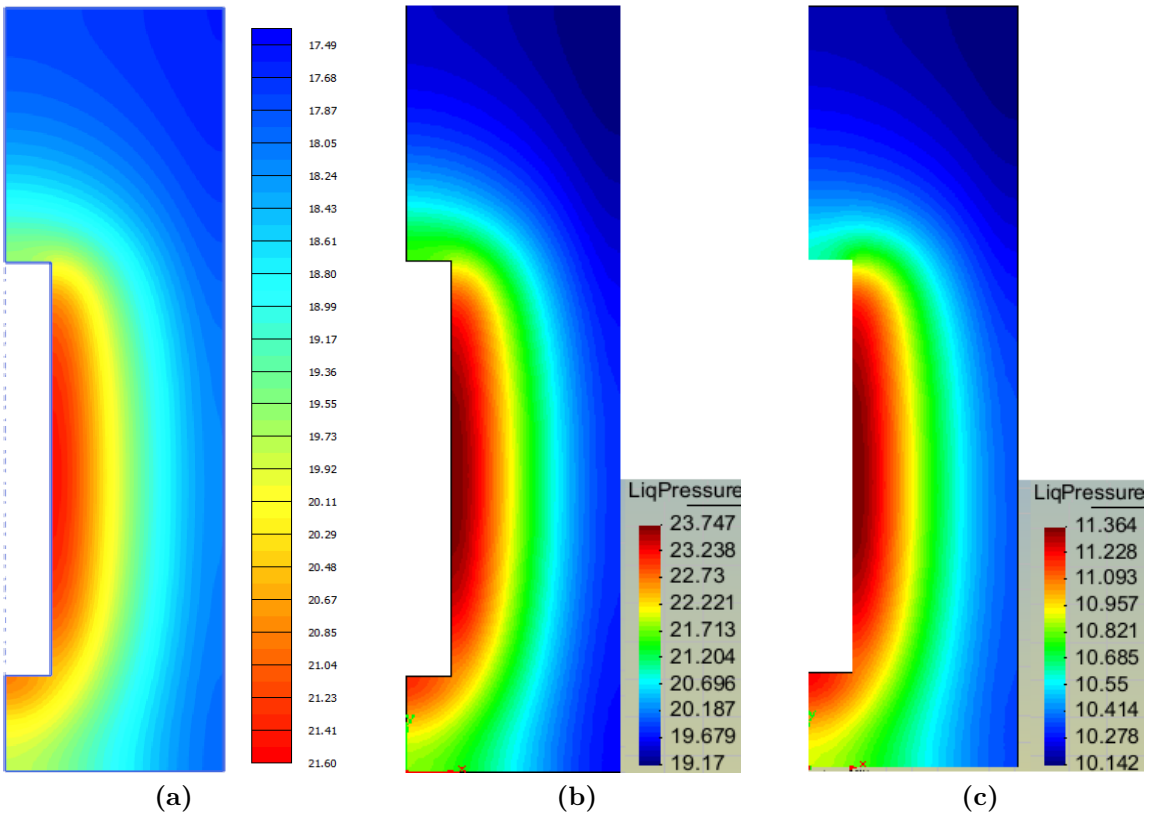

Figure 5.5: Water pressure [MPa] at t=100 days: a) PLAXIS. b) CODE_BRIGHT with $\alpha_s = 1.5 \times 10^{-4}\ ^{\circ}C^{-1}$. c) CODE_BRIGHT with $\alpha_s = 0.5 \times 10^{-4}\ ^{\circ}C^{-1}$

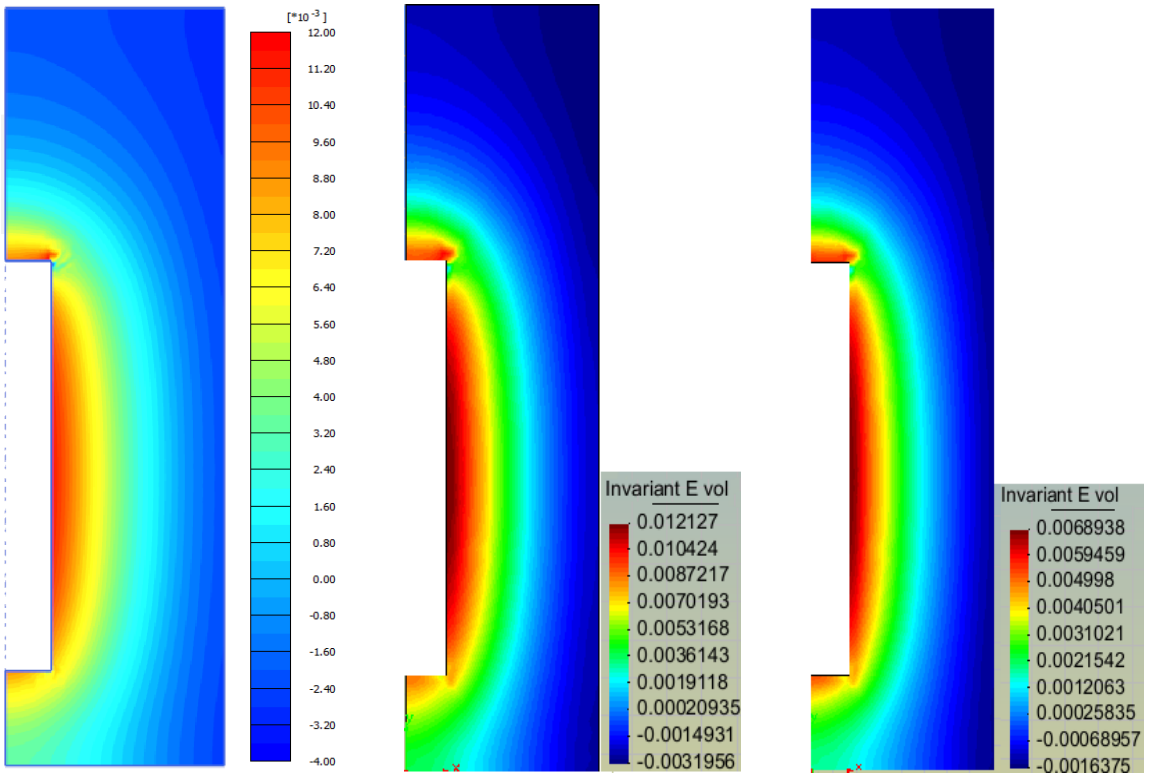

(a) **(b)** **(c)**

Figure 5.6: Volumetric strain [-] at t=100 days: Positive values represent expansion. a) PLAXIS. b) CODE_BRIGHT with $\alpha_s = 1.5 \times 10^{-4}\ ^{\circ}C^{-1}$. c) CODE_BRIGHT with $\alpha_s = 0.5 \times 10^{-4}\ ^{\circ}C^{-1}$

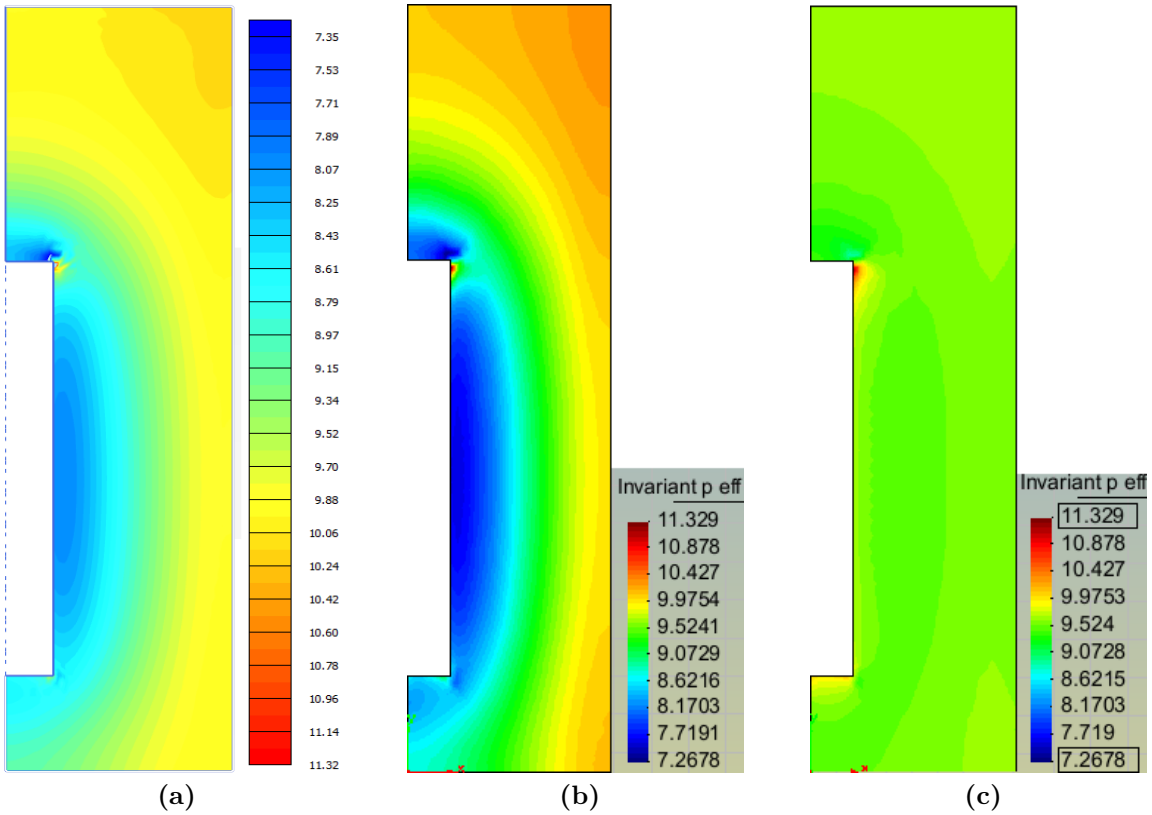

(a) **(b)** **(c)**

Figure 5.7: Mean effective stress [MPa] at t=100 days: Positive values represent pressure. a) PLAXIS. b) CODE_BRIGHT with $\alpha_s = 1.5 \times 10^{-4}\ ^{\circ}C^{-1}$. c) CODE_BRIGHT with $\alpha_s = 0.5 \times 10^{-4}\ ^{\circ}C^{-1}$. Legends equalized with b) due to disturbance of peak behavior

water velocity. It has already been proven in section 4.1 and 5.3 that the energy balance equations implemented in PLAXIS and CODE_BRIGHT match the analytical solution of the one-dimensional heat-diffusion equation. This makes it likely that the higher-dimensional heat diffusion is also correctly implemented, since it is modeled by the same section of code. Heat diffusion dominates in the two-dimensional cylindrical scenario modeled in this section. It is therefore not surprising that the models produce the same temperature profile. The two CODE_BRIGHT Models use different values for the thermal expansion of the solid grains, for the reasons explained in the previous paragraph. The different thermal expansion will influence the water pressure and therefore also the flux of water. But in both cases the advective energy flux is negligible.

Figure 5.8 plots temperature as function of time for a point close to the middle of the heater, see the red dot in figure 5.3a. This figure shows that the temperature evolution at this location is also the same for all three models. The lines representing the different models are indistinguishable. The temperature at this point remains approximately constant after 30 days.

Pore pressure

Figure 5.5 displays cross sections of the water pressure. PLAXIS matches the CODE_BRIGHT model with $\alpha_s = 1.5 \times 10^{-4}$ quite well. The difference in pore water pressure is approximately 10%. The highest pore water pressure occurs at the middle of the long side of the heating element. In both cases the water pressure at the bottom is significantly larger than at the top. This is not a hydrostatic pressure increment caused by the gravity present in the model, since this difference in water pressure exceeds 1 MPa while the difference in the y-coordinate is only 1.625 meters. The horizontal boundary at the bottom is closer to the heater than the horizontal boundary at the top. Since no heat flow occurs through these horizontal boundaries, the temperature at the bottom rises more than at the top. This will result in a higher water pressure at the bottom. The horizontal boundary also limits the flow of water which makes it harder for the excess pressures to dissipate compared to the top of the heating element. This will result in the high water pressures to be sustained longer at the bottom.

The lowest pore water pressure is present at the top-right of the model. The pressure disturbance at the boundary of the heater will propagate towards the cool regions of the heater by means of a water mass flux. The top-right is furthest away from the heating element and it will therefore take the most time for the water pressure to rise there. Still, the water pressure in this corner increased significantly with respect to the initial water pressure of 1 MPa, even though the temperature has not significantly increased at this point.

The water pressure in the CODE_BRIGHT model with $\alpha_s = 0.5 \times 10^{-4}$ is much lower than when the solid expansion $\alpha_s = 1.5 \times 10^{-4}$. The volume increment of the solid phase is reduced in this case so the water is compressed less. The predicted water pressure values are also much lower than the values predicted by PLAXIS.

Figure 5.10 plots water pressure as function of time. Two additional models are added to the three models presented in figure 5.5. These two models investigate the effect of having variable viscosity as illustrated by figure 5.9. It turns out that variable viscosity has a negligible effect on the temperature distribution and evolution within the model. The advective energy flux remains negligible. For this reason the variable viscosity models were not plotted in the temperature-time graph of figure 5.8.

For all the five models it can be seen that the water pressure reaches its maximum value between 20 and 30 days. This is the moment at which the temperature at this point approaches its maximum value as can be seen in figure 5.8. The associated water pressure increment therefore also comes to a halt. The pressure gradient within the soil will result in a mass flux of water. Water flows away from regions with high water pressure to regions where the water pressure is low. This will result in a reduction of the water pressure after the peak temperature has been reached. The effect of having variable viscosity does have an influence on the pressure evolution within the heater.

Let's first investigate the effect on the CODE_BRIGHT model with $\alpha_s = 1.5 \times 10^{-4}$. At approximately t = 20 days the peak temperature is reached. The viscosity in the variable viscosity model is always lower than the constant viscosity μ_{20} since the temperature within the heater is always higher than 20 degrees Celcius. Viscosity as function of temperature is plotted in figure 5.9. The variable viscosity model therefore has a higher permeability and the pressure gradient will dissipate faster. The pressure at the point will therefore reduce quicker after reaching its maximum at t = 20 days when variable viscosity is used.

A similar effect occurs in PLAXIS when variable viscosity is activated. With variable viscosity the pressure dissipates faster after reaching its maximum. Before t = 20 days another interesting effect is

visible though. The pore pressure in the variable viscosity model is slightly higher than than that of the constant viscosity model. This can be explained in the following way: the soil closest to the heater will heat up the quickest resulting in a very high water pressure. The water pressure further away from the heater will initially be less affected since heating did not occur here yet. The pressure slope close to the heater is therefore initially much higher than the pressure slope further away. This gives rise to a net flux of water towards the point at which the water pressure is plotted. In turn this will result in a positive pressure contribution during the first days of the model. The magnitude of this contribution is amplified by having variable viscosity since the flow of water resulting from this pressure gradient is larger. Later when the temperature profile is stable water will start to flow towards the outer regions of the heater where the water pressure is low since it heated up less. This dissipation of pressure goes faster with lower viscosity. The water pressure in the CODE_BRIGHT Model with $\alpha_s = 0.5 \times 10^{-4}$ also reaches its peak around t = 25 day, although the peak pressure is much lower.

Volumetric strain

Cross sections of the volumetric strain are plotted in figure 5.6. The PLAXIS model again shows the best agreement with the CODE_BRIGHT model that uses $\alpha_s = 1.5 \times 10^{-4}$. The volumetric strain calculated by PLAXIS and this CODE_BRIGHT model is very similar in magnitude. The maximum volumetric strain varies by less than 2% (0.01194 in PLAXIS vs 0.012127 in CODE_BRIGHT). The compressive volumetric strain shows a slightly larger deviation (-0.003935 in PLAXIS vs -0.0031956 in CODE_BRIGHT). The maximum compressive strain in CODE_BRIGHT occurs in the outer regions of the heater while the maximum compressive strain in PLAXIS occurs at the top-right of the heating element. This difference is caused by the different mesh-densitities. The mesh density in CODE_BRIGHT can not be increased due to the 1010 node limitation imposed by the graphical user interface GID. The mesh-density of PLAXIS can instead be reduced to approximate the density in CODE_BRIGHT. With this coarser mesh the maximum compressive strain in PLAXIS is also located in the outer regions of the heater. It agrees very well with the value from CODE_BRIGHT. By making the mesh in PLAXIS coarser the peak compressive strain at the top-right of the heating element can not be captured so well anymore.

At the top-right and bottom-right corners of the heating element a volumetric strain disturbance is present in all the models. The volumetric strain is lower at these locations (i.e. more compressive). This can be explained by the mechanical boundary conditions applied to the model. No movement perpendicular to any boundary is allowed while sliding along a boundary is allowed. The soil around the heating element expands and will therefore slide along the boundary. Around the corner points of the heater it will encounter soil expanding along a perpendicular boundary. Both soil regions try to expand towards the same area. This will result in more compressive stresses and strains at the corners. Because the boundaries are fixed the volume within the heater is constant. The expansion that occurs around the heating element has to be compensated by compression at places where the temperature increased less. The CODE_BRIGHT model with $\alpha_s = 0.5 \times 10^{-4}$ has volumetric strains that are much less expansive and also less compressive than in PLAXIS.

Effective mean stress

Figure 5.7 shows cross sections of the effective mean stress. Close to the top-right corner of the heating element the average mean stress exceeds 9 MPa in all models. The highest value (13.67 MPa) appears in the PLAXIS model, although this can not be seen in the cross-section due to the equalized legends. It exceeds the values from both CODE_BRIGHT models, but this can be explained by the fact that the resolution in the PLAXIS model is higher. It has more nodes and integration/stress points than the CODE_BRIGHT models. This higher mesh density allows the PLAXIS model to better capture the peak behavior. By using a coarser mesh this peak value is reduced together with the corresponding compressive volumetric strain peak.

Prior to the heating, a total stress of 10 MPa was applied to the soil. Because the initial water pressure is 1 MPa, the initial effective mean stress is 9 MPa. The volumetric strain is defined as zero at the initial temperature of $293.15°K$ and initial effective mean stress of 9 MPa. The volumetric strain can be decomposed in a mechanical and a thermal part. Effective mean stress above the reference value of 9 MPa will result in a compressive (elastic) mechanical volumetric strain as is illustrated by figure 2.9. The CODE_BRIGHT model shows an expansive volumetric strain at the top-right of the heating element. The expansive thermal component of the volumetric strain apparently compensates the compressive

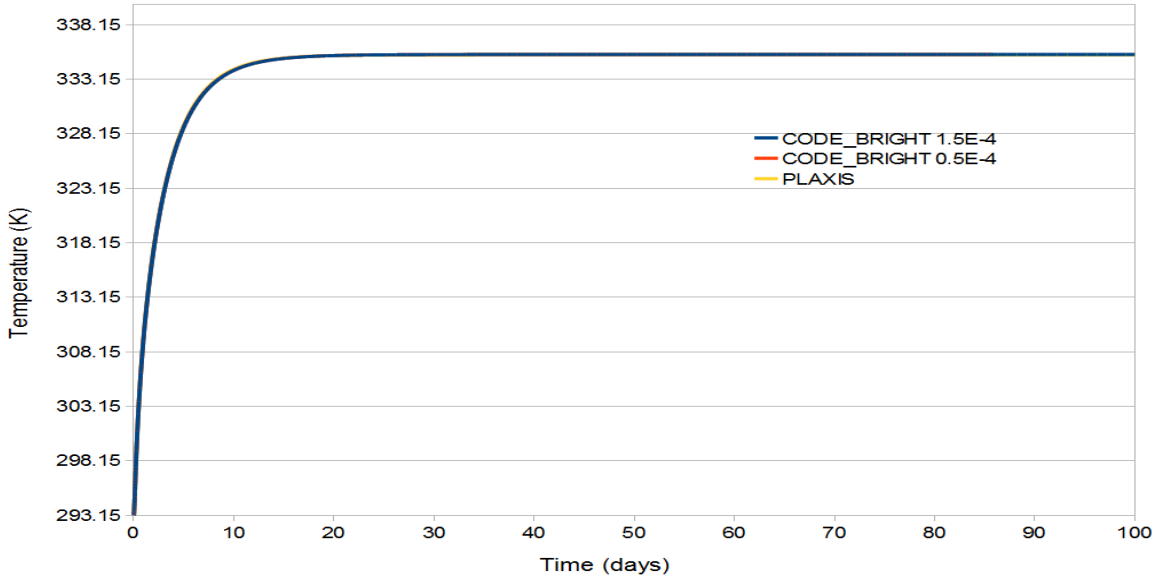

Figure 5.8: Temperature against time. The plots are made at a small distance from the middle of the heater, see the red dot in figure 5.3a.

mechanical volumetric strain component. The PLAXIS model which has a higher effective mean stress at this location shows a compressive volumetric strain in figure 5.6.

Slightly above the effective mean stress peak, there is an effective mean stress minimum. The minimum effective mean stress value of PLAXIS is 0.007043 and the minimum of the CODE_BRIGHT model is 0.0072678. The difference in the peak value and the difference in the minimum value is significantly reduced by using a coarser mesh in PLAXIS. Apart from the different effective mean stress peak and minimum value, the PLAXIS model and the CODE_BRIGHT model with $\alpha_s = 1.5 \times 10^{-4}$ agree very well. The effective mean stress close to the heating element is slightly lower in CODE_BRIGHT. This can be explained by the higher water pressure. The CODE_BRIGHT model with $\alpha_s = 0.5 \times 10^{-4}$ shows a much larger deviation.

Summary

Both the cross-sections and the time plots show great agreement between PLAXIS and CODE_BRIGHT, both in values and in trends. The CODE_BRIGHT model with $\alpha_s = 1.5 \times 10^{-4}$ gives results that are very similar to PLAXIS in all four cross-sections. The difference in the effective mean pressure spike close to the top-right heating element boundary is the result of the difference in mesh density. The mesh-density of CODE_BRIGHT can not be increased due to commercial nature of the visualization software. The coarser mesh of CODE_BRIGHT is not able to accurately represent this highly localized peak. Neglecting this spike, the liquid pressure is the quantity that deviates the most from PLAXIS but even in this case the difference is less than 10%. The liquid pressure in PLAXIS and CODE_BRIGHT also peaks approximately at the same time as can be seen in figure 5.10. The level of agreement between CODE_BRIGHT and PLAXIS is satisfactory, especially since the THM-implementation in PLAXIS is in its early stages of development.

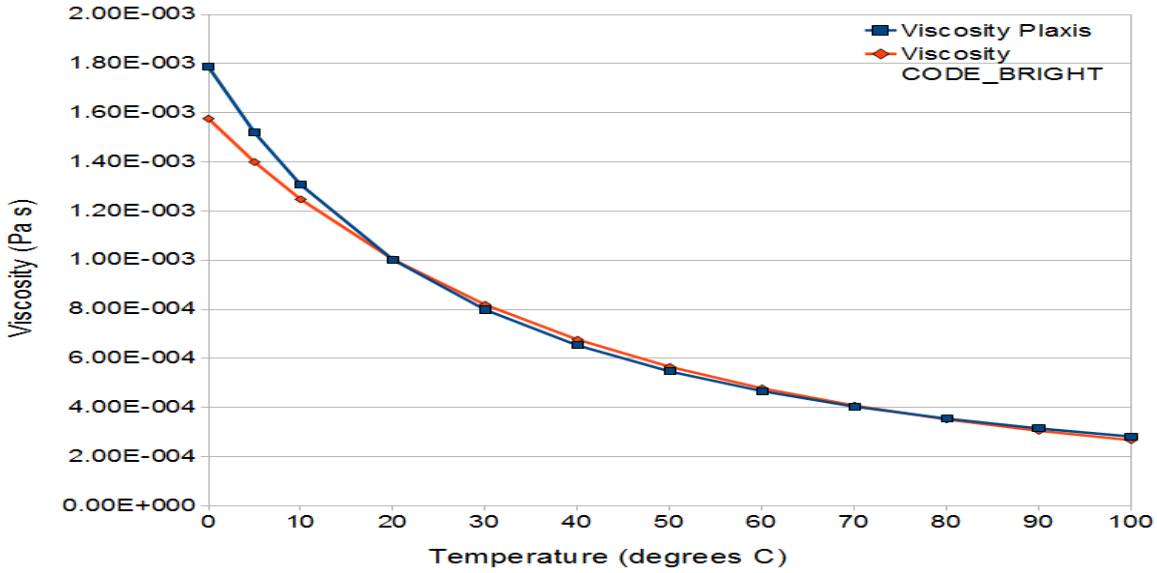

Figure 5.9: Temperature dependent viscosity in PLAXIS and CODE_BRIGHT. The values implemented in PLAXIS were introduced in table 3.2. CODE_BRIGHT suggests using A = 2.1×10^{-12} ($MPa\ s^{-1}$), B = 1808.5 (-) in combination with equation (5.9). Both implementations are very similar for the temperature range above 20 $°C^{-1}$ experienced in the heater.

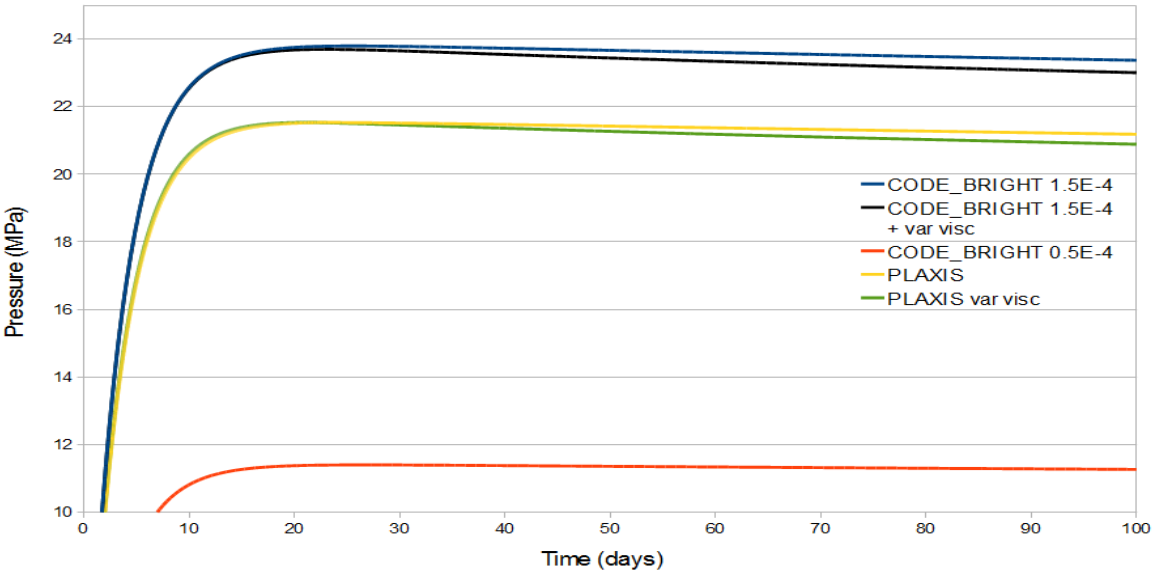

Figure 5.10: Water pressure against time. Note the non-zero origin of the pressure axis for visualization purposes. The plots are made at a small distance from the middle of the heater, see the red dot in figure 5.3a.

Chapter 6

THM Applications

6.1 Storage of nuclear waste

One of the main reasons for the interest in Thermo-Hydro-Mechanical coupling is the large influence that it has on the structural integrity of a clay barrier surrounding canisters of nuclear waste [47] [56] [43]. Temperature affects the mechanical characteristics of the clay as was discussed in section 2.4. The volumetric response of the clay with respect to changes in temperature and suction will influence its permeability and therefore also its capability to isolate the canisters from the environment. Vapor fluxes will also occur due to gradients in suction and temperature. The safe storage of radioactive waste is one of the main challenges associated with nuclear energy. Since leakage through the clay barrier would have a severe environmental impact, it is very important to be able to accurately model its long-term behavior. For this reason several full scale models are constructed in underground drifts in for instance Japan [43], the United States [41], Switzerland [14] and Sweden [46]. Large laboratory tests such as the mock-up test described in chapter 5 also illustrate the great importance of Thermo-Hydro-Mechanical coupling for the storage of nuclear waste.

6.2 Energy piles

A relatively stable temperature is present within the ground at depths exceeding 10 meter [50]. Energy piles are usually at least 15 meters long to ensure good contact with the soil whose temperature is relatively unaffected by seasons [44]. A u-shaped pipe is installed within the pile, forming a closed system for water circulation. Heat exchange with the soil takes place when the water flows through the pipe towards the bottom of the pile and then flows upwards towards the surface. This system can provide cooling during summer. In the winter the system can provide heating by using the relatively high temperature of the soil in combination with a heat pump. Figure 6.1 gives an overview of the system.

The THM-kernel could be used to model the seasonal temperature evolution in the soil. The correct functioning of the energy pile system depends on the capacity of the soil to maintain a relatively invariant temperature at depth. If the heat exchange with the pile causes the soil to heat too quickly during summer or cool too quickly during winter the system might lose its effectiveness. Using information about expected heat exchanged between the soil and the piles, the heat capacity and thermal conductivity of the soil and the groundwater flow, the thermal evolution of the deep soil can be modeled by PLAXIS. Additionally, the annual heating/cooling cycles of the soil around the piles may induce strains [28] which can be investigated by the THM-kernel.

6.3 Geothermal energy

Multiple techniques exist for the extraction of geothermal energy. First of all there is a distinction between open and closed systems. The depth from where the energy is obtained also varies: shallow systems go down to depths of 200 meters while deep systems may reach down more than a kilometer [3]. The extraction of geothermal energy in closed systems makes use of verical u-shaped heat pipes through which fluid circulates, see figure 6.2. On its way down the heat pipe water will heat up. This thermal energy will then be advected upwards where it may be used to heat houses or generate electricity.

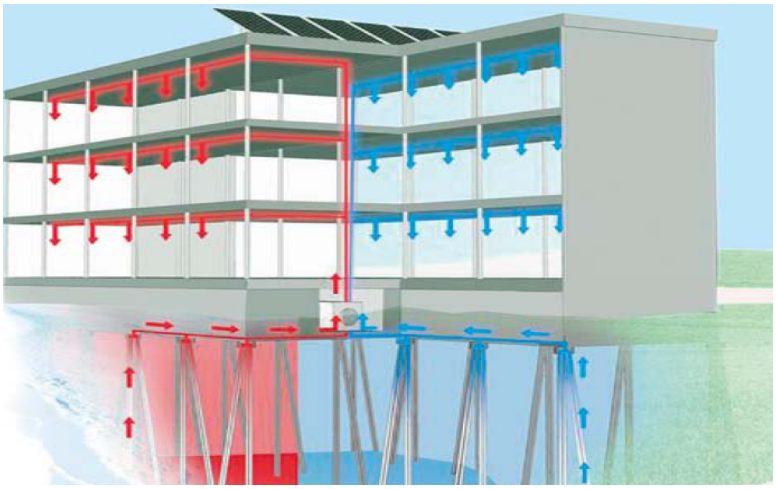

Figure 6.1: Schematic showing the function of energy piles. Huge energy savings can be achieved by utilizing the temperature of the deep ground which is relatively unaffected by seasonal variation. During winter (left side) heat is extracted from the ground, heating the building. During summer (right side) the deep ground is used for cooling the building. Figure from [44].

Just as the energy piles described in the last section, the heat pipes will disturb the temperature distribution within the soil. This will result in deformation of the soil which could be predicted by the THM-kernel of PLAXIS. Predicting the heat flow from the heat pipes (or from an energy pile) to the soil would require the introduction of a heat pipe 'structural object' in PLAXIS. The reason for this is that the temperature distribution within the heat pipe will depend on the fluids physical properties and the speed at which it flows through the heat pipe. Methods have been developed to model the thermal effects of heat pipes [3] [4]. These methods would have to be included in PLAXIS to model the heat transfer from energy piles or heat pipes. The groundwater velocity also plays an important role since it will influence the temperature profile around the heat pipes and therefore also the conductive heat transfer with the pipe.

6.4 Ground freezing

Ground freezing is a technique that has succesfully been used in tunneling and mining for over 100 years. An example of a tunneling project in which ground freezing has successfully been used is the No. 7 subway line extension in New York [51]. The tunnel was drilled primarily through hard bedrock. A certain section would have to be drilled through unconsolidated water bearing soils which were likely to flow. By freezing these soils the pore water would turn into ice. This would significantly increase the temporary strength of these soils. Another benefit of ground freezing is that it prevents groundwater from infiltrating the tunnel. After freezing, the TBM can drill through the bedrock and the frozen soil

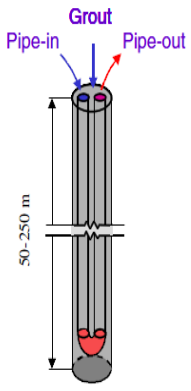

Figure 6.2: The structure of a vertical u-shaped heat pipe in a shallow closed system. Figure from [3].

alike. Freezing will support the unconsolidated soils until the tunnel lining segments are installed and grouted into place.

An example of the successful application of freezing in the mining industry is McArthur river Uranium mine [27]. By freezing the ore body the temporary stability can be increased. With this technique some ore bodies which were previously unfeasible to be mined can be extracted after all.

The ground freezing technique requires the installation of many freezing pipes. Refrigerated brine is pumped through these pipes, reducing the temperature of the rock/soil below the freezing point. In order to model the temperature of the pile a heat pipe 'structural object' has to be introduced within PLAXIS as was discussed in section 6.3.

The latent heat associated with the phase transition of water to ice has a profound influence on the temperature evolution of the ground. In addition the ground water flow patterns will also be altered when the ground freezes. Currently the PLAXIS THM-kernel does not include phase transitions. Further research and development is therefore required in order to extend the use of PLAXIS to ground freezing.

6.5 Other uses

Without going into details, some other topics related to THM-coupling are:

- Frost heaving is the result of the formation of ice-lenses underground. The magnitude of the heaving depends on the ability of the ice-lenses to draw up water from the soil. This in turn depends on the temperature and the permeability of the soil. Frost heaving can damage roads and buildings in countries that experience cold winters. It is therefore very useful to be able to accurately model this phenomenon.
- Temperature influences soil stiffness, suction and therefore also the cohesion. Temperature will therefore influence the safety factor of a construction. The magnitude of this influence could be investigated by a THM-model.
- Roads can be damaged during hot summers when the bitumous constituents of the aggregate (partially) melt. Thermal expansion and contraction may also induce cracks. Existing constitutive models for bitumous material could be extended to include this behavior. If this behavior could be correctly modeled the lifetime and required maintenance of a road could be better estimated.

Chapter 7

Conclusion

7.1 One dimensional nonporous heat conduction

Section 4.1 has proven that the numerical implementation of the energy balance equation matches the analytical solution for a non-porous one-dimensional material. It has been shown that the magnitude of the time-steps is of great importance for the transient phase of the model. It is therefore very important that PLAXIS will suggest suitable time-stepping parameters.

7.2 Two dimensional advection-diffusion of temperature

Analytical solutions have been presented in section 4.3.1 to verify the correct code implementation of the energy balance equation when advection takes place. The verification is currently not successful yet due to the limitations of the current kernel with respect to the hydraulic boundary conditions. This problem is described in more details in section 4.3.2. It is important that this complication has been discovered early in the development procedure. The finite element implementation of the advection-diffusion equation is notoriously challenging. Further research is required to determine the best way to deal with this problem.

7.3 Vapor diffusion

The correct implementation of the relative humidity, vapor density and the pressure gradient part of the vapor diffusion equation (3.20) has been verified in section 4.2. It has also been shown that the approximation (3.21) is valid for the model that is being investigated. Procedures like these can be very useful to make sure that the governing equations have been succesfully implemented.

7.4 Code comparison with CODE_BRIGHT

After having performed some investigations to verify the correct implementation of the governing equations, a numerical comparison with CODE_BRIGHT has been performed in section 5. The temperature agrees perfectly, both in the transient and the steady state phase. The largest deviation between the models appears in the water pressure. The difference between CODE_BRIGHT and PLAXIS is approximately 10%. The solid grain thermal expansion coefficient α_s is not very clearly defined in CODE_BRIGHT and it has been demonstrated that this parameter has a very large influence on the resulting water pressure. It may be that the difference between PLAXIS and CODE_BRIGHT is related to this parameter. Both the volumetric strain and the effective mean stress are very similar in magnitude and patterns in CODE_BRIGHT and PLAXIS. The agreement between CODE_BRIGHT and PLAXIS has been very good in general.

The fully saturated heater modeled in the code comparison is just the first step in the matching procedure. The complete mock-up test deals with an unsaturated clay which can experience plastic strains. Inflow of water takes place on the outer radial boundary, simulating the hydration due to the inflow of water from the host-rock in full-scale repository conditions. In order to correctly model the response

of the unsaturated clay subjected to suction and temperature gradients, a temperature dependent constitutive model is required for unsaturated soils. Such a model should incorporate stiffness and cohesion changes in addition to the volumetric response due to changes in suction and temperature. Section 2.3.2 and 2.4 have demonstrated that plastic strains can accumulate due to changes in temperature and suction. When a constitutive model with these capabilities is implemented in PLAXIS it will be possible to compare the level of agreement between PLAXIS and CODE_BRIGHT for the complete mock-up test.

Chapter 8

Acknowledgements

First of all I would like to thank Plaxis for providing me a thesis position and a valuable learning environment. I am also grateful for the help Dr. Galavi has given me. His insight in the theory and the numerical implementation proved to be very valuable. I would also like to thank Dr. Haxaire for his involvement in the process. His feedback on my ideas and his proofreading of this thesis were very useful. Dr. Brinkgreve helped me keep in mind the timeline by assuming the role of a manager. His feedback was very appreciated. Finally I would like to thank my examiner from LTU, Dr. Mattsson.

References

[1] Film notes for surface tension in fluid mechanics. `http://web.mit.edu/hml/ncfmf/04STFM.pdf`, 1969. Link last checked: May 25th, 2011.

[2] Q. Ai-fang, C. Guang-jing, T. Yong-wei, and S. De-an. Analytical solution to one-dimensional consolidation in unsaturated soils. *Applied mathematics and mechanics*, 28, 2008.

[3] R. Al-Khoury, P. G. Bonnier, and R.B.J. Brinkgreve. Efficient finite element formulation for geothermal heating systems. part i: Steady state. *International journal for numerical methods in engineering*, 63, 2005.

[4] R. Al-Khoury and P.G. Bonnier. Efficient finite element formulation for geothermal heating systems. part ii: Transient. *International journal for numerical methods in engineering*, 67, 2006.

[5] E.E. Alonso, A. Gens, and A. Josa. A constitutive model for partially saturated soils. *Geotechnique*, 3:405–430, 1990.

[6] K. Axelsson. *Constitutive modelling of soils.* Luleå University of Technology, 1994.

[7] J. Bonet. *Nonlinear Continuum Mechanics for Finite Element Analysis.* Cambridge university press, 1st edition, 1997.

[8] L. Börgesson, M. Chijimatsu, T. Fujita, T.S. Nguyen, J. Rutqvist, and L. Jinge. Thermo-hydro-mechanical characterisation of a bentonite-based buffer material by laboratory tests and numerical back analyses. *International Journal of Rock Mechanics and Mining Sciences*, 38:95–104, 2000.

[9] J.W.M. Bush. Surface tension module. `http://web.mit.edu/1.63/www/Lec-notes/Surfacetension/`. Link last checked: May 25th, 2011.

[10] D. Eberly. Derivative approximation by finite differences. `http://www.geometrictools.com/Documentation/FiniteDifferences.pdf`. Link last checked: May 25th, 2011.

[11] M.J. Fayer. *UNSAT-H Version 3.0: Unsaturated Soil Water and Heat Flow Model. Theory, User Manual, and Examples*, 2000.

[12] D.G. Fredlund and H. Rahardjo. *Soil mechanics for unsaturated soils.* Wiley, 1993.

[13] Y.-C. Fung and P. Tong. *Classical and computational solid mechanics.* World Scientific, 2001.

[14] A. Gens, A.J. Garcia-Molina, S. Olivella, E.E. Alonso, and F. Huertas. Analysis of a full scale in situ test simulating repository conditions. *International journal for numerical and analytical methods in geomechanics*, 22:515–548, 1998.

[15] J.U. Hasan and D.G. Fredlund. Pore pressure parameters for unsaturated soils. *Canadian geotechnical journal*, 17:395–404, 1980.

[16] F. Huertas, B. de la Cruz, J. L. Fuentes-Cantillana, E. Alonso, J. Linares, J. Samper, FJ. Elorza, C. Svemar, J-P. Salo, A. Muurinen, J. Pacovsky, J. Verstricht, B. Bazargan-Sabet, N. Jockwer, B. Vignal, H. Shao, W. Kickmaier, B. Baeyens, L. Börgesson, I. Rhen, F. Villieras, J.C. Robinet, and J.C. Gourry. Full-scale engineered barriers experiment for a deep geological repository for high-level waste in crystalline host rock – phase ii. *nuclear science and technology, European Union*, 2005.

[17] Intel®. Intel®math kernel library: Linear solver basics. http://cache-www.intel.com/cd/00/00/22/97/229716_229716.pdf. Link last checked: May 25th, 2011.

[18] K.B. Kaliszka. Developing a parallel solver for mechanical problems. Master's thesis, TU Delft, 2010.

[19] M. Åkesson. Temperature buffer test. evaluation modeling tbt_3 mock-up test. Technical report, SKB, 2008.

[20] N. Khalili, A. Uchaipichat, and A.A. Javadi. Skeletal thermal expansion coefficient and thermo-hydro-mechanical constitutive relations for saturated homogeneous porous media. *Mechanics of materials*, 42:593–598, 2010.

[21] S. Konyai, V. Sriboonlue, and V. Trelo-Ges. The effect of air entry values on hysteresis of water retention curve in saline soil. *American Journal of Environmental Sciences*, 5:341–345, 2009.

[22] F.J. Leij and J. H. Dane. Analytical solutions of the one dimensional advection equation and two- or three-dimensional dispersion equation. *Water resources research*, 26:1475–1482, 1990.

[23] P. Lollino, F. Cotecchia, L. Zdravkovic, and D.M. Potts. numerical analysis of the behavior of stiff clays under a rockfill embankment. In P. Mestat, editor, *5e Conférence Européenne Méthodes Numériques en Géotechnique*. Presses des Ponts, 2002.

[24] A. Maqsoud, B. Bussiere, M. Mbonimpa, and M. Aubertin. Hysteresis effects on the water retention curve: A comparison between laboratory results and predictive models. 57TH CANADIAN GEOTECHNICAL CONFERENCE, http://www.polymtl.ca/enviro-geremi/pdf/articles/H21.175.pdf. Link last checked: May 25th, 2011.

[25] P.L. Martin, J.M. Barcala, and F. Huertas. Large-scale and long-term coupled thermo-hydro-mechanic experiments with bentonite: the febex mock-up test. *Journal of Iberian geology*, 32(2):259–282, 2006.

[26] J.P. Monlouis-Bonnaire, J. Verdier, and B. Perrin. Prediction of the relative permeability to gas flow of cement-based materials. *Cement and Concrete Research*, 34:737–744, 2002.

[27] G.P. Newman. Case study: Thermal analysis of artificial ground freezing at mcarthur river uranium mine.

[28] D. Nicholson. Geotechnical aspects of energy geo-structures. http://lmswww.epfl.ch/common_documents/Amis_LMS+R/2009/Nicholson_GeotAspectsEnergyGeostr_01.09.pdf. EPFL Workshop 2009.

[29] M. Nuth and L. Laloui. A model for the water retention behavior of deformable soils including capillary hysteresis. GEO-FRONTIERS 2011.

[30] Polytechnical University of Catalonia (UPC). Code_bright. http://www.etcg.upc.edu/recerca/webs/code_bright/v3. Link last checked: May 25th, 2011.

[31] Polytechnical University of Catalonia (UPC). *Short Course CODE_BRIGHT, documentation.*, 2010.

[32] D. Or and M. Tuller. Capillarity. http://www.engr.uconn.edu/environ/envphys/pdf/vadose_pdf/Capillarity_revised01.pdf. Link last checked: May 25th, 2011. Lecture notes University of Connecticut.

[33] Plaxis. *Internal Hydro-Mechanical report*, 2010.

[34] Plaxis. *Plaxis material models manual*, 2010.

[35] Plaxis. *Plaxis scientific manual*, 2010.

[36] Plaxis. *Internal THM-report*, 2011.

[37] Polytechnical University of Catalonia (UPC). *CODE_BRIGHT TUTORIAL: VII. TUTORIAL EXAMPLE: THM Mockup-test problem.*

[38] J.N. Reddy. *An introduction to the Finite Element Method.* McGraw.Hill, 3rd edition, 2006.

[39] E. Romero and A. Gens. *Characterisation and thermo-hydro-mechanical behaviour of unsaturated Boom clay: an experimental study.* PhD thesis, Technical University of Catalonia (UPC), 1999.

[40] P. Roura and J. Fort. Local thermodynamic derivation of Young's equation. *Journal of colloid and interface science*, 272:420–429, 2004.

[41] J. Rutqvist, D. Barr, R. Datta, A. Gens, A. Millard, S. Olivella, C.-F. Tsang, and Y. Tsang. Coupled thermo-hydrological-mechanical analyses of the yucca mountain drift scale test – comparison of field measurements to predictions of four different numerical models. *International Journal of Rock Mechanics & Mining Sciences 42*, pages 680–697, 2005.

[42] J. Rutqvist, L. Börgesson, M. Chijimatsu, A. Kobayashi, L.Ling, T.S. Nguyen, J. Noorishad, and C.-F. Tsang. Thermohydromechanics of partially saturated geological media: governing equations and formulation of four finite element models. *International Journal of Rock Mechanics and Mining Sciences*, 38:105–127, 2000.

[43] J. Rutqvist, L. Börgesson, M. Chijimatsu, T.S. Nguyen, L. Jing, J. Noorishad, and C.-F. Tsang. Coupled thermo-hydro-mechanical analysis of a heater test in fractured rock and bentonite at kamaishi mine – comparison of field results to predictions of four finite element codes. *International Journal of Rock Mechanics & Mining Sciences 38 (2001) 129-142*, 38:129–142, 2001.

[44] Ruukki. Energy-efficient buildings using energy piles. `http://www.ruukki.com/News-and-events/~/media/Files/News-and-events/Media-kits/Eco%20Build%202011/EN%20Energy%20pileswhite%20paper%20022011.ashx`. Link last checked: May 25th, 2011.

[45] M. Sanchez, A. Gens, and S. Olivella. Effect of thermo-coupled processes on the behaviour of a clay barrier submitted to heating and hydration. *Annals of the Brazilian Academy of Sciences*, 82(1):153–168, 2010.

[46] T. Sandén, R. Goudarzi, M de Combarieu, M. Åkesson, and H. Hökmark. Temperature buffer test - design, instrumentation and measurements. *Physics and chemistry of the earth*, 32:77–92, 2007.

[47] B.A. Schrefler. F.e. in environmental engineering: Coupled thermo-hydro-mechanical processes in porous media including pollutant transport. *Archives in Computational Methods in Engineering*, 2, 3:1–54, 1995.

[48] A. Segal. Finite element methods for incompressible navier-stokes equations. `http://ta.twi.tudelft.nl/users/vuik/burgers/fem_notes.pdf`, 2011. Link last checked: May 25th, 2011.

[49] J.R. Shewchuk. An introduction to the conjugate gradient method without the agonizing pain. Technical report, Carnegie Mellon University.

[50] Skanska. Energy incorporating energy piles. `http://www.skanska.co.uk/Services/Piling--foundations/About-us/Sustainability/Energy-incorporating-Energy-Piles/`. Link last checked: May 25th, 2011.

[51] J.A. Sopko and M.R. Norman. Ground freezing for tunnel support no. 7 line subway extension new york city.

[52] N.K. Toker. Improvements and reliability of MIT tensiometers and study on soil moisture characteristic curves. Master's thesis, M.I.T., 2002.

[53] I. Towhata, P. Kuntiwattanaku, I. Seko, and K. Ohishi. Volume change of clays induced by heating as observed in consolidation tests. *Soils and foundations*, 33(4):170–183, 1993.

[54] M.V. Villar and R. Gomez-Espina. Retention curves of two bentonites at high temperature. *Springer Proceedings in Physics*, 112:267–274, 2007.

[55] C. Vuik. Iterative solution methods. `http://ta.twi.tudelft.nl/users/vuik/burgers/lin_notes.pdf`, 2011. Link last checked: May 25th, 2011.

[56] W. Wang, G. Kosakowski, and O. Kolditz. A parallel finite element scheme for thermo-hydro-mechanical (thm) coupled problems in porous media. *Computers & Geosciences*, 35:1631–1641, 2009.

[57] W. Wu, X. Li, R. Charlier, and F. Collin. A thermo-hydro-mechanical constitutive model and its numerical modelling for unsaturated soils. *Computers and Geotechnics*, 31 (2004):155–167, 2003.

[58] Hai-Sui Yu. *Plasticity and Geotechnics*. Springer, 2006.

Appendix A

One-dimensional nonporous linear elastic equations

In this appendix the one-dimensional balance equations for a nonporous (i.e. $\phi, \kappa^{int} = 0$) linear elastic material will first be derived. These equations can then be used to derive a set of analytical solutions which can be used to verify the THM implementation of PLAXIS.

A.1 One-dimensional balance equations

In this section a set of one-dimensional governing equations is derived which will be used to verify the numerical implementation in PLAXIS. This is done in section 4.1. The equations derived in section 3.1 are used as the basis for these one-dimensional equations. The one dimensional nature of the equations should be interpreted in the way that all derivatives in the second and third spatial dimension are zero. In order to allow for a fair comparison with the PLAXIS 2D implementation certain effects of the 2D configuration should be taken into account. For example: if a soil sample is subjected to a one-dimensional loading in PLAXIS 2D, the deformation in that direction can be influenced by the lateral boundary conditions in a higher-dimensional geometry like PLAXIS 2D. Whether this occurs depends on the value of the the material model used and the lateral displacement boundary conditions. If the material is linear elastic for instance, the Poisson ratio is the parameter of the material model that links the axial deformation to the lateral boundary conditions. In order to get a good fit between the one-dimensional equations and the implementation in PLAXIS 2D these effects will be considered.

Since a nonporous material will be investigated, the 1D-version of the water mass balance equation (3.32) has no significance. The energy balance equation (3.49) reduces to:

$$C_s \rho_s \frac{\partial T}{\partial t} = \lambda \frac{\partial^2 T}{\partial y^2} \tag{A.1}$$

In the derivation of this expression the heat production Q^h has been set to zero.
When linear elasticity is assumed, matrix M in equation (3.57) becomes.

$$\mathbf{M} = \frac{E'}{(1-2\nu')(1+\nu')} \begin{pmatrix} 1-\nu' & \nu' & \nu' & 0 & 0 & 0 \\ \nu' & 1-\nu' & \nu' & 0 & 0 & 0 \\ \nu' & \nu' & 1-\nu' & 0 & 0 & 0 \\ 0 & 0 & 0 & \frac{1}{2}-\nu' & 0 & 0 \\ 0 & 0 & 0 & 0 & \frac{1}{2}-\nu' & 0 \\ 0 & 0 & 0 & 0 & 0 & \frac{1}{2}-\nu' \end{pmatrix} \tag{A.2}$$

The reader is reminded that vector $\mathbf{m}$ is defined as:

$$\mathbf{m} = (1,1,1,0,0,0)^T \tag{A.3}$$

and that the matrix-vector product $\mathbf{B}_{DT}\mathbf{m}$ is defined as:

$$(\mathbf{B}_{DT}\mathbf{m}) = (\beta_{DT,x}, \beta_{DT,y}, \beta_{DT,z}, 0, 0, 0)^T \tag{A.4}$$

In order to do a meaningful comparison, the set of equations should match the simulation procedure in PLAXIS. This means that the effect of boundary fixities which are commonly applied in PLAXIS should be taken into account. When compressing a sample in one direction, the fixed boundaries on the sides will influence the axial deformation when the Poisson's ratio is unequal to zero. This effect should be accounted for when deriving the momentum balance equation for the '1D-scenario', since otherwise the model and the analytical output will not match even when the code is properly implemented. The independent variable 'y' is used for the vertical direction. This is also the direction along which the '1D' equations have been derived so far. The strain in this direction is a dependent variable. The strains in the other two directions are zero (standard fixities and plain strain). The strain differential $d\varepsilon$ in equation (3.57) therefore turns into:

$$d\varepsilon = (0, d\varepsilon_{yy}, 0, 0, 0, 0)^T \tag{A.5}$$

Inserting equations (A.5) and (A.2)-(A.4) into equation (3.57) and removing the water pressure term due to the nonporous nature of the material considered gives:

$$\begin{pmatrix} \frac{\partial}{\partial x} \\ \frac{\partial}{\partial y} \\ \frac{\partial}{\partial z} \end{pmatrix} \cdot \left[\frac{E}{(1-2\nu)(1+\nu)} \begin{pmatrix} 1-\nu & \nu & \nu \\ \nu & 1-\nu & \nu \\ \nu & \nu & 1-\nu \end{pmatrix} \left(\begin{pmatrix} 0 \\ d\varepsilon_{yy} \\ 0 \end{pmatrix} - \begin{pmatrix} \beta_{DT,X} \\ \beta_{DT,Y} \\ \beta_{DT,Z} \end{pmatrix} dT \right) \right] + d \begin{pmatrix} 0 \\ -\rho g \\ 0 \end{pmatrix} = 0 \tag{A.6}$$

In which only the first three components of the vectors are shown, since these are the only ones with significance. Shear stresses and strains will not appear in this one-dimensional scenario. In line with the discussion before, the partial derivatives $\frac{\partial}{\partial x}$, $\frac{\partial}{\partial z}$ are zero. Only the 'y' component in equation (A.6) turns out to be unequal to zero:

$$\frac{\partial}{\partial y} \left(\frac{E}{(1-2\nu)(1+\nu)} \left[(1-\nu) \left(d\varepsilon_{yy} - \beta_{DT,Y} dT \right) - \nu dT \left(\beta_{DT,X} + \beta_{DT,Z} \right) \right] \right) - d(\rho g) = 0 \tag{A.7}$$

Since linear elasticity is assumed, the stress and strain differentials in equation (A.7) can be replaced by their non-differential counterparts. The differential dT can be replaced with $(T - T_0)$. This definition defines the thermal strain to be zero at T_0.

$$\frac{\partial}{\partial y} \left(\frac{E}{(1-2\nu)(1+\nu)} \left[(1-\nu) \left(\varepsilon_{yy} - \beta_{DT,Y} (T - T_0) \right) - \nu (T - T_0) \left(\beta_{DT,X} + \beta_{DT,Z} \right) \right] + p_w \right) - \rho g = 0 \tag{A.8}$$

A.2 One-dimensional analytical solutions

Analytical solutions for equations (A.1) and (A.8) are derived in this section. The energy balance equation (A.1) is:

$$C_s \rho_s \frac{\partial T}{\partial t} = \lambda \frac{\partial^2 T}{\partial y^2} \tag{A.9}$$

The thermal boundary conditions are:

$$\begin{cases} T(y,0) &= T_0 &, y \in (0,1) \\ T(0,t) &= T_0 &, t > 0 \\ Q(1,t) &= Q_0 &, t > 0 \end{cases} \tag{A.10}$$

When the time 't' goes to infinity, a steady state situation will be attained. Therefore the choice has been made to split the temperature field into a transient component and a steady state component. The latter matches the non-homogeneous boundary conditions at $y \in \{0, 1\}$ and $t > 0$ given in (A.10).

$$T(y,t) = U(y,t) + V(y) \tag{A.11}$$

In which $U(y,t)$ represents the transient component and $V(y)$ the steady state component. When these components are superimposed they form the final temperature field. The steady state temperature field

will be a straight line since no heat production is present. The slope of this straight line is determined by the constant heat flux at $y = 1$. The temperature at $y = 0$ determines the other constant.

$$V(y) = T_0 - \frac{Q}{\lambda} y \tag{A.12}$$

A positive heat flux means that energy is leaving the system at $y = 1$. Therefore the second term in equation A.12 has a minus sign in front of it. The following boundary conditions therefore apply to the transient term $U(y, t)$.

$$\begin{cases} U(y,0) &= \frac{Q}{\lambda} y \quad , y \in (0,1) \\ U(0,t) &= 0 \quad , t > 0 \\ -\lambda \frac{\partial U}{\partial y}(1,t) &= 0 \quad , t > 0 \end{cases} \tag{A.13}$$

Note that the boundary conditions at $y \in (0, 1)$ are homogeneous now. The next step in the solution procedure is the splitting of U(y,t) into two components:

$$U(y, t) = A(y)B(t) \tag{A.14}$$

Inserting equation A.11 and A.14 into equation A.9 yields:

$$C_s \rho_s A(y) \frac{\partial B(t)}{\partial t} = \lambda B(t) \frac{\partial^2 A(y)}{\partial y^2} \tag{A.15}$$

Note that the steady state component dropped out. Separation of variables gives:

$$\frac{C_s \rho_s}{\lambda B(t)} \frac{\partial B(t)}{\partial t} = \frac{1}{A(y)} \frac{\partial^2 A(y)}{\partial y^2} = -K \tag{A.16}$$

In which the $B = B(t)$ and $A = A(y)$. Since both sides of the equation depend on only one independent variable, they have to be constant. The constant is defined as $-K$ for convenience. The following ordinary differential equation for $B(t)$ is obtained.

$$\frac{\partial B(t)}{\partial t} + \frac{K\lambda}{C_s \rho_s} B(t) = 0 \tag{A.17}$$

Which has the solution

$$B(t) = c_0 e^{\frac{-K\lambda t}{C_s \rho_s}} \tag{A.18}$$

The following ODE is obtained for $A(y)$:

$$\frac{\partial^2 A(y)}{\partial y^2} + KA(y) = 0 \tag{A.19}$$

This yields a solution of the form:

$$A(y) = c_1 \sin\left(\sqrt{K} y\right) + c_2 \cos\left(\sqrt{K} y\right) \tag{A.20}$$

The boundary conditions given in A.13 imply $A(0) = 0$. Therefore c_2 is zero and the solution reduces to:

$$A(y) = c_1 \sin\left(\sqrt{K} y\right) \tag{A.21}$$

In order to satisfy the heat flux boundary condition at $y = 1$ in A.13 it follows that $\frac{\partial A}{\partial y}(1) = 0$.

$$\frac{\partial A(y)}{\partial y} = c_1 \sqrt{K} \cos\left(\sqrt{(}K) y\right) \tag{A.22}$$

In order to avoid the trivial solution $c_1 = 0$ we have to take:

$$\sqrt{K} = \pi \left(\frac{2i+1}{2}\right) \tag{A.23}$$

In which i represents an arbitrary integer. For each choice of K according to equation (A.23), $U(y, t)$ satisfies equation (A.9). Due to the linearity of this differential equation, a solution of the form:

$$U(y, t) = \sum_{i=0}^{n} A_i(y) B_i(t) \tag{A.24}$$

would also hold. The subscript i refers to the use of a constant K_i according to equation A.23. The first boundary condition in (A.13) can be written as:

$$U(y,0) = \sum_{i=0}^{\infty} h_i A_i(y) B_i(0) = \sum_{i=0}^{\infty} h_i A_i(y) = \sum_{i=0}^{\infty} h_i \sin\left(\left(i+\frac{1}{2}\right)\pi y\right) = \frac{Q}{\lambda} y \tag{A.25}$$

In which h_i is a constant which absorbed the constants c_0 and c_1 from equations A.18 and A.21. $A_m \perp A_n$ on $y \in [0,1]$ for $n \neq m$. Therefore the use of the generalized fourier theorem is justified. This theorem states:

$$h_i = \frac{1}{\|A_i\|^2} \cdot \left\langle \frac{Q}{\lambda} y, A_i \right\rangle \tag{A.26}$$

In which:

$$\|A_i\|^2 = \int_0^1 \sin^2\left(\left(i+\frac{i}{2}\right)\pi y\right) dy = \frac{1}{2} \tag{A.27}$$

The last step can be confirmed by using integration by parts. Also:

$$\left\langle \frac{Q}{\lambda} y, A_i \right\rangle = \int_0^1 \frac{Q}{\lambda} y \cdot \sin\left(\left(i+\frac{1}{2}\right)\pi y\right) dy = \frac{4Q(-1)^i}{\lambda \pi^2 (2i+1)^2} \tag{A.28}$$

In which the last step also follows from integration by parts. Substituting equations A.27 and A.28 into A.26 gives:

$$h_i = \frac{8Q(-1)^i}{\lambda \pi^2 (2i+1)^2} \tag{A.29}$$

Substituting equation A.28 back into equation A.25 gives:

$$U(y,t) = \frac{8Q}{\lambda \pi^2} \sum_{i=0}^{\infty} \frac{(-1)^i}{(2i+1)^2} \sin\left(\left(i+\frac{1}{2}\right)\pi y\right) e^{-\frac{\pi^2 \lambda t (1+i)^2}{C_s \rho_s}} \tag{A.30}$$

Substituting equations A.12 and A.30 back into A.11 finally gives:

$$T(y,t) = \frac{8Q}{\lambda \pi^2} \sum_{i=0}^{\infty} \frac{(-1)^i}{(2i+1)^2} \sin\left(\left(i+\frac{1}{2}\right)\pi y\right) e^{-\frac{\pi^2 \lambda t (1+i)^2}{C_s \rho_s}} - \frac{Q}{\lambda} y + T_0 \tag{A.31}$$

The magnitude of the term in the infinite sum of equation (A.31) decreases with increasing 'i' because the exponent becomes more negative. When plotting the equation the sum is therefore truncated after a finite amount of steps. Sufficient terms have been summed if a further increase in amount of terms no longer visually influences the resulting plot. I will now proceed with deriving the equation expressing the strain as function of the temperature. The side boundaries of the model are fixed (i.e. strains in the second and third direction are 0) which is in accordance with equation (A.8). The bottom boundary ($y = 0$) is also fixed, but the top ($y = 1$) is free to move. For simplicity zero gravity is assumed. The water pressure is zero due to the nonporous nature of the material. Equation (A.8) therefore reduces to:

$$\frac{\partial}{\partial y}\left(\frac{E}{(1-2\nu)(1+\nu)}\left[(1-\nu)\left(\varepsilon_{yy} - \beta_{DT,Y}(T-T_0)\right) - \nu(T-T_0)\left(\beta_{DT,X} + \beta_{DT,Z}\right)\right]\right) = 0 \tag{A.32}$$

The deformation governing equation has been derived from the equation of motion with zero acceleration. The term within brackets in equation (A.32) physically represents:

$$\left(\frac{E}{(1-2\nu)(1+\nu)}\left[(1-\nu)\left(\varepsilon_{yy} - \beta_{DT,Y}(T-T_0)\right) - \nu(T-T_0)\left(\beta_{DT,X} + \beta_{DT,Z}\right)\right]\right) = \sigma_{yy} \tag{A.33}$$

So equation A.32 states that the stress does not depend on the independent variable y. It is a constant in this scenario.

$$\frac{\partial \sigma_{yy}}{\partial y} = 0 \tag{A.34}$$

At $y = 1$ the material is free to expand. No external force is applied at this point. It follows that $\sigma_{yy} = 0$ at the top. Therefore equation A.33 says that $\sigma_{yy} = 0$ for any $y \in [0,1]$. Equation A.33 can now be rewritten as:

$$\varepsilon_{yy} = (T-T_0)\left(\beta_{DT,Y} + \frac{\nu}{1-\nu}\left(\beta_{DT,X} + \beta_{DT,Z}\right)\right) \tag{A.35}$$

Note that the Young's modulus E has no influence on the temperature induced deformation. The equations derived in this section will be compared with numerical results in section 4.1.

Appendix B

On the assumption of constant air pressure

Section 3.1 mentioned that the atmospheric air pressure is used as reference level. The term pressure is used instead of tension in this section because it is intuitively easier to work with, even though the mechanical sign convention still applies. So the reader should be aware that negative values of p correspond to pressure. The relative gas pressure is assumed to be zero everywhere. In this appendix the consequences of this assumption and the effects of soil pore gas in general will be investigated.

The assumption of constant air pressure can only be made when the air-phase is continuous. This is often the case for soils with saturation levels below 80%. When the saturation level is above 90% the air is normally concentrated in bubbles [12]. The air inside these bubbles is not in contact anymore with the atmospheric air, and can therefore have a different pressure. There are two governing equations in which the air pressure appeared. It is therefore important to investigate what the effects are of setting the relative gas pressure to zero in these equations.

The first equation is the relative humidity expressed in equation (3.9). The capillary pressure is a parameter in this equation and it depends directly on the air pressure. The relative humidity can be rewritten as:

$$\theta = \exp\left(\frac{p_g - p_w}{\rho_w R_v T}\right) = \exp\left(\frac{p_g}{\rho_w R_v T}\right) * \exp\left(\frac{-p_w}{\rho_w R_v T}\right) \tag{B.1}$$

So the definition of relative humidity in equation (3.9) is multiplied with a term containing the relative gas pressure. The relative humidity is used in the equations governing the vapor flux. When the saturation is very high, and the air-phase is therefore discontinuous, the validity of the equations governing the vapor flux in PLAXIS is questionable. Literature study is required to find out if there is a water vapor flux when disconnected bubbles are present. And if so, a governing equation should be derived. Only when this has been done it seems appropriate to investigate the numerical effect of the gas pressure inside these bubbles on the relative humidity and vapor flux.

The second equation in which the air pressure appears is equation (3.52). When the relative air pressure would not have been set to zero, the term χdp_w in the PLAXIS implementation of the momentum balance equation (3.57) would have been replaced with $\chi dp_w + (1-\chi)dp_g$. This would leads to the following momentum balance equation.

$$\nabla \cdot \left[\mathbf{M}\left(d\varepsilon - \mathbf{B}_{DT}\mathbf{m}dT\right) + \chi dp_w \mathbf{m} + (1-\chi)dp_g\right] + d\left(\rho \mathbf{g}\right) = 0 \tag{B.2}$$

dp_g is an extra unknown. In order to balance the amount of equations and unknowns, an equation describing the air mass balance would be required.

In order to investigate the effect of air pressure on the momentum balance equation it is useful to make a small sidestep first to investigate how the air pressure increases during undrained loading. Undrained behavior describes the pressure response directly after applying an instantaneous load. Skempton's B pore pressure parameters for undrained K0 loading are defined in the following way for air and water respectively:

$$B_{ak} = \frac{\partial p_g}{\partial \sigma_y} \tag{B.3}$$

$$B_{wk} = \frac{\partial p_w}{\partial \sigma_y} \tag{B.4}$$

These pore pressure parameters are not constant during undrained loading and B_{wk} is always larger than B_{ak} [12]. They both approach one as the soil becomes saturated. The fact that B_{wk} is always larger than B_{ak} means that the suction is reduced when undrained compression takes place. Even though the current THM implementation does not implement undrained calculation modes, it is still useful to study Skempton's B parameters since they can give insight in the initial response of a soil under compression. Consider one dimensional consolidation where a load is applied instantaneously to the top of the soil. The bottom is impermeable for water and gas while the top can drain freely. An analytical solution for the water and gas pressure has been derived for this geometry [2]. The permeability of air is orders of magnitude higher than the permeability of water over the full range of saturations possible [12]. This includes the saturation range in which the air phase is discontinuous. The analytical equations for gas and water pressure during consolidation show that even when the permeability for gas and water are of similar magnitude, the excess gas pressure will dissipate orders of magnitudes faster. This will be even more so when the permeability of gas is higher than that of water. The permeability of air through soil decreases as the optimum water content is approached, since the air phase becomes occluded. When this happens the flow of air takes place as diffusion of air through water.

When the instantaneous load is applied the initial response of the pore gas and pore water will be undrained. Since Skempton's pore pressure parameter for water is always higher than that of gas the initial excess pore water pressure will exceed the initial excess gas pressure. Bishop's stress equation (2.25) says that this excess air pressure will make the effective stress less compressive. Compressive effective stress on a material plane has the tendency to increase the shear strength. The momentum balance equation of PLAXIS (3.57) does not take the reduction of the effective stress due to the excess gas pressure into account like equation (B.2) does. It may therefore overestimate the undrained strength of a soil. But an instantaneous load that was the basis of the analytical equations [2] is not so common in civil engineering projects. Constructions are normally built in phases in which the load on the soil is slowly increased. Since the air pressure dissipates so much faster than water pressure it is likely excess pore gas pressures will never build up. In this case the relative gas pressure terms in equation (B.2) will drop out and the momentum balance equation as it is implemented in PLAXIS will be obtained. So when no very high loading rates (e.g. instantaneous loads) are applied the assumption of neglecting the gas pressure in the momentum balance equation of PLAXIS will be acceptable.

When discontinuities in the loading rate occur such as in pile driving, an undrained response may be approached. The assumption that the relative gas pressure is zero may not be valid anymore. Whether the air behaves undrained or not in this scenario should be investigated more closely. PLAXIS currently has an option for undrained hydro-mechanical analysis. The compressibility of the air-water mixture in the soil becomes important since it determines the change in pore pressures and it therefore also influences the initial deformation. The form of the equations describing the undrained compressibility of an air-water mixture differs slightly from literature [12] [15]. Fredlund defines the compressibility of an air-water mixture as: [12]

$$C_{Aw} = SC_wB_w + (1 - S + hS)C_aB_a \tag{B.5}$$

In which the definitions for B_w and B_a are similar to (B.3) and (B.4). The difference is that σ_y is replaced with σ, which represents an isotropic stress change on the bulk soil. C_{Aw} represents the compressibility of the air-water mixture and C_a and C_w represent the compressibility of air and water respectively. The parameter h is Henry's solubility constant which is approximately 0.02. Rewriting into bulk moduli gives:

$$\begin{aligned} \frac{1}{K_{Aw}} &= \frac{SB_w}{K_w} + \frac{(1 - S + hS)B_a}{K_a} \\ K_{Aw} &= \frac{K_wK_a}{SB_wK_a + (1 - S + hS)B_aK_w} \end{aligned} \tag{B.6}$$

The following expression is used in PLAXIS [33]:

$$K_{Aw} = \frac{K_wK_a}{SK_a + (1 - S)K_w} \tag{B.7}$$

The formulation in PLAXIS (B.7) differs in two ways from the formulation of Fredlund (B.6) [12] [15]. First of all the PLAXIS implementation does not take into account that air can dissolve in water. In formulation (B.5) this has a large influence on the compressibility for saturations close to one. This can be seen in Figure B.1. The effect of taking into account that air can dissolve in water can have a large influence at high saturation when formulation (B.5) is used to describe the compressibility. When no

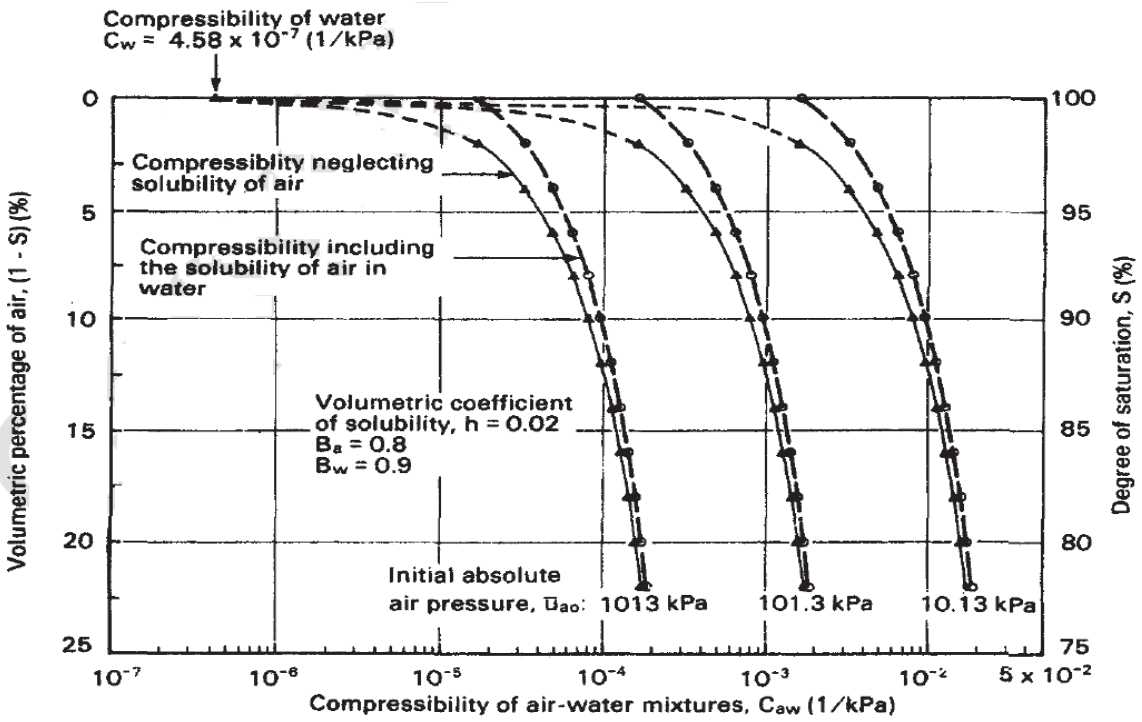

Figure B.1: Equation (B.5) plotted for different initial values of air pressure. The compressibility of air C_a depends on the air pressure. The effect of air dissolution on the compressibility is visualized. This figure comes from [12].

dissolution is considered the compressibility will quickly decrease to that of water. But at high levels of saturation the term hSC_aB_a becomes dominant since C_a is a lot larger than C_w for the air pressure levels shown in Figure (B.1). When the saturation becomes one the solubility term should be dropped and the compressibility will reduce to that of water [12]. Since PLAXIS does not consider dissolution of air into water, large deviations between the formulations (B.6) and (B.7) will occur at high levels of saturation. Another difference between these two formulations is the appearance of pore pressure parameters in (B.6). This is the result of a difference in definition of the bulk modulus. The formulation of Fredlund describes the relative change in volume of an air-water mixture when the bulk soil is loaded. Not all the load is transferred to the pore fluid, so with this definition the compressibility decreases (i.e. bulk modulus increases) when the pore pressure parameters decrease. It is harder to compress the pore fluid since the load is not transferred to it efficiently. The soil skeleton carries most of the load instead. Experiments and the analytical formulations are presented in [12] to describe the relation between the pore pressure parameters and the saturation. Both pore pressure parameters approach one when the soil becomes fully saturated, but whether they actually reach this value depends on the stiffness of the soil. The bulk modulus in the PLAXIS definition describes the volume response when the pore fluid is loaded directly. By setting B_a and B_w to one a scenario is approximated in which the pore fluid is loaded directly. Doing this allows comparison between the bulk moduli of PLAXIS and that of Fredlund.

Fredlund [12] has shown that the isothermal compressibility of air C_a is $1/\overline{p_a}$ under the assumption of an ideal gas. $\overline{p_a}$ represents the abolute air pressure. This means that the isothermal bulk modulus of air equals the abolute gas pressure $\overline{p_a}$. There are contradicting statements about which value is used for the bulk modulus of air in PLAXIS. The internal hydro-mechanical documentation of 2010 mentions that an arbitrarily small value of $1kPa$ is used [33]. The material's manual of PLAXIS 2010 on the other hand mentions that the bulk modulus of air is $100kPa$ [34]. Figure B.3 is used to illustrate the effect of the bulk modulus of air on the bulk modulus of the air-water mixture. The first thing that becomes apparent in this figure is that the bulk modulus of air has an enormous influence on the bulk modulus of the air-water mixture in the entire unsaturated range. This can have a large effect on the undrained bulk modulus K_u, especially if the bulk modulus of the soil is relatively low. A reason for using an arbitrarily low value for the bulk modulus of air could be that the air-phase is assumed to be drained

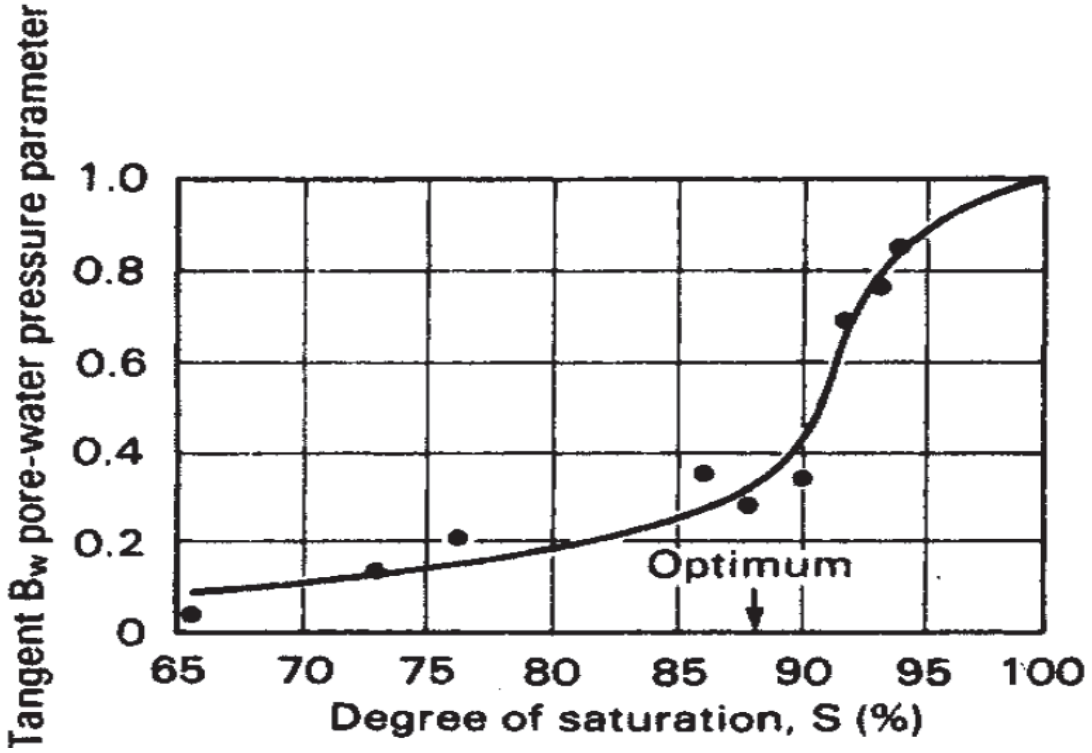

Figure B.2: B_w as function of saturation for a clayey gravel. The experiment was performed by Skempton (1954) and this figure is presented in [12]

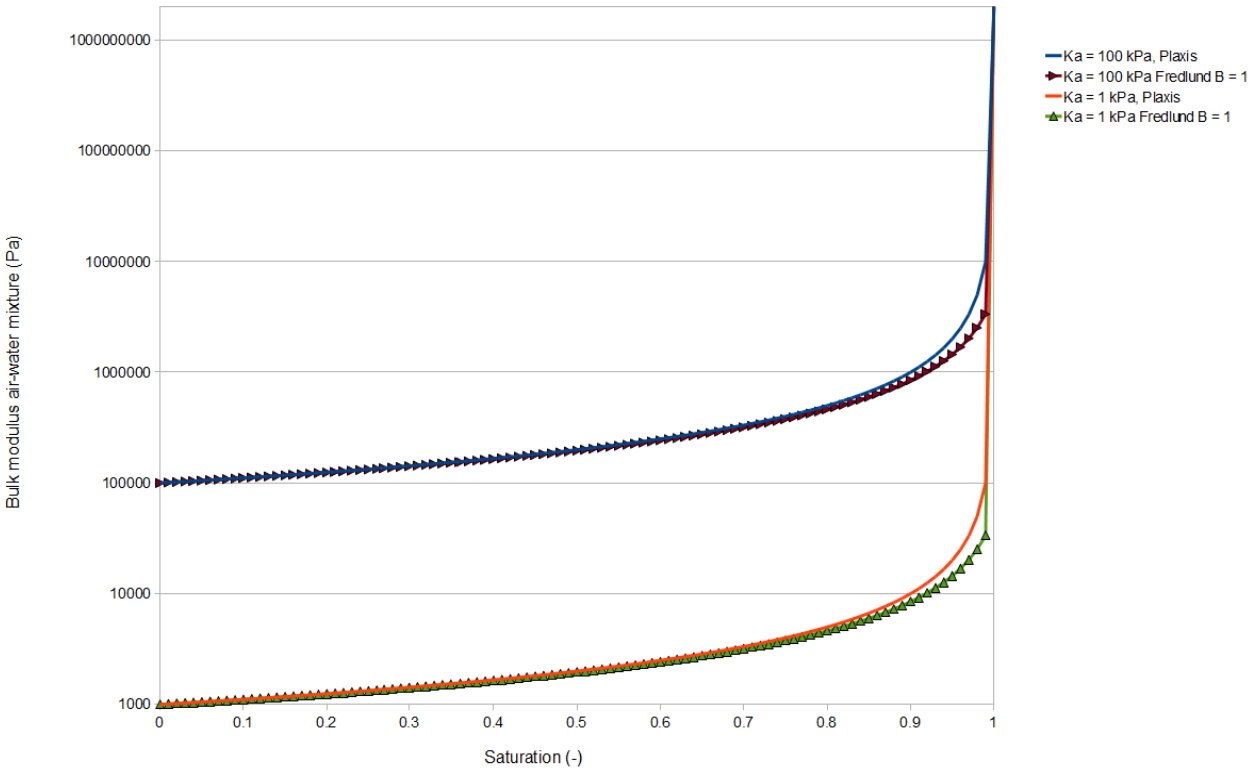

Figure B.3: Bulk modulus is plotted as function of saturation for the formulation of Fredlund (B.6) and PLAXIS (B.7). Different air bulk moduli are used. In Fredlund's equation the effect of loading the pore fluid directly has been simulated by setting Ba and Bw to 1.

while the water phase is assumed to be undrained in an undrained analysis. This would make sense for certain geotechnical projects since excess pore-air pressures dissipate a lot faster as discussed before in this appendix. If this is the case, my recommendation to PLAXIS would be that they write this choice down more clearly in the documentation so the users know which assumptions are made and why. The figure also clearly shows that the dissolution of air into water has a large effect on the bulk modulus for high levels of saturation (note the logarithmic scale in the figure). The PLAXIS implementation does not include this effect. The bulk modulus of the air-water mixture therefore quickly increases to the bulk modulus of water at high level of saturation while this may not be the case in reality. The effect of air solubility reduces as saturation decreases. When undrained compression takes place, the pressure of air and water will increase. Since the bulk modulus of air is equal to the absolute air pressure, it will increase during undrained compression. So in order to correctly model the undrained behavior of an unsaturated soil the change in time of the saturation and air pressure should be modeled since they influence the bulk modulus of the air-water mixture.